

# *Contents*

<b>1</b>	<b>Introduction</b>	<b>1</b>
1.1	Overview of the present PhD work	1
1.2	Wigner crystals	2
1.3	Experimental systems	4
1.3.1	Electrons above liquid He	4
1.3.2	Complex plasmas	5
1.3.3	Colloidal systems	13
1.3.4	Stainless-steel balls on a plane conductor	15
1.3.5	Self-assembled aggregates of magnetized disks	17
1.4	Related systems	19
1.4.1	Quantum dots	19
1.4.2	Magnetic fluids	21
1.4.3	Penning trap for ions	22
1.4.4	Vortices in superconductors and superfluids	23
1.4.5	Biological and related systems	24
1.5	Previous theoretical results on classical clusters	25
1.5.1	Ground state configuration	25
1.5.2	Normal modes	28
1.5.3	Melting	28
1.5.4	Coupled dots: artificial molecules	30

<b>2</b>	<b>Model System and Numerical Approach</b>	<b>33</b>
2.1	General Hamiltonian and the classical limit	33
2.2	Monte Carlo simulation and the Newton optimization	34
2.3	Saddle points	41
2.4	Magnetic field	41
<b>3</b>	<b>Structure of Small and Large 2D Clusters</b>	<b>43</b>
3.1	Introduction	43
3.2	Pure Coulomb potential interaction	44
3.2.1	Small systems	44
3.2.2	Saddle points	47
3.2.3	Large system and topological defect structure	51
3.3	The Yukawa interaction potential	55
3.4	Numerical results for other interaction potentials	58
3.5	Hard wall confinement	60
3.5.1	Small clusters	61
3.5.2	Large clusters	64
3.6	Conclusions	66
3.7	Appendix A - Table I	68
3.8	Appendix B - Table II	73
<b>4</b>	<b>Eigenmode Spectrum</b>	<b>75</b>
4.1	Normal modes in a pure Coulomb system	76
4.2	Normal modes in a Yukawa system	79
4.3	Normal modes in a hard wall confinement	82
4.4	The eigenfrequencies of two particles	87
4.5	Periodic motion of particle at the edge	89
4.6	Conclusions	90
<b>5</b>	<b>Melting of 2D clusters</b>	<b>93</b>
5.1	Introduction	93
5.2	Non-homogeneous melting in a Coulomb system	94
5.3	Melting and energy barriers in a Yukawa system	100
5.4	Conclusions	106
<b>6</b>	<b>2D Clusters in a Magnetic Field</b>	<b>107</b>
6.1	Introduction	107
6.2	Results on complex plasmas	108

<b>7 Nonlinear Screening in Large 2D Coulomb Clusters</b>	<b>113</b>
7.1 Introduction	113
7.2 Numerical approach	114
7.3 Ground state configurations and topological defects	115
7.4 Normal modes	117
7.5 Nonlinear screening	120
7.6 Conclusions	124
<b>8 Summary</b>	<b>125</b>
<b>9 Samenvatting</b>	<b>129</b>
<b>References</b>	<b>133</b>
<b>List of publications</b>	<b>143</b>
<b>Curriculum Vitae</b>	<b>145</b>



# 1

---

## *Introduction*

### 1.1 OVERVIEW OF THE PRESENT PHD WORK

An appreciable amount of theoretical research has already been devoted to classical Wigner crystals. The aim of this thesis is to study in detail how the structural, dynamical and melting properties of a *finite* size classical Wigner crystal which contains boundaries is modified with respect to an infinite two-dimensional (2D) Wigner lattice. The influence of the functional form of the inter-particle interaction, the type of confinement potential and the number of particles is critically examined. Hereby, we aimed at revealing the basic physics of such a system.

Most of the work in this thesis is motivated by experimental results. In the first chapter, I give a few typical examples of experimental systems which have been realized to investigate the classical 2D Wigner crystal.

The second chapter of the thesis is devoted to a description of the model system and the numerical approach which is used to obtain the relevant properties of it. The Monte Carlo simulation technique, the Newton method and the method to calculate the saddle points in the energy landscape are given.

In the third chapter we extend the previous results of Bedanov and Peeters for the ground-state configurations of small pure Coulomb clusters to other interparticle interaction types and to different functional forms for the confinement potential. We also investigate large systems and the topology of the configurations. In a hard wall confined system the physics is very different, e.g. there is a very inhomogeneous distribution of particles because many of them are pushed to the edge of the system where they create a non-parabolic

confinement potential for the other particles; the ground-state configuration is investigated as a function of the inter-particle interaction (Coulomb, dipole, logarithmic and screened Coulomb) and compared with the parabolic case.

The normal modes are treated in the fourth chapter of my thesis. The dispersion relation in a 2D finite system is investigated and compared with the experimental results of the phonon spectrum in a finite size plasma crystal. The normal modes in a 2D system with different interaction potentials show different behaviour. The normal modes of a large but finite size system is compared with the 2D infinite system. Furthermore, we found that in a hard wall confinement potential, the normal modes are very different.

In the fifth chapter, I show our results on melting in both small and large systems. The melting behavior is found to be strongly influenced by the inter-particle interaction potential: a small cluster with a short-range interaction melts earlier than the one with long-range interaction. The melting temperature is related to the energy barriers between the ground state and the metastable states. For larger clusters, the melting scenario changes and is strongly influenced by the location of the topological defects.

The sixth chapter is dedicated to the investigation of clusters in the presence of a magnetic field. The magnetic field dependence of the normal mode spectra of 2D finite clusters of complex plasmas which are confined by an external harmonic potential is presented. The dependence of the normal mode spectrum as a function of a perpendicular magnetic field is discussed. Also the nature of the eigenmodes is investigated.

Finally, we extend the study to a system containing a single fixed point impurity with a variable charge placed in a 2D large Coulomb cluster and make a comparison with the cluster in the absence of the impurity. The screening length as a function of the impurity charge is found to be a highly nonlinear function.

## 1.2 WIGNER CRYSTALS

In 1934, Wigner predicted that electrons crystallize and form a lattice if the density of a three-dimensional(3D) electron gas is lowered beyond a certain critical value [1]. This is due to the fact that the Coulomb energy increases relative to the kinetic energy and correlations begin to strongly dominate the electronic structure. For a homogeneous 3D electron gas, such crystallization is expected at very low densities, i.e., at large values of the average Wigner-Seitz radius.

In the classical regime the importance of the Coulomb interaction is determined by the coupling parameter  $\Gamma = \langle V \rangle / \langle K \rangle$  which is defined as the ratio of the mean potential energy  $\langle V \rangle = e^2 \langle 1/r \rangle = e^2 \sqrt{\pi n_e}$  to the mean kinetic energy  $\langle K \rangle = k_B T$ . This gives  $\Gamma = \sqrt{\pi n_e} e^2 / k_B T$ . In the low temperature quantum regime one has  $\langle K \rangle = E_F = \pi \hbar^2 n_e / m$  and conse-

quently  $\Gamma = r_s = r_0/a_B$ , with  $n_e = 1/\pi r_0^2$  the electron density. According to the value of  $\Gamma$  different regimes can be distinguished. When  $\Gamma < 1$ , which is realized in a dilute system at high temperature, the Coulomb interaction is of minor importance and the system is almost an ideal gas of fermions. For  $1 < \Gamma < 100$  the electrons are correlated and the system behaves liquid-like. For  $\Gamma > 100$ , which is the high-density low-temperature regime, the Coulomb potential energy dominates over the kinetic energy and there are strong correlations between the electrons, which is expected to drive the system through a phase transition to an ordered state, i.e. a periodic crystalline array.

The quest for the observation of such a Wigner crystal has been the object of very intense and continuous work. Experimental observations of a 3D Wigner lattice of electrons has not yet been realized. Electrons in materials like e.g. metals and semiconductors not only feel their mutual repulsion but are also influenced by the ‘imperfect’ host lattice in which they move. Defects, impurities and similar imperfections destroy such a 3D Wigner lattice. Therefore, one has looked for alternative systems in which such Wigner crystallization can be realized. In 1971 Crandall and Williams [2] proposed to look for such Wigner lattice in the 2D system of electrons above a helium surface, where the conditions for crystallization can be realized much more easily and also because of the almost ideal character of the system, i.e. no complicated band structure is present like in real metals, absence of impurities and imperfections, and the inherent low temperature.

After the theoretical prediction of the possibility of the existence of a Wigner lattice on the helium surface [2] the fundamental problem arises: how to observe such a Wigner lattice? The electron solid is lighter, much less dense and is also much less strongly bound than a normal solid, so that different experimental techniques have to be used in order to detect whether or not the 2D electron system is in the ordered phase. Modern processing techniques allowed the artificial creation of such Wigner crystals in the laboratory. Eight years later in 1979, the first discovery of Wigner crystallization of electrons on the surface of liquid helium was reported by Grimes and Adams in Ref. [3].

Experimental investigations of classical Wigner crystals have made considerable progress since the first discovery of Wigner crystallization [3]. Examples of electrons in quantum dots [4], particles in colloidal suspensions [5, 6] and in confined plasma crystals [7–10] can exhibit such classical Wigner crystal-like order structures. Various similar systems, such as laser-cooled ions in a trap [11] which is realized by electric and magnetic fields, trapped ions cooled by laser techniques [12], ions in a radio-frequency (RF) trap (Paul trap) [13, 14] or a Penning trap [15–17] which can also serve as an illustration of 3D Coulomb clusters [18–20].

Other related systems, which exhibit Wigner crystal-like ordering are the following: the vortex clusters in an isotropic superfluid [21], vortices in superfluid  $\text{He}^4$  [22, 23], vortices in a Bose-Einstein condensate stirred with a laser

beam [24], in superconducting grains [25], even in biological system [26, 27] have many common features with those of 2D charged particles [28].

Electron and ion crystals, for example, electron of quantum dots and ions in a penning trap, are atomic scale crystals. Macroscopic crystals have many advantages for the detailed study of the Wigner Crystal, because of the macroscopic size and ease of photographing and controlling over a wide range of parameters. Examples are complex plasmas, and colloidal systems. In the following sections, these experimental systems are discussed in detail.

Very recently, macroscopic 2D Wigner islands, consisting of charged metallic balls above a plane conductor were studied and ground state, metastable states and saddle point configurations were found experimentally by Prof. M. Saint Jean's group at the University of Paris 6 [29]. Dynamic self-assembly of millimetre-size magnetic disks at a liquid-air interface was reported by the G. M. Whitesides' group from Harvard University in Ref. [30, 31]. In the following section, these two experiments will be described in detail.

### 1.3 EXPERIMENTAL SYSTEMS

A substantial amount of experimental research has already been devoted to classical Wigner clusters. Below, I give a few typical examples of experimental systems which have been realized to investigate the static and dynamic properties of Wigner clusters.

#### 1.3.1 Electrons above liquid He

Electrons deposited above the surface of liquid helium will float about  $100\text{\AA}$  above the He surface and have been shown to form the analogue of the microscopic Wigner crystal at sufficient low temperature [3, 32]. The electrons can be trapped in surface states in which they are attracted towards the surface by the small polarization they induce in the liquid, but are prevented from penetrating into the liquid due to a potential energy barrier at the surface. The first discovery of Wigner crystallization of electrons was observed in this system in 1979 [3].

If one applies a strong electric field perpendicular to the helium surface, the system becomes unstable and the homogeneous electron distribution is destroyed. The electrons become localized in a regular array of pockets, or 'dimples', which can be considered as effective classical charged particles.

These many-electron dimples, each of which contains up to  $10^7$  electrons with a typical diameter of the order of 1 mm, can be considered as macroscopic particles and the Coulomb repulsion between them leads to an ordering in a ring configuration as is shown in Fig. 1.1 for 2, 8 and 20 dimples on the surface of liquid Helium [32].

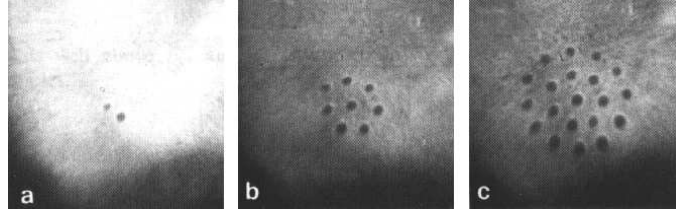


Fig. 1.1 Configurations of (a) 2, (b) 8 and (c) 20 dimples (appearing as dark spots) on a helium surface in an external potential of cylindrical symmetry [from Ref. [32]].

It is not only possible to trap electrons above the surface of liquid helium, but also to trap charged particles, or ‘ions’, below the surface of liquid helium [33]. These ions are created by removing (resulting in a positive ion) or adding (resulting in a negative ion) an electron from or to the helium. As is the case with electron pools trapped above the surface of liquid helium, the trapped ions provide us with simple 2D systems of particles with precisely known (Coulomb) interactions. There are two essential differences with the systems of electrons above the He surface: 1) the effective mass is much larger; and 2) the particle motion is strongly damped because of the friction with the helium liquid.

Such systems are model systems which allow one to carry out experiments analogous to 2D plasma physics and on the behavior of condensed matter in two dimensions. The large effective mass of an ion means that the ion system is always in the classical limit.

### 1.3.2 Complex plasmas

Roughly 99% of all matter in the universe exists in the plasma state, which coexists with dust grains. The formation of Wigner crystals in complex (dusty) plasmas has attracted much interest very recently. The systems containing colloid nano/microscopic particles (“dust”) immersed in a gaseous plasma background have recently been widely discussed in the context of the physics [34–36] and chemistry of plasmas, ionized gases, space physics and astrophysics, and materials research. Earlier this system was also called a *dusty plasma* because the particles were treated as “dust”. Nowadays one refers to it as a *complex plasma* in analogy to the condensed matter field of “complex fluids” in colloids.

This state of matter is ubiquitous in space, e.g. in the interplanetary medium, in interstellar clouds, in comet tails, and in the ring systems of the giant planets as well as in mesospheric noctilucent clouds [37, 38]. In microchip manufacturing, avoiding particle contamination during the many production steps that involve plasmas is a technological challenge [39, 40]. On the other hand, the growth, transport, and deposition of nanoparticles is the

central goal of many plasma deposition techniques, e.g. in the manufacturing of amorphous solar cells [41–44].

This system has four components, i.e. electrons, ions, neutral atoms and dust particles with high charges which are responsible for the unusual plasma properties. Unlike the most ordinary plasmas in space and laboratory which are weakly coupled, i.e. the interaction energy of nearest neighbours is much smaller than their thermal energy (for example,  $\Gamma \sim 10^{-3}$  and  $10^{-5}$  for typical glow discharges and thermonuclear fusion plasmas, respectively), a complex plasma is strongly coupled because every dusty particle carries around  $10^4$  electron charges. The competition between the order caused by the mutual Coulomb interactions and the disorder caused by random thermal motion of particles leads to different states ranging from a solid crystal phase to a liquid phase. The coupling constant  $\Gamma$  is defined as the ratio of the Coulomb interaction potential to the thermal energy. When  $\Gamma$  increases, the system can self-organize from a disordered gas phase to an ordered condensed phase, the so-called classical Wigner crystal.

This system represents a unique bridge connecting plasma physics and condensed-matter physics. This system has been extensively studied in the past few years (see Ref. [45] and references therein). The ordered solid phase of dusty plasmas was first predicted theoretically by Ikezi [46] and observed experimentally as *Plasma crystals* [7–10]. This system opens a new window to many interesting issues of generic behaviour from modern condensed matter and statistical physics. A few typical topics which were studied for a plasma crystal are as the following: (i) The different structures in the crystal phase, especially under an additional dipole field [7–10]. (ii) The normal modes [47, 48] and phonon propagation in the crystal phase under external periodic driving force [49–54]. The excitation of normal modes of 2D Coulomb clusters in laboratory complex plasmas was recently observed [47, 48] and it agrees well with the theoretical prediction [55]. A detailed description of the structure, dynamics and melting of a finite size 2D complex plasma is given in Ref. [56]. (iii) Many experiments [57–63] were devoted to study the structure and the order-disorder phase transition of the plasma crystal, which may serve as a macroscopic model system for melting in two or three dimensions. The dynamical and thermodynamic properties of the particle system can be conveniently studied with video cameras. (iv) The structure of the liquid phase [62, 64]. (v) The defect dynamics [61]. (vi) The microscopic motion and collective excitations in the melting and liquid states [61, 62, 65]. (vii) The anomalous diffusion in the melting and liquid states [65], etc.

In the experiment, particles are trapped in a horizontal layer by a shallow parabolic well, while particles can be electrically suspended in the sheath above the electrodes, where gravity is balanced by the electric force (see the setup in Fig. 1.2). For a plasma with an electron temperature of a few electronvolts, a micrometre-sized dust particle can be charged up to about  $10^4$  electrons due to the much higher electron mobility than ion mobility, which makes this system different from the penning trap system where the ions can

only carry few electrons. The large charges drastically increase  $\Gamma$  and the suspended dust clouds can be turned into ordered crystal states even at room temperature. This is not like in the penning trap, in which the system needs very low temperature e.g. using laser cooling which makes the penning trap setup much more expensive. The larger mass slows down the time scale to the order of a second, and the proper spatial scales make direct observations of particle trajectories feasible, whereas ions in penning traps have much smaller sizes and are much harder to visualize. Therefore, unlike the atomic-scale systems, here particle trajectories can be observed by optical micro-imaging because of the macroscopic size, and the structural and dynamical behaviour can be measured in real time and space. In addition, dynamical processes are only weakly damped which is the main difference between the complex plasma and the colloidal system. By controlling the different parameters, the structure can be changed, leading to a better understanding of phase transitions.

Waves and collective oscillations are fundamental dynamical processes which have attracted many scientists' attention. The normal modes have been obtained from the thermal Brownian motion of the particles around their equilibrium position. The spectral properties of the ground-state configurations were performed by Schweigert and Peeters in Ref. [55]. The excitation of normal modes of 2D Coulomb clusters in laboratory complex plasmas was recently observed [47, 48] and it agrees well with the theoretical prediction [55]. The mode-integrated spectrum shows two broad maxima which are found to be due to "shear-like" and "compression-like" modes [48, 56]. The theoretical results are compared with the experimental data in the following section.

In a plasma crystal, the interaction between charged particles is a Coulomb repulsion, which is screened by the ambient plasma. For only two particles levitated on the same horizontal plane in a sheath, Konopka et al. [66] demonstrated that the binary interaction was accurately modeled by a Yukawa potential,

$$\Phi(r) = \frac{Q}{4\pi\epsilon_0 r} \exp\left(\frac{-r}{\lambda_D}\right), \quad (1.1)$$

where  $r$  is the distance between two particles,  $Q$  is the particle charge, and  $\lambda_D$  is the shielding length. In that experiment, only the potential in the horizontal plane was characterized.

In the following I give a short overview of some typical experiments on plasma crystals, which are relevant for the present work.

### 1.3.2.1 *The infinite 2D Wigner crystal*

One experiment was conducted in an annular radio-frequency (rf) dusty plasma trap by Prof. Lin I's group at National Central University in Taiwan. The micrometer-sized  $SiO_2$  particles were generated through gas-phase reaction and aggregation by introducing  $O_2$  and  $SiH_4$  gases into the low pressure rf Ar discharge and were confined in an annular plasma trap. The degree of

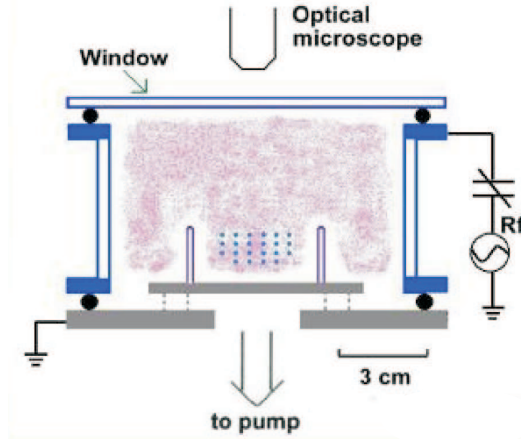


Fig. 1.2 Sketch of the side view of the cylindrical discharge system [from Ref. [7]].

Coulomb coupling decreases monotonically with increasing rf power, which in turn increases the background plasma fluctuations. They were able to form and observe the liquid and crystal phase in the trap by precisely controlling the rf power. Fig. 1.2 shows the side view of a typical experimental system [7]. It consists of a hollow outer electrode capacitively coupled to a 14 MHz rf power amplifier, a grounded center electrode with a ring-shape groove on the top for lateral trapping of the particles, and a top glass window for observation of the particle positions.

When the rf power was decreased to about 1 W at 200 mTorr argon pressure, the formation of different colloidal crystals is observed in the groove region. Fig. 1.3 shows the different crystal structures. A hexagonal crystal was observed which has lowest energy for a 2D infinite system. It is well known that the hexagonal lattice is the most energetically favored structure for infinite 2D system [67].

### 1.3.2.2 Finite Wigner clusters

The experiment is modified further in Ref. [68], instead of the large radius groove, a hollow coaxial cylinder with 3-cm diameter and 1.5-cm height is put on the bottom electrode to confine dust particles in the weakly ionized glow discharge generated in Ar at a few hundred mTorr using a 14-MHz rf power system. By operating at very low rf power ( $< 0.5$  W) creates a nonuniform dark space i.e., the boundary layer, which is adjacent to the cylinder wall and supports outward a radial space charge field. Decreasing rf power can increase the dark space width and, in turn, reduce the diameter of the cluster.

Fig. 1.4 shows a few typical microimages of clusters up to large  $N$  with 1/30 sec exposure time. For small  $N$ , particles are alternately packed in con-

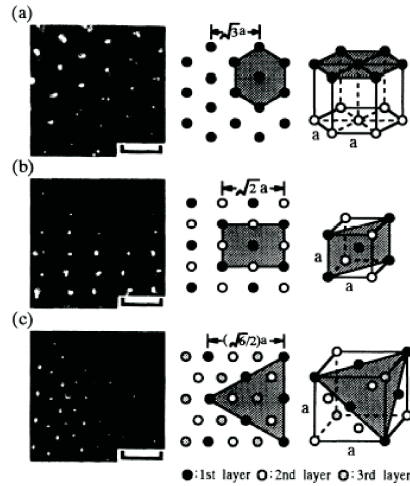


*Fig. 1.3* Micrographs and sketches of the different crystal structures. (a) Hexagonal; (b) bcc; (c) fcc. The center column corresponds to the structures in the micrographs. The graded areas in the sketches are normal to the optical axis [from Ref. [7]].

centric shells with periodically oscillating occupation numbers as  $N$  increases as was predicted by Bedanov and Peeters [70]. The thermal induced collective excitations are dominated by the intershell angular motions. For large  $N$ , the large triangular core surrounded by a few outer circular shells appears and supports vortexlike excitations, which induce uniform and isotropic motions.

With this experimental device, the structure and dynamical behaviour from the highly-ordered state, through the melting and liquid states with associated vortex-type excitation and anomalous diffusion, to the state with self-organized macroscopic dusty waves after losing microscopic order were investigated. Topological defects in the plasma crystal are also investigated by the same group. Very recently, the defect turbulence in 2D creeping dusty plasma Liquids through directly tracking the trajectory of each particle and measuring the evolution of each associated local bond-orientational order was reported [69].

Another experimental setup is the one in which macroscopic finite plasma crystals are studied by Prof. A. Piel's group in Kiel (Germany). In their system, the monodisperse microspheres are immersed in the gaseous discharge plasma of electrons, ions, and neutrals. The particles are trapped in the space charge sheath above the lower electrode where the electric field force levitates the microspheres against the gravitational force. Because of this force balance the particles arrange in a horizontally extended 2D structure. Under an additional horizontal confinement the particles arrange in 2D finite clusters.

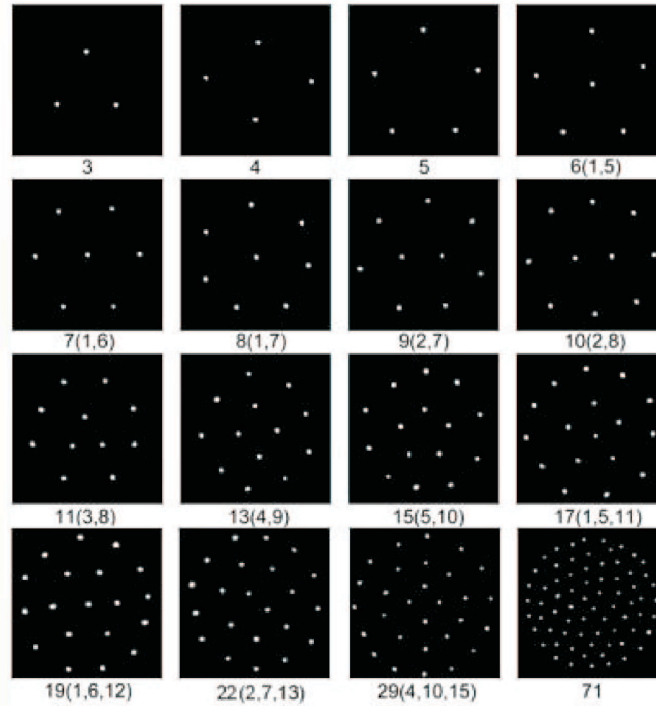


Fig. 1.4 Snapshots of the microimages of the typical cluster structure at different  $N$ . For displaying purposes, the scales are not the same for the pictures. The typical interparticle spacing is between 0.3 and 0.7 mm [from Ref. [68]].

The experiments have been performed in a capacitively coupled parallel plate rf discharge operated in argon at a quite low gas pressure of 1.6 Pa to ensure weak damping. The lower electrode was operated at 13.56 MHz and 9 W forward and 1 W reflected power with a peak-to-peak voltage of  $V_{pp} = 37$  V. The upper electrode and the discharge vessel were grounded (see Fig. 1.5 (a)). Melamine/formaldehyde microspheres of  $9.47\mu\text{m}$  diameter ( $m = 6.73 \times 10^{-13}$  kg) are dropped into the plasma and form a 2D finite Coulomb cluster above the lower electrode. The horizontal confinement for the particles is realized by a shallow circular parabolic trough in the electrode (see Fig. 1.5 (a)). The 2D Coulomb clusters of microspheres are illuminated by a laser sheet and are recorded from the top with a charge-coupled device (CCD) video camera. In the experiment, it was confirmed from the side view camera that the microspheres are indeed trapped into only a single layer.

The validity of the presently accepted values for the particle charge and the shielding length can be tested by analysing the normal modes of more complex objects. Melzer *et al* have recently performed experiments on the normal modes of 2D Coulomb clusters in a parabolic trap. Such clusters arrange in

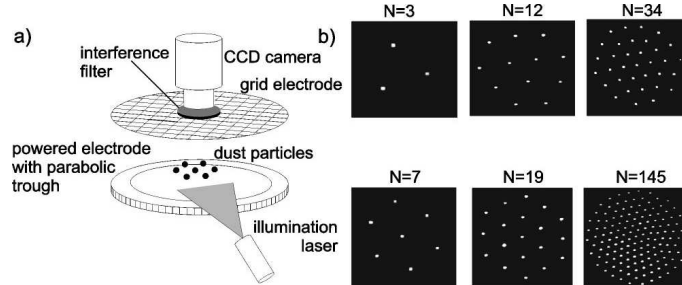
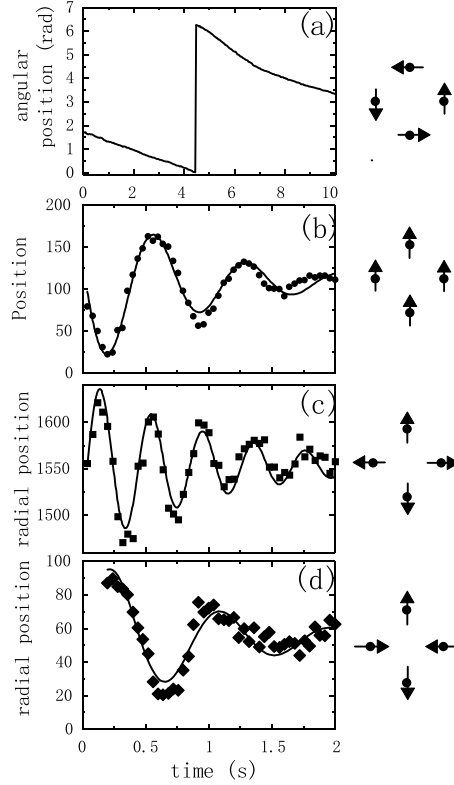


Fig. 1.5 (a) Scheme of the experimental setup. (b) Snapshots of the clusters with  $N = 3, 7, 12, 19, 34,$  and  $145$  particles [from Ref. [48]].

regular shells as first predicted by Bedanov and Peeters [70]. Clusters with up to 100 particles were produced experimentally [68] and their structure compares well with the predictions [70]. Radial oscillations of the particles forming small clusters can be excited by a sudden transition from a state with reduced rf power, which increases the interparticle distance, to normal operation. The particles then perform damped oscillations until they reach their equilibrium positions. The different normal modes of the cluster are then identified from the trajectories of the particles according to the eigenvectors of the modes. As an example, some of the normal modes of a four-particle cluster are shown in Fig. 1.6: First, the center-of-mass motion of the cluster is calculated. Second, the radial and angular positions of all particles in the cluster are determined with respect to the center-of-mass. The breathing mode is then obtained as the oscillation of the sum of the radial positions  $\Sigma r_i/N$ . Finally, the antisymmetric mode is determined from the alternating sum, i.e.,  $(r_1 - r_2 + r_3 - r_4)/4$  when using the  $N = 4$  cluster as an illustrative example. All these modes agree with those predicted by Schweigert and Peeters [55].

The eigenfrequencies of these modes were determined by rearranging the measured trajectories of the four particles into the eigenvectors, which were then fitted by damped harmonic functions. From the analysis of the eigenmodes, the charge and the shielding length can be derived, which compare well with the resonance method and with earlier findings [49, 71]. The normal modes of small two-dimensional clusters were also recently discussed by Amiranashvili *et al* [55, 72].

Very recently, the breathing mode oscillation of a strongly-coupled, dusty plasma disk was experimentally characterized by the Prof. W. L. Theisen's group at Ohio Northern University in USA [73], where the breathing mode oscillation of a circular dusty plasma crystal has been excited by amplitude-modulating the rf power sustaining the discharge. It is the first time a normal mode of a mesoscopic Coulomb cluster has been driven at a single frequency. The resonance curves were found to be in excellent agreement with the theory of a driven, damped harmonic oscillator.



*Fig. 1.6* Normal modes of the  $N = 4$  cluster. (a) rotation around the center of the potential well, (b) center-of-mass motion, (c) breathing mode, (d) antisymmetric mode. The symbols denote experimental values. The curves are best fits to the experimental data [from Ref. [47]].

Mach cones are formed when an object passes through a medium with a velocity that is larger than the sound speed of the surrounding medium. At each instant circular wavefronts are excited by the object that superimpose to form a V-shaped Mach cone, which can be most easily observed in a two-dimensional particle cloud. Mach cones in plasma crystals give the unique opportunity to study phenomena of solid-state physics, which are inaccessible in real solids.

Mach cones have first been observed by Samsonov *et al* [74, 75] by utilizing fast charged particles. Due to the electrostatic repulsion these fast particles induce a disturbance in the above crystal layer thus generating compressional Mach cones. In these experiments it was revealed that at least two distinct nested cones were generated, which were later explained by Dubin [76].

A linear chain is a simple and interesting form of condensed state matter with a low dimensionality. Charged macroscopic-sized particles, levitated

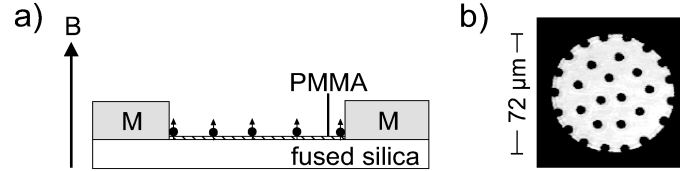


Fig. 1.7 Schematic side view of the experimental cell (a). A TEM mesh (M) serves as lateral confinements for the particles. Photograph (top view) of a single compartment which is occupied by a 2D colloidal system (b) [from Ref. [6]].

in a dusty plasma, can be confined in a single row, forming a 1D plasma crystal [77]. Generic properties of a quasi-one-dimensional classical Wigner crystal were recently studied theoretically [78]. A transverse optical mode was observed in a one-dimensional Yukawa chain with periodic structure [79]. In their experiment, the dispersion relation of phonons was measured, verifying that the optical mode has negative dispersion, with phase and group velocities that are oppositely directed.

### 1.3.3 Colloidal systems

Colloids are small solid particles dispersed in a fluid. Such particles are made from many different materials and can be suspended in a wide variety of solvents. The typical size of colloidal particles ranges from nanometers to micrometers. Because of this small size, thermal energy induces Brownian motion of the particles, and the resultant dynamics can play an important role in the properties of the suspension.

Colloidal particles have a long history and are important in a broad range of applications in technology and materials processing. Here, I give a brief introduction to the subject. The rheological properties of colloidal suspensions have traditionally been of primary concern in their technological applications, and our understanding of these properties continues to evolve. Because they can be produced with a specific size, colloidal particles are now also being used as novel building blocks to engineer completely new materials, including high-precision filters, controlled-porosity substrates, and photonic devices. In addition, new methods are evolving to alter the shape of the particles and create controlled structures with nonspherical particles. New experimental techniques are allowing improved measurement and increased understanding of the structure, properties, and behavior of colloidal suspensions [80].

Colloidal suspensions are also of great scientific interest, motivated not only by their technological applications but also by their potential use as models to investigate the collective phase behavior of systems in which Brownian motion produces an equilibrium state, to explore fundamental questions of packing and geometry, and to fabricate new structures.

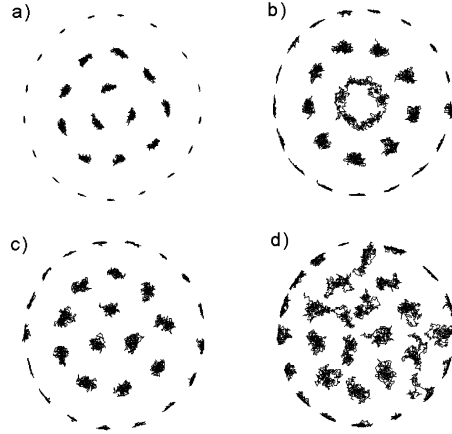


*Fig. 1.8* Particle trajectories ( $N = 29$ ) in a circular confinement for decreasing  $\Gamma$ : (a) 152; (b) 38; (c) 30; (d) 7.5. The data in each picture represent runs of 30 min [from Ref. [6]].

For example, it has been found that the colloidal system displays phenomena as crystallization, melting, structural phase transitions, etc. Thus colloids represent a very interesting classical model system which is conveniently accessible by experiments.

Here I discuss an experiment by the group of Prof. Leiderer at the University of Konstanz [6] which showed interesting phase behavior of a 2D colloidal system confined in a circular hard wall container. As substrate for the 2D colloidal system fused silica plates was used onto which a  $3 - 4\mu\text{m}$  thick smooth film of poly(methyl-methacrylate) (PMMA) was deposited by spin coating. The lateral confinement was realized by a TEM (transmission electron microscope) grid made of copper and a thickness of  $15\mu\text{m}$  which was heated to about  $150^\circ\text{C}$  and then pressed into the thin PMMA film. After this process typically several tens of identical circular compartments (diameter  $72\mu\text{m}$ ) with perpendicular walls was obtained ((see Fig. 1.7 (a)). After insertion of the superparamagnetic colloidal spheres which were suspended in water (DynaBeads  $4.5\mu\text{m}$ ) and stabilized with 0.2 wt % Triton X-100, the particles sedimented towards the shaped bottom plate where they formed a 2D colloidal system in each compartment (see Fig. 1.7(b)). The advantages of colloidal suspensions as model systems are their convenient time (milliseconds) and length scales (microns) which allow detailed observation of single particle trajectories by means of video microscopy.

The superparamagnetic colloidal spheres have a pair potential which can be varied over a wide range by an external magnetic field  $B$ . The external magnetic field induces a magnetic moment  $M$  in the particles leading to a repulsive magnetic dipole pair potential  $V_{i,j} = \mu_0 M^2 / 4\pi r_{i,j}^3$ , where  $r_{i,j}$  is the particle distance. This is a very interesting setup because now one can

change the interaction strength between the particles by changing the external magnetic field  $B$ .

Here I introduce an important coupling parameter  $\Gamma = \langle V_{i,j} \rangle / Nk_B T$ , which is the interparticle interaction energy measured in units of the particle kinetic energy, where the brackets correspond to the sum over all pairs  $i, j, N$  to the number of particles and  $k_B T$  to the thermal energy. The coupling parameter  $\Gamma$  characterizes the order of the system. For a given system, there are only two parameters to characterize the order of the system, namely  $\Gamma$  and number of particles  $N$ . Since  $B$  plays the role of an inverse effective temperature which can be adjusted precisely by the external magnetic field  $B$ . During the experiment, they vary the  $B$  to investigate the melting behaviour, whereas the temperature is kept constant.

At high  $B$ , i.e., strongly repulsive forces between the particles, a shell structure displaying radial and orientational order was observed. With decreasing  $\Gamma$  (by decreasing  $B$  field), they found first a loss of angular order between adjacent shells. Upon further decreasing  $\Gamma$  (reduction of  $B$  field), the angular order is restored again before the system melts completely (see Fig. 1.8).

This interesting behavior was explained theoretically [81] (see also Ref. [82]). The re-entrance melting behaviour was found to be a consequence of the radial particle fluctuations which are responsible for a locking of adjacent shells.

#### 1.3.4 Stainless-steel balls on a plane conductor

“2D macroscopic Wigner islands” were recently studied experimentally by M. Saint Jean’s group at the University of Paris 6 [29]. Their system is macroscopic and very convenient to investigate various behaviors which are observed in mesoscopic confined systems. The system consists of electrostatically interacting charged balls of millimeter size moving on a plane conductor. The advantage of this setup is that one is able to control independently the charge of the balls, their confining potential and the effective temperature.

The temperature is simulated by mechanical shaking. In this system the number of particles is obviously perfectly controlled and the confining potential can be tuned continuously. Moreover, the spatial configuration is directly observed at the macroscopic scale with a video camera.

In the present thesis, I present a detailed comparison between their experimental results and our theoretical results. I also explain why some of the experimental configurations differ from our simulation results [83].

Here I give a detailed description of the experimental setup. The “2D macroscopic Wigner islands” are constituted by stainless-steel balls ( $d = 0.8mm$ ) located on the bottom electrode of a horizontal plane capacitor, the top electrode being a transparent conducting glass. To get the balls charged, a potential  $V_e$  of about one thousand volts is applied to this capacitor. In order to confine the balls, another potential  $V_c$  is applied to an isolated metallic

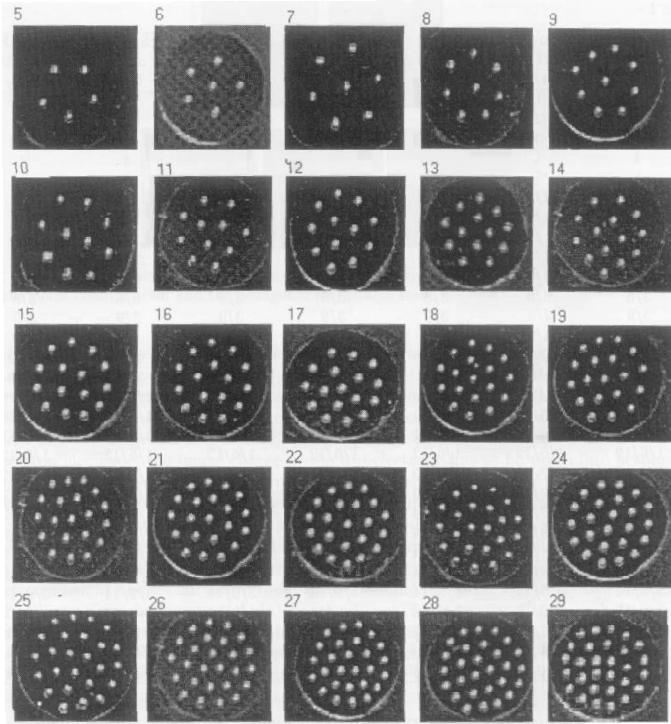


*Fig. 1.9* Examples of ground-state configurations observed for  $N = 5$  to 29. The diameter of the circular frame is 10mm [from Ref. [29]].

circular frame ( $d = 10\text{mm}$ ) intercalated between the two capacitor electrodes. The experiment cell is fixed on a plate that leans on three loudspeakers.

By using loudspeakers, the cell is initially strongly shaken and the system is liquid at this initial stage. A voltage  $V_e$  is then applied and maintained throughout the experiment. Above a 500V threshold, the balls become monodispersely charged, repelling each other and spreading throughout the whole available space. For the used  $V_e$  potential, the charge of each ball is about  $10^9$  electrons. Simultaneously, the potential  $V_c$  is applied to the external frame which repelled the charged balls and confine them in a circular area.

The system is firstly shaken by the loudspeakers to simulate the thermal Brownian motion corresponding to an effective temperature. In order to guarantee that the observed configurations correspond to the ground state with minimum energy, an annealing process is used, i.e., the system is initially heated up and cooled down to very small temperature (i.e. this is given by the noise level produced by the loudspeaker). By analyzing these long time images of the arrays of the balls and measuring the time spent in each

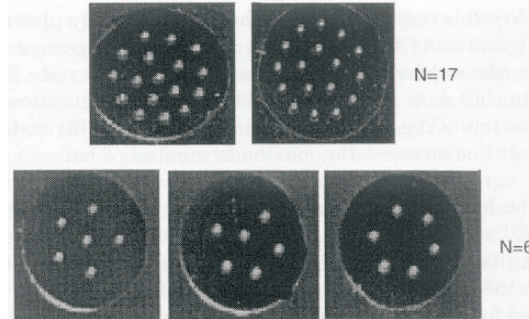


*Fig. 1.10*  $N = 17$ : ground state (1,5,11) and metastable (5,12) configurations.  $N = 6$ : ground-state (1,5) saddle point configuration and the hexagonal metastable state [from Ref. [29]].

observed configuration for a set of fixed experimental parameters, the ground-state configurations are obtained by the most frequently observed state. The ground-state configurations for  $N = 5$  to 29 are shown in Fig. 1.9.

Metastable configurations are observed at the same time as the ground-state configuration. Fig. 1.10 shows, for instance, two configurations observed for  $N = 17$ . Moreover, the unstable equilibrium associated with a saddle point in the configuration space is also observed for  $N = 6$  particles; it corresponds to the transition between the ground state (1,5) and the hexagonal metastable state. Those experimental results are discussed and compared with our theoretical results [83] in the third chapter.

As is well known, the particles configuration depends on the interaction potential and the confinement potential. In this experimental setup, the influence of the interacting potential can be modified by the distance between the balls and the transparent electrode, since the nature of the inter-ball force depends on this distance with respect to the ball dimension. For the large electrode distance, each ball can be considered as a point charge and the inter-ball interaction is then a purely Coulomb interaction which is similar to the earlier theoretically studied system [70].

### 1.3.5 Self-assembled aggregates of magnetized disks

Another interesting experiment is the formation of dynamic patterns of milli-metre-sized magnetic disks which are located at the liquid-air interface and subject to a magnetic field produced by a rotating permanent magnet as investigated by the group of Prof. Whitesides at the department of chemistry and chemical biology at Harvard University in Ref. [30, 31]. By this versatile system, one is able to obtain a better understanding of dynamic self-assembly.

In the experimental system: the circular disks are fabricated by filling hollow polyethylene tubing filled with poly doped with magnetite. The magneti-

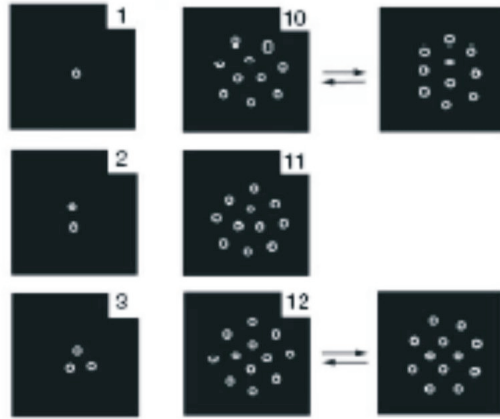


*Fig. 1.11* Dynamic patterns formed by various numbers of disks rotating at the ethylene glycol/water-air interface. For  $n < 5$ , the aggregates do not have a ‘nucleus’ -disks are precessing on the rim of a circle. For  $n > 5$ , nucleated structures appear. For  $n = 10$  and  $n = 12$ , the patterns are bistable in the sense that the two observed patterns interconvert irregularly with time [from Ref. [30]].

cally doped disks are placed on the liquid-air interface, and are fully immersed in the liquid except for their top surface. A permanent bar magnet was placed below the interface and rotated with a certain angular velocity.

The disks spin around their axes with angular frequency equal to that of the magnet. A magnetic force attracts the disks towards the center of the disk, and the repulsive hydrodynamic interaction is due to fluid motion associated with spinning to push them apart from each other.

The competition between the magnetic attraction and the hydrodynamic repulsion of the disks leads to the formation of patterns exhibiting various types of ordering. For small number of disks, pentagons are formed, and for  $N > 6$  multishell structures appear (see the Fig. 1.11). For a large number of disks a hexagonal structure with six-fold symmetry is obtained.

Based on this experimental system setup, the experimental research group not only investigates identical particles (disks), but also systems containing one or two different disks. The experimental results are given in Ref. [84]. The hydrodynamic repulsion generated by the large disk is larger than the hydrodynamic force generated by the small disks, so that the configuration can change drastically. The theoretical investigation of the influence of a single mobile defect particle on the structure of a classical 2D cluster was published in Ref. [85], which was the subject of the Master’s thesis of K. Nelissen [86]. A perfect agreement with the experimental results was realized.

## 1.4 RELATED SYSTEMS

### 1.4.1 Quantum dots

The subject of this thesis is the *classical* Wigner Crystal, which is the classical analog of the well-known quantum dot problem. Quantum dots are atomic-like structures which have interesting optical properties and may be of interest for single electron devices.

Quantum dots are small man-made structures in which electrons are confined in all three spatial directions. As in real atoms, electrons are attracted to a central location. In a natural atom, this central location is a positively charged nucleus, while in quantum dots electrons are typically trapped in a bowl-like parabolic potential. Like natural atoms, these small electronic systems contain a discrete number of electrons and have a discrete spectrum. Therefore, they are called *artificial atoms*. However, these artificial atoms exhibit new physics which have no analogue in real atoms. The origin of this different behavior is the nature of the confinement potential which, being usually parabolic, is much more shallow than the  $1/r$  potential of real atoms. This results in a lower electron density, i.e., a larger mean separation between electrons, than is the case for real atoms. Because the kinetic energy decreases much faster than the Coulomb energy with increasing size of the system, the electron-electron interaction will be much more important than in natural atoms. It turns out that correlations dominate the physics of artificial atoms and the electron configurations can approach the classical Wigner limit in which the electrons are in fixed positions which minimize the electrostatic energy. Because the size and geometry of artificial atoms can be changed arbitrarily, they can be considered as tiny laboratories in which quantum mechanics and the effects of electron-electron interactions can be studied.

Quantum dots (sometimes called artificial atoms) are nanoscale semiconductor structures where a small number of electrons are confined into a small spatial region [87, 88]. As in real atoms, electrons are attracted to a central location. In a natural atom, this central location is a positively charged nucleus, in typical quantum dots, electrons are trapped in a bowl-like parabolic potential.

The electron motion is usually further restricted to two dimensions. There is strong theoretical evidence for the existence of a limit where the electron system crystallizes to Wigner molecules, which is seen as the localization of the electron density around positions that minimize the Coulomb repulsion [89–91].

Classical studies serve as a good starting point for more demanding quantum-mechanical calculations. In the limit of weak confinement (low density) or a very strong magnetic field the quantum effects are quenched and the electron correlations start to dominate the properties of the system. The

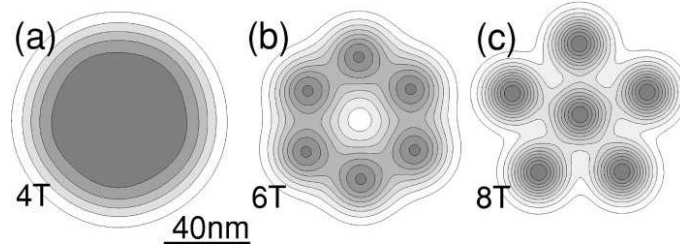


*Fig. 1.12* Electron density distribution for six electrons in (a) approximation of the MDD phase for  $B = 4$  T calculated with the six-center wave function in (1,5) configuration and the Wigner molecules with shell structures (b) (0,6) for  $B = 6$  T and (c) (1,5) for  $B = 8$  T. The darker the shade of grey the larger electron density. The bar shows the length scale [from Ref. [92]].

ultimate limit is a purely classical system where only the Coulomb repulsion between the electrons defines the ground state. The problem reduces to finding the classical positions of electrons which depend on the forms of the confining and the interaction potentials that minimize the total energy of the system.

A quantum dot can be used as a unique physical laboratory for studying properties of electron systems. In particular, the quantum dot confined electron systems are much more sensitive to the external magnetic field than the natural atoms [93, 94]. The application of strong magnetic field induces the formation of Wigner molecules in quantum dots.

The application of the external magnetic field leads to relative shifts of the energy levels corresponding to different spin-orbital configurations. In consequence, the ground-state configuration changes when the magnetic field increases. At a certain, sufficiently high, magnetic field all the electrons have parallel spins and occupy orbitals with successive magnetic quantum numbers. In this state, called a maximum density droplet (MDD), the electron charge distribution still possesses the symmetry of the confinement potential. If, however, the magnetic field increases further, all the occupied energy levels approach the lowest Landau level and become degenerate. Then, the Coulomb interaction leads to a rapid change of the electron distribution. As a result, the confinement-potential symmetry of the electron density is broken and the Wigner molecule is formed.

Fig. 1.12 shows an example of the charge density distribution for six electrons in a parabolic dot for three magnetic field values (from Ref. [92]). If the magnetic field increases above 5.3 T, the electron system becomes the Wigner molecule with the (0,6) shell structure (see the Fig. 1.12 (b)). If the magnetic field exceeds 7 T, the Wigner molecule changes its shape into the (1,5) configuration (see the Fig. 1.12 (c)), which is the lowest-energy configuration of the classical cluster with six particles [70].

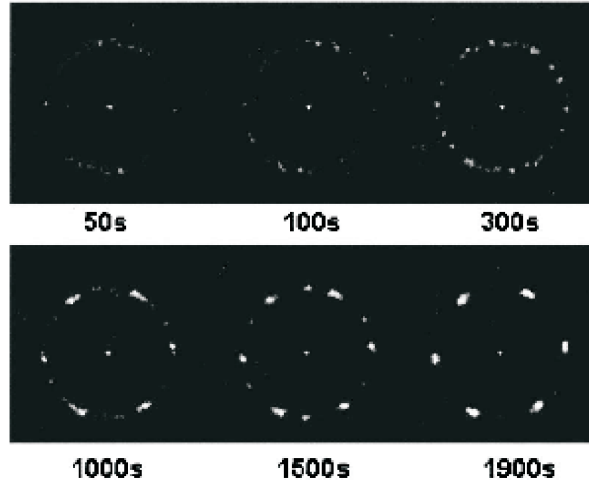


Fig. 1.13 The fast Fourier transform (FFT) of the time series images of the Delaunay triangulation plot [from Ref. [95]].

#### 1.4.2 Magnetic fluids

Versatile structures of a magnetic fluid thin film subjected to an external field have attracted a great deal of attention from researchers due to their induced optical properties and potential applications.

Magnetic fluids typically consist of colloidal magnetic particles, dispersed in a continuous carrier phase. The average diameter of the dispersed particles ranges between 5 – 10 nm. By applying a direct current magnetic field on the magnetic fluid thin film, it is possible to induce a stable structure.

Recently, an oscillating magnetic field perpendicularly to the high-quality magnetic fluid thin film was applied and a phase separation of particles in the liquid matrix was observed [95]. In the absence of an external magnetic field, thermal energy induces a Brownian motion of the particles. Whereas, applying a magnetic field over some critical point, the magnetic nanoparticles phase separate into a droplet form as they overcome the thermal agitation. Through the dipolar interaction among columns, the columnar structure of a high-quality magnetic fluid in a thin film subjected to perpendicular magnetic fields can form 2D lattices. A disordered pattern will appear at lower magnetic fields first, and will arranged to ordered 2D hexagonal lattices at higher fields.

Fig. 1.13 displays the fast Fourier transform of the time series images of the Delaunay triangulation plot. As time elapses, six bright spots appear around the center one. At 1900 s, it becomes six distinct bright spots. This addresses the evolution of the lattice transformation from disorder to the ordered state. In experiment, they also found that the low-frequency oscillating

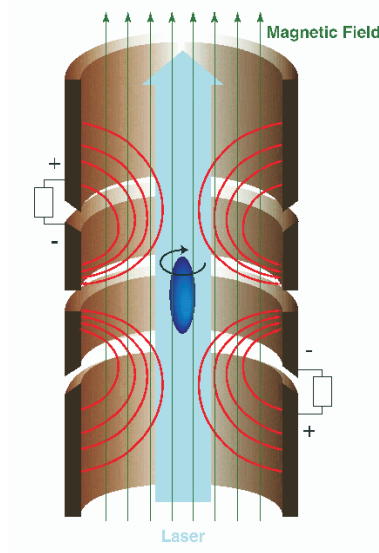


Fig. 1.14 Illustration of a Penning trap, a device that uses electric and magnetic fields to trap charged particles (ions) [from <http://www.aip.org/physnews/preview>].

magnetic field would adjust the columnar lattices to be an ordered structure more efficiently than applying dc magnetic fields.

### 1.4.3 Penning trap for ions

Plasmas are notoriously difficult to control. A plasma made purely of positive particles (such as magnesium ions) or negative particles (such as electrons) is called a “non-neutral plasma”. Such a “non-neutral plasma” can be controlled in a Penning trap, where static electric and magnetic fields are used to confine the charged particles (ions).

These traps typically have cylindrical symmetry [96], normally the batteries are added at the two ends to produce the electric field and the magnetic field travels from bottom to top (see Fig. 1.14). A laser beam is used to cool the ions to very low temperatures, where liquid and crystal-like states are realized. In recent experiments, additional electric fields were added that rotate about the magnetic field lines. These additional field lines allow researchers to confine ions in the traps indefinitely.

The crystallization of small numbers ( $N < 50$ ) of laser-cooled ions into Coulomb clusters was first observed in Paul traps [14, 97]. Here, I discuss the experimental results from Penning traps, where Be ions were confined radially in a cylindrical Penning trap (inner trap diameter 40.6 mm) with a uniform magnetic field  $B = 4.465$  T in the z-axis direction, and near the

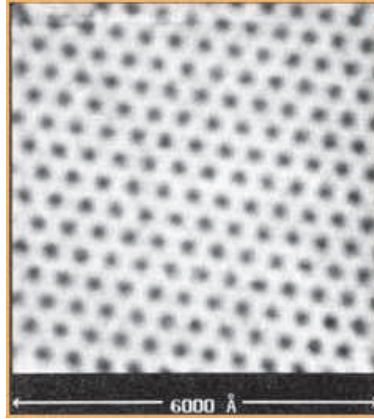


*Fig. 1.15* The Abrikosov flux lattice is imaged in  $NbSe_2$  by tunneling into the superconducting gap edge with a low-temperature scanning-tunneling microscope [from Ref. [98]].

trap center, this axial potential is quadratic. The ions were cooled by a laser beam propagating along the  $z$  axis. The laser power was  $50 \mu\text{W}$  and was focused at the ion plasma to a diameter of  $0.5 \text{ mm}$ . Five different stable crystalline phases were observed, and the energetically favored structure could be sensitively tuned by changing the areal density of the confined ions.

The laser-cooled  $^9\text{Be}^+$  ions confined in two-dimensionally extended lattice planes were directly observed [96]. Different stable crystalline phases for the ions were observed and the energetically favored structure could be sensitively tuned by changing the areal density of the confined ions. The experimental results are in good agreement with theoretical predictions for the planar (infinite in two dimensions) one-component plasma.

#### 1.4.4 Vortices in superconductors and superfluids

A magnetic field can penetrate a type-II superconductors as Abrikosov vortices (see Fig. 1.15), in the absence of pinning centers which form an ideal triangular lattice in a low-temperature region [99].

Vortices in mesoscopic superconductors (which were studied in the PhD thesis of Dr. B. J. Baelus [100]) can be viewed as a specific type of particles interacting magnetically and through the encircling superconducting screening currents with each other. This makes confined vortex structures somewhat similar to other systems such as electrons in artificial atoms that exhibit complex self-organized patterns for a small number of electrons. Such a system may be considered as a two-dimensional analog of a classical Thomson atom [101]. It is interesting to investigate the vortex structure of the mesoscopic superconducting system when only a small number of vortices are present

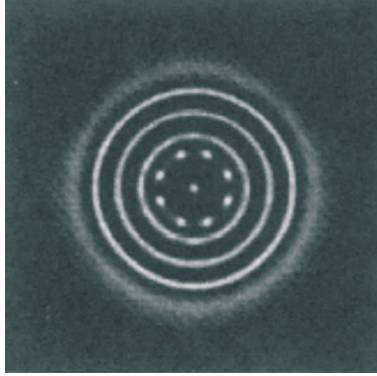


*Fig. 1.16* A snapshot of bacteria density, and the concentric rings are formed [from Ref. [27]].

in the superconducting island or grain [102, 103]. The Abrikosov triangular lattice is modified by the circular boundary conditions.

Similarly to Hund's rule, it is expected that vortices will obey specific rules for shell filling and exhibit magic numbers. It was found that the vortices are arranged in circular shells [104]. The melting of the vortex lattice and formation of a liquid vortex phase with the increase of temperature may take place. This effect was observed for high- $T_c$  superconductors (see review, Ref. [105], and references therein). In Ref. [106], the changes of the structure with temperature and the melting of clusters of vortices in axial-symmetric systems were studied.

#### 1.4.5 Biological and related systems

It is worth noting that this class of patterns is not limited to the physics world; similar ordering structures have been seen in biological system. For instance, motile cells of *Escherichia coli* aggregate form stable patterns of remarkable regularity when grown from a single point on certain substrates. The pattern geometries vary in a systematic way, depending on the initial concentration of the substrate [26].

The formation of spot patterns could be seen in bacterial colonies when the bacteria are subjected to oxidative stress due to hazardous by-products of respiration [27]. The wide variety of patterns is reproduced by the model through varying the details of the initiation of the chemo-attractant emission as well as the transition to a non-motile phase. Fig. 1.16 shows a snapshot of a typical bacteria density. As the interface propagates outwards, it creates a set of concentric rings. The breakup of the rings into spots occurs somewhere behind the front. Concentric rings are formed in the wake of the outer ring.

Ordered arrangements of the spots are easy to achieve once the interaction between different rings is not small.

Similar circular arrangements are found in charge effects on biomolecules, e.g. DNA surrounded by counterions. The structure of negatively charged nucleic acids is strongly influenced by positively charged counterions that surround them. Processes ranging from RNA folding to DNA condensation rely on interactions with ions and charged molecules. Interactions between these structures determine the positions of emerging elements in the developing pattern [107].

Substrate consumption, cell proliferation, excretion of attractant and chemotactic motility, when combined in a certain way, can generate complex spatial structures. With bacteria, these processes can be modulated independently in a controlled manner, allowing accurate tests of quantitative models for pattern formation [26].

## 1.5 PREVIOUS THEORETICAL RESULTS ON CLASSICAL CLUSTERS

There has been considerable theoretical progress in the study of 2D Wigner crystals. Here, I give a short overview of previous results on finite mesoscopic system, which consist of a finite number of charged particles which are confined into an artificial circular symmetric potential.

### 1.5.1 Ground state configuration

More than a hundred years ago, Mayer [108] studied the organization of permanent magnets floating on the surface of a liquid and subject to a central magnetic field. The multi-ring structures observed in Mayer's experiments had many analogies with what was then thought to be the structure of an atom. In fact, it was Mayer's experiments that inspired Thompson to construct in 1904 a classical model that was intended to explain the subatomic structure [101].

Although this picture of classical atoms turned out not to be relevant to describe 'real' atoms, Thomson-type models are adequate for describing many systems composed of finite numbers of interacting particles that behave classically. He was unable to obtain analytical results for a real 3D atom and therefore constrained the particles to move in a plane. This was the first theoretical study of a 2D classical atom, which was recently revisited in the licentiate thesis of Dr. B. Partoens [109].

An important difference with an infinite 2D classical Wigner crystal is, no matter how many particles are confined, that there is a boundary and the particles in the center will behave differently from those at the edge. These boundary effects will play an important role in the following sections.

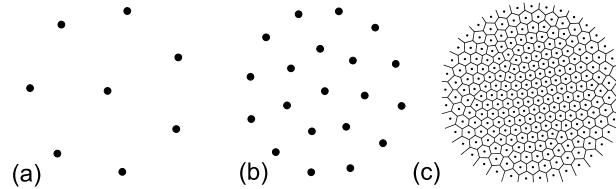


*Fig. 1.17* The classical ground-state configurations for (a) 8, (b) 20 and (c) 230 electrons in parabolic dots. For the 230 electron system the Voronoi construction shows better the hexagonal structure in the centre [From Ref. [70]].

In the case of not too large systems computer simulations by Bedanov and Peeters [70] showed that the particles are localized on rings (see Figs. 7.2 (a) and (b) for 8 and 20 particles, respectively). In Table 1.1 the shell structures are listed for different number of particles  $N$ . This table can be viewed as the classical equivalent to the well-known periodic table of elements. Notice that the particles are arranged into shells with average interparticle distance which is dependent both on the radius (shell number) for a particular structure and on the total number of particles. For large systems (see Fig. 7.2(c) for 230 particles) we found that the structure of the inner shells is very close to the one of a triangular lattice. Namely, almost all those particles are six-coordinated, whereas outer shells consists of lower-coordinated electrons. Thus there is a competition between two types of ordering: ordering into a triangular lattice structure (Wigner lattice) and ordering into a shell structure. The triangular lattice structure is the ordered configuration for a 2D system of point particles while the shell structure is imposed by the circular symmetry of the confinement potential. In fact, the outer particles are a bent triangular lattice with equal number of particles on the last few rings (see the largest  $N$ -values in Table 1.1).

When considering a sequence of systems with increasing  $N$  (see Table 1.1), we can see how shells are being filled by particles and sometimes a new embryo shell appears in the center. This process reminds us of the formation of the periodic system of elements. Also here there are rules for filling the shells. For instance, the first shell (counting from the center) never exceeds five particles, and the second shell never exceeds 10 particles for  $N < 50$  and 11 for larger  $N$ . When all the shells are filled up to their maximum allowed number of particles, a new shell, consisting of only one particle, appears in the center, when adding one particle to the system. Now the second shell has five particles (except for  $N > 50$ ), which is smaller than the maximum allowed.

$N$	$N_1, N_2, \dots$	$\omega_{min}$
3	3	1.41421
4	4	1.25189
5	5	1.02886
6	1,5	0.91889
7	1,6	1.09890
8	1,7	1.10688
9	2,7	0.12681
10	2,8	0.08910
11	3,8	0.02451
12	3,9	0.53084
13	4,9	6.002E-4
14	4,10	0.04940
15	5,10	0.45989
16	1,5,10	0.49237
17	1,6,10	0.05416
18	1,6,11	0.00614
19	1,6,12	0.66759
20	1,7,12	1.031E-4
21	1,7,13	0.00317
22	2,8,12	0.29341
23	2,8,13	0.12867
24	3,8,13	0.02762
25	3,9,13	0.11377
26	3,9,14	0.10409
27	4,9,14	0.01311
28	4,10,14	0.05682
29	4,10,15	0.03911
30	5,10,15	0.29745
31	5,11,15	0.02351
32	1,5,11,15	0.02971
33	1,6,11,15	0.06805
34	1,6,12,15	0.23793
35	1,6,12,16	0.06585
36	1,6,12,17	0.00895
37	1,7,12,17	0.00321
38	1,7,13,17	0.00613
39	2,7,13,17	0.22264
40	4,6,13,17	0.12420
41	4,6,14,17	0.12370
42	3,8,14,17	0.03340
43	3,9,14,17	0.05010
44	3,9,14,18	0.15520
45	3,9,15,18	0.19620
46	3,9,15,19	0.84250
47	4,10,15,18	0.18500
48	4,10,15,19	0.12420
49	4,10,16,19	0.15110
50	4,10,16,20	0.07530
60	1,7,13,18,21	0.07420
70	6,6,15,20,23	0.01220
80	1,6,12,17,22,22	0.01840
100	3,9,15,21,26,26	0.07094
151	1,6,12,18,24,30,30,30	0.19077
230	1,6,12,18,23,25,34,37,37,37	0.21760

*Table 1.1* Ground-state configurations and lowest non-zero eigenfrequency of classical artificial atoms [from Ref. [55, 70]].

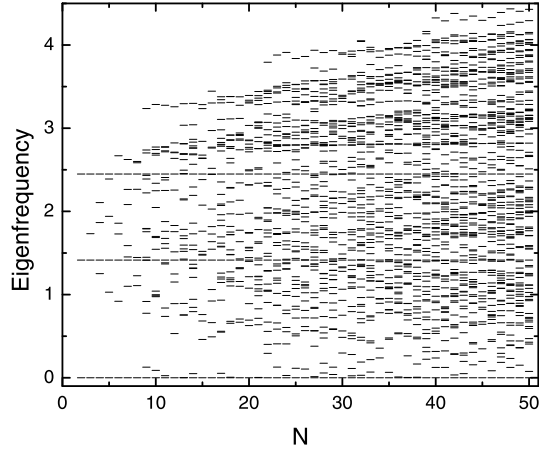


Fig. 1.18 Normal mode frequencies (in units of  $\omega_0/\sqrt{2}$ ) as function of the number of particles:  $N$  [from Ref. [55]].

### 1.5.2 Normal modes

To find the excitation spectrum of the cluster a normal mode analysis was presented in Ref. [55]. By diagonalising the dynamical matrix, one obtains the squared eigenfrequencies of the system. Thus for a cluster of  $N$  particles we have  $2N$  normal modes.

This spectrum is shown in Fig. 1.18 as a function of the number of particles. The eigenfrequencies in this figure are in units of  $\omega_0/\sqrt{2}$ , where  $\omega_0$  is the radial confinement frequency. Notice that there are three horizontal lines which show that there are three eigenfrequencies which are independent of  $N$  [55].

For clusters of sufficient large size (i.e.  $N > 8$ ) we find that a typical feature of its spectrum is the occurrence of a very low eigenfrequency. Because of the scale in Fig. 1.18 this frequency is not always discernable from the  $\omega = 0$  frequency and therefore we have listed it in Table 1.1 as  $\omega_{min}$ . For small  $N$ ,  $\omega_{min}$  corresponds to intershell rotations while for large  $N$  the lowest frequency mode corresponds to a vortex/anti-vortex pair excitation [55]. Configurations with a large value of  $\omega_{min}$  are more stable against deformations and are called ‘magic number’ clusters [55]. Notice that these is a common divisor between the number of particles in each ring of the cluster, i.e. the rings are commensurate.

### 1.5.3 Melting

Understanding the microscopic mechanism of melting has intrigued scientists since the late nineteenth century. Special interest has been devoted to 2D melting [110]. Most works address infinite systems consisting of a single

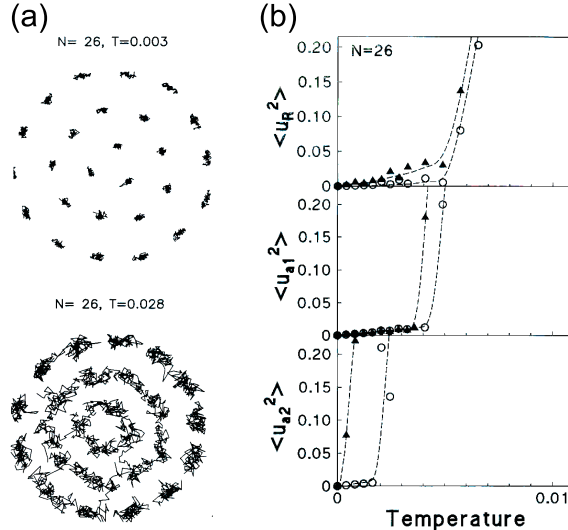


Fig. 1.19 (a) Monte Carlo particle trajectories for a system consisting of  $N = 26$  particles for two different temperatures. (b) Radial displacement  $\langle u_R^2 \rangle$ , the relative intrashell  $\langle u_{a1}^2 \rangle$  and intershell  $\langle u_{a2}^2 \rangle$  angular displacements versus temperature for  $N = 26$ . Results are shown for the first shell (circles) and the outer shell (solid triangles) [from Ref. [70]].

layer. However, whether melting of a 2D crystal is a first order transition and proceeds discontinuously or is a continuous transition in which the crystal first transits into a hexatic phase retaining quasi-long-range orientational order and then melts into an isotropic fluid, is still an open question and a controversial issue [111].

Here we study melting by performing Monte Carlo(MC) simulations. The radial deviations which was introduced in Ref. [70] is applied to characterize the melting behavior:

$$\langle u_R^2 \rangle = \frac{1}{N} \sum_{i=1}^N \left( \langle r_i^2 \rangle - \langle r_i \rangle^2 \right) / a^2, \quad (1.2)$$

with  $a = 2R/\sqrt{N}$  the average distance between the particles, and  $R$  is the radius of the system.

To characterize the relative angular intrashell and the relative angular intershell displacement, we consider the functions defined in Ref. [70], for the relative angular intrashell square deviation

$$\langle u_{a1}^2 \rangle = \frac{1}{N_R} \sum_{i=1}^{N_R} \left[ \langle (\varphi_i - \varphi_{i1})^2 \rangle - \langle \varphi_i - \varphi_{i1} \rangle^2 \right] / \varphi_0^2, \quad (1.3)$$

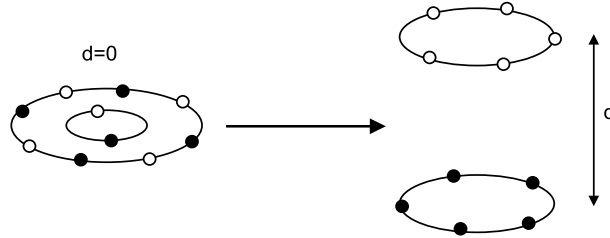


Fig. 1.20 Schematic diagram of the artificial molecule consisting of 10 charged particles in the large  $d$  limit and for  $d = 0$ .

and the relative angular intershell square deviation

$$\langle u_{a2}^2 \rangle = \frac{1}{N_R} \sum_{i=1}^{N_R} \left[ \langle (\varphi_i - \varphi_{i2})^2 \rangle - \langle \varphi_i - \varphi_{i2} \rangle^2 \right] / \varphi_0^2 \quad (1.4)$$

with  $\varphi_i$  the angle of particle  $i$  with respect to the x-axis,  $i1$  indicates the nearest particle to particle  $i$  in the same shell, and  $i2$  refers to the nearest particle to particle  $i$  in the adjacent shell,  $\varphi_0 = 2\pi/N_R$  is the angle between adjacent particles in a shell for a uniform shell with  $N_R$  particles.  $\langle u_{a1}^2 \rangle$  characterizes the angular motion in a particular shell, while  $\langle u_{a2}^2 \rangle$  shows if the motion of the two adjacent shells is correlated or not.

Typical particle trajectories during MC runs for a system of  $N = 26$  in a parabolic confinement potential are shown in Fig. 1.19(a). At low temperatures the particles exhibit harmonic oscillations around their  $T = 0$  equilibrium position, and the oscillation amplitude increases linearly and slowly with temperature: the particles are well localized and display still an ordered structure. At even high temperatures, particles exhibit liquid-like behavior, they can move freely within the shells and can hop from shell to shell.

Temperature dependencies of radial and angular displacements are presented in Fig. 1.19(b). From this picture, one can see that the intershell displacements start to grow at much lower temperatures than the temperature at which the radial displacement jumps. It clearly indicates that the melting scenario of a small laterally confined 2D system shows a two step process. Upon increasing the temperature, first intershell rotation becomes possible where orientational order between adjacent shells is lost while retaining their internal order and the shell structure. At even higher temperatures, the growth of thermal fluctuations leads to radial diffusion between the shells, which finally destroys positional order.

#### 1.5.4 Coupled dots: artificial molecules

It is interesting to extend this work to the case of classical *artificial molecules* [112] which consist of two classical 2D atoms laterally separated by a distance

*d.* Intuitively, we expect interesting behaviour as a function of  $d$  which governs the inter atomic interaction. This can be seen from Fig. 1.20. For  $d = 0$  we have just one 2D atom (e.g. for  $2N = 10$ , this is a two ring structure), while for  $d \rightarrow \infty$  the system consists of two independent 2D atoms with each half of the total number of particles (e.g. two atoms each having 5 particles on one ring). This implies that as a function of  $d$  structural transitions (e.g. configurational changes) have to take place. It was found that these artificial molecules show a surprisingly complex behaviour as a function of  $d$ .



# 2

---

## *Model System and Numerical Approach*

### 2.1 GENERAL HAMILTONIAN AND THE CLASSICAL LIMIT

Before discussing the 2D classical artificial atom, we introduce the full quantum mechanical Hamiltonian which describes  $N$  electrons moving in a 2D quantum dot with a harmonic confinement and interacting through a Coulomb potential. It is given by

$$-\sum_{i=1}^N \frac{\hbar^2}{2m} \nabla_i^2 + \sum_{i=1}^N \frac{1}{2} m \omega_0^2 r_i^2 + \frac{e^2}{\epsilon} \sum_{i=1}^{N-1} \sum_{j=i+1}^N \frac{1}{|\mathbf{r}_i - \mathbf{r}_j|}, \quad (2.1)$$

with  $m$  the effective mass of the electrons,  $\epsilon$  the dielectric constant of the medium the electrons are moving in,  $\mathbf{r} = (x, y)$  is the position and  $\omega_0$  is the strength of the confinement frequency.

We will express this Hamiltonian in dimensionless form. If we use the oscillator length  $a_0 = \sqrt{\hbar/m\omega_0}$  as the unit of length and  $\hbar\omega_0$  as the unit of energy, the dimensionless Hamiltonian becomes

$$H = -\frac{1}{2} \sum_{i=1}^N \nabla_i^2 + \frac{1}{2} \sum_{i=1}^N r_i^2 + \beta^3 \sum_{i=1}^{N-1} \sum_{j=i+1}^N \frac{1}{|\mathbf{r}_i - \mathbf{r}_j|}, \quad (2.2)$$

where the dimensionless electron-coupling constant  $\beta = \sqrt{e^4 m / (\epsilon^2 \hbar^2) / \hbar\omega_0} = a_0/a_B$  with  $a_B = \epsilon \hbar^2 / (m e^2)$  the effective Bohr radius is a measure of the strength of the electron-electron interaction. For a strong confinement, the confinement frequency  $\omega_0$  will be very large, which results in a small coupling

constant  $\beta^3$ . In this limit of small  $\beta$  values, it is a simple *quantum* problem of non-interacting particles in a harmonic oscillator potential, and the electron-electron interaction can be treated as a perturbation. However, in this thesis we are interested in large systems and thus in large values of  $\beta$ . Therefore it is interesting to look at the Hamiltonian after the rescaling of the length  $r \rightarrow \beta r$  which is given by

$$H = -\frac{1}{2\beta^2} \sum_{i=1}^N \nabla_i^2 + \beta^2 \left( \frac{1}{2} \sum_{i=1}^N r_i^2 + \sum_{i=1}^{N-1} \sum_{j=i+1}^N \frac{1}{|\mathbf{r}_i - \mathbf{r}_j|} \right). \quad (2.3)$$

One can see that for large systems the energy increases as  $\beta^2$  and that the importance of the kinetic energy term goes to zero. This leads to the *classical* limit in which the particles can be treated as point particles and the groundstate configurations are found by minimizing the potential energy

$$U = \frac{1}{2} \sum_{i=1}^N r_i^2 + \sum_{i=1}^{N-1} \sum_{j=i+1}^N \frac{1}{|\mathbf{r}_i - \mathbf{r}_j|}. \quad (2.4)$$

It is also interesting to compare the importance of electron-electron interaction in these 2D quantum dots, with those in real atoms and in self-assembled quantum dots. Therefore we have to compare the value of the dimensionless electron-electron coupling constant  $\beta^3 = a_0/a_B$  in all three cases. The most strongly confined, and thus less correlated, 2D quantum dots have a typical confinement strength of  $\hbar\omega_0 = 3$  meV [113], which corresponds to a dot diameter of 100 nm. This yields  $\beta^3 \approx 2$ . Also self-assembled quantum dots can often be approximated by a 2D parabolic confinement potential. A typical confinement strength is  $\hbar\omega_0 = 44$  meV and a diameter of only 20 nm. The corresponding coupling constant equals  $\beta \approx 0.5$ . As  $\beta^3$  equals the typical length scale divided by the effective Bohr radius, this gives for real atoms  $\beta^3 = a_B/a_B = 1$ . Fig. 7.1 shows these three cases, together with an estimate of the number of electrons that can be trapped in the corresponding dot/atom.

Apart from the importance of the electron-electron interaction, there are other differences between real atoms and quantum dots. In the first place of course the confinement potential for the electrons is different. Where in a real atom the electrons are moving around the nucleus due to the Coulomb attraction, the confinement in a quantum dot is typically harmonic. Second, the artificial atoms we consider are two-dimensional, i.e. the electrons can only move in a plane. And most importantly, the number of electrons, the size and the geometry of artificial atoms can be changed experimentally.

## 2.2 MONTE CARLO SIMULATION AND THE NEWTON OPTIMIZATION

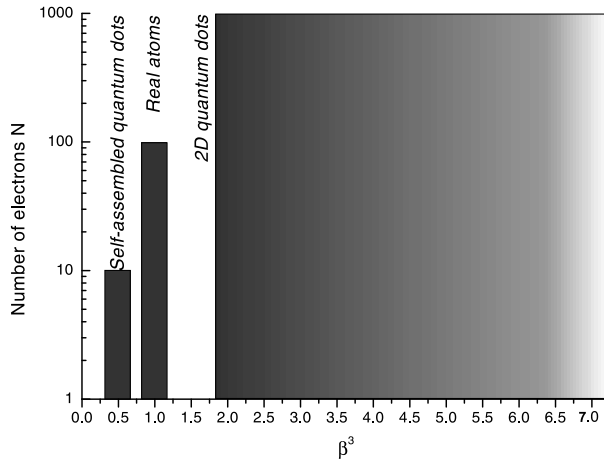


Fig. 2.1 Comparison between the importance of electron correlations in self-assembled quantum dots, real atoms and 2D quantum dots (electrostatically confined) with the number of electrons that can be trapped.  $\beta^3$  is a measure for the strength of the electron-electron interaction [from Ref. [109]].

The structure of the classical artificial atom is found by minimizing the potential energy [70]

$$H = \sum_{i=1}^N \frac{1}{2} m \omega_0^2 r_i^2 + \frac{e^2}{\epsilon} \sum_{i=1}^{N-1} \sum_{j=i+1}^N \frac{1}{|\mathbf{r}_i - \mathbf{r}_j|}. \quad (2.5)$$

For this classical system we will introduce different units for length and energy  $r' = (e^2/\epsilon)^{1/3} \alpha^{-1/3}$ ,  $E' = (e^2/\epsilon)^{2/3} \alpha^{1/3}$  where  $\alpha = m \omega_0^2 / 2$ . Those units are obtained by  $E' = \frac{1}{2} m \omega_0^2 r'^2 = e^2 / \epsilon r'$ . The dimensionless potential energy is given by

$$H = \sum_{i=1}^N r_i^2 + \sum_{i=1}^{N-1} \sum_{j=i+1}^N \frac{1}{|\mathbf{r}_i - \mathbf{r}_j|}. \quad (2.6)$$

This energy only depends on the number of electrons  $N$ , not on the confinement strength  $\omega_0$ , nor on the charge of the particles or the medium they are moving in and therefore we have a rather universal problem.

In the present thesis, we present the results for particles interacting through the Coulomb potential. Moreover, we also consider other interactions such as  $1/r_{ij}^3$ ,  $\exp(-r_{ij}/\lambda_D)/r_{ij} = \exp(-\frac{r_{ij}}{r_0} \frac{r_0}{\lambda_D})/r_{ij} = \exp(-\kappa \frac{r_{ij}}{R})/r_{ij}$  ( $\lambda_D$  is the screening length, and  $\kappa = R/\lambda_D$ ) and  $-\ln r_{ij}$ , for the cases of dipole, screened Coulomb and logarithmic inter-particle interaction, respectively ( $r_{ij} \equiv |\vec{r}_i - \vec{r}_j|$ ).

The particles in a *Complex plasmas* interact through a screened Coulomb potential which depends on the physical parameters and the background

plasma, can have different forms. The average interparticle potential is often assumed to be isotropic and purely repulsive and approximated by the Yukawa (Debye-Hückel) potential [46]. We choose the units:  $r_0 = (2q^2/m\epsilon\omega_0^2)^{1/3}$  for the length,  $E_0 = (m\omega_0^2q^4/2\epsilon^2)^{1/3}$  for the energy and  $T_0 = (m\omega_0^2q^4/2\epsilon^2)^{1/3}k_B^{-1}$  for temperature. The dimensionless Hamiltonian for such a system is given by:

$$H = \sum_i^N r_i^2 + \sum_{i>j}^N \frac{\exp(-\kappa|\mathbf{r}_i - \mathbf{r}_j|)}{|\mathbf{r}_i - \mathbf{r}_j|}, \quad (2.7)$$

where  $\kappa = r_0/\lambda_D$  is the inverse dimensionless screening length. As the range of the Yukawa system can vary from an extremely short-range hard-sphere-like potential for small  $\lambda_D$  to the long-range one-component plasma for  $\lambda_D = \infty$ , it is applicable to a wide variety of systems. When  $\kappa = 0$ , the interaction between particles is a pure Coulomb potential. At zero temperature, the behavior of the Yukawa system is completely characterized by the number of particles  $N$  and  $\kappa$ .

For a dipole system which is perpendicular to the plane of the cluster, they have the pairwise interaction  $d^2/r_{ij}^3$ , where  $d$  is a constant which depends on the experiment. For example, excitons in quantum dots can be considered as a 2D classical system of particles with unidirected dipole momenta  $d \approx 2el/\epsilon$ , where  $l$  is the distance between the two vertically coupled 2D semiconductor dots, and  $\epsilon$  is the dielectric constant which exciton in the media. The Hamiltonian for such a system has the form:

$$H = \sum_i^N r_i^2 + \sum_{i>j}^N \frac{1}{|\mathbf{r}_i - \mathbf{r}_j|^3}, \quad (2.8)$$

The coordinates, energy, and temperature are in the following units:  $r_0 = d^{2/5}/(\frac{1}{2}m\omega_0^2)^{1/5}$  for the length,  $E_0 = \frac{1}{2}m\omega_0^2r_0^2$  for the energy and  $T_0 = k_B T/E_0$  for temperature.

For the logarithmic inter-particle interaction, we can write the potential energy in a dimensionless form if we express the coordinates and energy in the following units:  $r' = \beta^{1/n}\alpha^{-1/n}R^{(n-2)/n}$ ,  $E' = \beta$ , with  $\alpha = \frac{1}{2}m\omega_0^2$ . The dimensionless expression for the potential energy is given by

$$H = \sum_{i=1}^N r_i^n - \sum_{i>j}^N \ln |\vec{r}_i - \vec{r}_j|. \quad (2.9)$$

In order to minimize this potential energy, Monte Carlo simulations were performed. In this procedure one randomly throws the electrons in the confinement potential and one lets the system relax to a minimum energy configuration. The MC simulation technique [114] is relatively simple and rapidly convergent and it provides a reliable estimation of the total energy of the system in cases when relatively small number of Metropolis steps is sufficient.

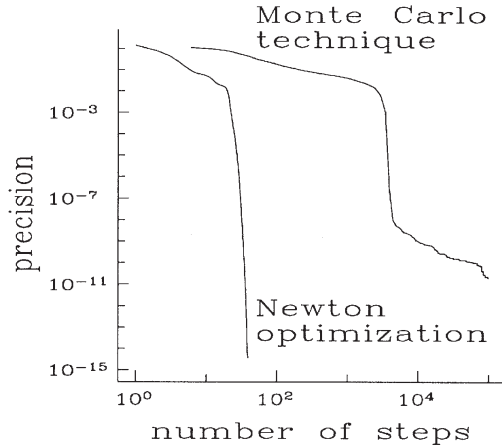


Fig. 2.2 Accuracy of the calculated ground-state energy versus the number of simulation steps, using the MC technique, and the Newton optimization technique for a cluster consisting of  $N = 13$  particles [from Ref. [55]].

However, the accuracy of this method in calculating the explicit states is poor for systems with a large number of particles, which have significantly more metastable states. To circumvent this problem we employed the Newton optimization technique after the standard MC routine. This procedure was outlined and compared with the standard MC technique in Ref. [55]. The efficiency of the Newton method is illustrated in Fig. 7.2. It is apparent that the Newton optimization technique converges much faster.

Let us suppose that the coordinates of the particles are given by  $\{r_{\alpha,i}^n, \alpha = x, y; i = 1, \dots, N\}$ , after  $n$  steps in the simulation. Then the potential energy in the vicinity of this configuration can be written in the following quadratic form

$$\begin{aligned}
 H[r_{\alpha,i}] = & H[r_{\alpha,i}^n] - \sum_i \sum_{\alpha} H_{\alpha,i} (r_{\alpha,i} - r_{\alpha,i}^n) \\
 & + \frac{1}{2} \sum_{i,j} \sum_{\alpha,\beta} H_{\alpha\beta,ij} (r_{\alpha,i} - r_{\alpha,i}^n) (r_{\beta,j} - r_{\beta,j}^n), \quad (2.10)
 \end{aligned}$$

with  $H_{\alpha,i} = -\partial H / \partial r_{\alpha,i}$  the force and

$$H_{\alpha\beta,ij} = \frac{\partial^2 H}{\partial r_{\alpha,i} \partial r_{\beta,j}} \quad (2.11)$$

the dynamical matrix. The next step is based on the condition of minimal energy  $\partial H / \partial r_{\alpha,i} = 0$ , which leads to

$$\sum_j \sum_{\beta} H_{\alpha\beta,ij} (r_{\beta,j} - r_{\beta,j}^n) = H_{\alpha,i}, \quad (2.12)$$

This method will only work in the vicinity of a minimum, in particular when the dynamical matrix is positive definite. That is why this method is applied after the Monte Carlo simulations. In order to assure the stability of the algorithm, instead of solving the set of equations (2.12), we solve

$$\sum_j \sum_\beta (\delta_{\alpha\beta,ij}\eta + H_{\alpha\beta,ij}) (r_{\beta,j} - r_{\beta,j}^n) = H_{\alpha,i}, \quad (2.13)$$

where  $\delta_{\alpha\beta,ij}$  is the unit matrix and  $\eta$  is a damping coefficient. In the first few iterations,  $\eta$  is taken to be large:  $\eta = 10 - 100$ . If in the next step, the total energy of the system decreases, the damping coefficient is reduced, while in the opposite case, the value of  $\eta$  is increased. From our experience we know that such an algorithm for choosing the damping parameter guarantees convergency of the iteration process. The iteration process is stopped after  $\eta$  has become smaller than a critical value and the energy no longer improves beyond a required accuracy.

In this way the system has converged to a stable configuration which corresponds to a local minimum in the energy landscape  $H(\vec{r}_1, \vec{r}_2, \dots, \vec{r}_N)$ . Starting from a different initial random configuration of particles may result in a different local minimum. Repeating the above procedure a sufficient number of times we may expect to obtain the ground state configuration as the one with the lowest energy.

Most of such studies focus on systems with an external parabolic confinement, which is similar to the action of a uniform neutralizing background of charges. Other types of confinements which have also been considered are those residing from a fixed positive charge. Such a positive charge keeps the repelling charged particles together, and is in fact the classical analog for atoms [115, 116]. An extreme case of confinement is the one consisting of hard walls. In a hard wall confined system the physics is very different, e.g. there is a very inhomogeneous distribution of particles because many of them are pushed to the edge of the system where they create a non-parabolic confinement potential for the other particles. To find out the ground-state configuration, the “*Combined Monte Carlo + gradient search*” method are applied.

The 2D cluster consists  $N$  charged particles which interact through a repulsive  $1/r^{n'}$  potential and confined in a hard wall confinement potential. In the following discussion, a general confinement potential  $V(r) = r^n$  is given. So the potential energy of the system is given by

$$E = \sum_{i=1}^N \frac{1}{2} m \omega_0^2 R^2 \left( \frac{r_i}{R} \right)^n + \frac{e^2}{\varepsilon R} \sum_{i>j}^N \frac{R^{n'}}{|\vec{r}_i - \vec{r}_j|^{n'}}, \quad (2.14)$$

where  $R$  the radius of the hard wall,  $e$  the particle charge,  $m$  is the mass of the particles,  $\omega_0$  the radial confinement frequency,  $\varepsilon$  the dielectric constant of the medium the particles are moving in, and  $\vec{r}_i = (x_i, y_i)$  the position of the

$i$ th particle with  $r_i \equiv |\vec{r}_i|$ .  $n \rightarrow \infty$  corresponds to the hard wall limit

$$V(r) = \begin{cases} 0 & \text{for } r < R; \\ \infty & \text{for } r \geq R. \end{cases} \quad (2.15)$$

As the above potential energy depends only on two parameters which depend on the experimental setup (namely  $R$  and  $e^2/\varepsilon$ ) and we have to choose also two units (namely for the length and the energy) it is possible to scale out all experimental dependent parameters. The potential energy can be written in dimensionless form using the following units for length and energy:

$$r_0 = (e^2/(\varepsilon\alpha))^{1/(n+n')} R^{(n'+n-3)/(n+n')} \quad (2.16)$$

$$E_0 = (e^2/\varepsilon)^{n/(n+n')} \alpha^{n'/(n+n')} R^{(2n'-n)/(n+n')} \quad (2.17)$$

with  $\alpha = m\omega_0^2/2$ . In the limit of a hard wall confinement, the length unit becomes  $r_0 \rightarrow R$  which is the radius of the hard wall, and the energy unit becomes  $E_0 \rightarrow (e^2/\varepsilon)/R$ . In the case of parabolic confinement, i.e.  $n = 2$ , and Coulomb interaction, i.e.  $n' = 1$ , we recover the previously defined units [70]:  $r_0 = (e^2/\varepsilon)^{1/3}\alpha^{-1/3}$  and  $E_0 = (e^2/\varepsilon)^{2/3}\alpha^{1/3}$ . The dimensionless expression for the potential energy is given by

$$H = \sum_{i=1}^2 r_i^n + \frac{1}{|\vec{r}_1 - \vec{r}_2|^{n'}}. \quad (2.18)$$

with the hard wall potential limit

$$V(r) = \begin{cases} 0 & \text{for } r < 1; \\ \infty & \text{for } r \geq 1. \end{cases} \quad (2.19)$$

Note that this Hamiltonian only depends on the number of particles  $N$  and not on the radius of the hard wall.

In next chapter, we mainly present results for particles interacting through the pure Coulomb potential (i.e.  $n' = 1$ ). We also consider other interactions such as  $1/r_{ij}^3$ ,  $\exp(-r_{ij}/\lambda_D)/r_{ij} = \exp(-\frac{r_{ij}}{R}\frac{R}{\lambda_D})/r_{ij} = \exp(-\kappa\frac{r_{ij}}{R})/r_{ij}$  ( $\lambda_D$  is the screening length, and  $\kappa = R/\lambda_D$ ) and  $-\ln r_{ij}$ , for the cases of dipole, screened Coulomb and logarithmic inter-particle interaction, respectively ( $r_{ij} \equiv |\vec{r}_i - \vec{r}_j|$ ).

The normal modes of the classical atoms can be studied by diagonalising the dynamical matrix which gives us the squared eigenfrequencies of the system and the corresponding eigenvectors are the corresponding displacements.

In a system of clusters with Coulomb interaction and a parabolic confinement, it is well known that there are three eigenfrequencies which are independent of  $N$  [55]:  $\omega/\omega' = 0, \sqrt{2}$  and  $\sqrt{6}$ , which correspond to the rotation of the system as a whole, the center of mass mode and the breathing mode, respectively. The existence and value of these eigenfrequencies can be obtained analytically [117].

1. For any axial symmetric system the system as a whole can rotate, which leads to an eigenfrequency  $\omega = 0$ .
2. The Hamilton equation of motion yields

$$\dot{v}_{xi} = -2x_i + \sum_{j \neq i} (x_i - x_j) / |\mathbf{r}_i - \mathbf{r}_j|^3. \quad (2.20)$$

Now consider the center of mass  $\mathbf{R} = \sum_i \mathbf{r}_i$  which satisfies the differential equation

$$\frac{d^2 R_x}{dt^2} = \sum_i \dot{v}_{xi} = -2 \sum_i x_i = -2R_x, \quad (2.21)$$

and of course the same for  $R_y$ . Thus we find a twofold-degenerate vibration of the center of mass with eigenfrequency  $\sqrt{2}$ . This frequency is independent of the number of electrons, which is a consequence of the generalized Kohn theorem [118].

3. For the mean square radius  $R^2 = \sum_i (x_i^2 + y_i^2)$  we find

$$\frac{d^2 R^2}{dt^2} = -6 \sum_i (x_i^2 + y_i^2) + 2H + 2T \quad (2.22)$$

with  $T = \sum_i (\dot{x}_i^2 + \dot{y}_i^2)$  the total kinetic energy. So we see that there exists a breathing mode with frequency  $\sqrt{6}$ .

The Lindemann melting criterion [119] states that a solid will melt when the root-mean-square displacement of the particles from their lattice sites reaches a certain critical value  $\delta = \sqrt{\langle u^2 \rangle} / a$ , where  $a$  is the lattice constant, and  $\delta \approx 0.1$  in 3D systems. Thus one starts from the solid phase and melting is induced by the thermal fluctuations. For an infinite 2D system one has  $\langle u^2 \rangle = \infty$  and consequently this criterion is no longer applicable. Therefore, Bedanov *et al* [120] proposed a modified Lindemann parameter

$$\delta' = \frac{1}{a} \sqrt{\langle |\vec{u}(\vec{R} + \vec{a}) - \vec{u}(\vec{R})|^2 \rangle}, \quad (2.23)$$

where fluctuations between nearest neighbours are considered, and it turns out that this quantity is finite for a 2D solid.

To investigate the temperature dependence of the system, we also use the standard Metropolis algorithm [114]. We allow the system to approach its equilibrium state at some temperature  $T$ , after executing  $10^4 - 5 \times 10^5$  "MC steps". Each MC step is formed by a random displacement of all particles. If the new configuration has a smaller energy it is accepted, but if the new energy is larger the configuration is accepted with probability  $\delta < \exp(-\Delta E/T)$ , where  $\delta$  is a random number between 0 and 1 and  $\Delta E$  is the increment in the energy [121].

### 2.3 SADDLE POINTS

Between metastable states and the ground state there are potential barriers. When moving from one metastable state to e.g. the ground state, the system will prefer to transit over the lowest potential barrier, which is the *saddle point configuration* between these energy minima.

One knows that the transition state changes from the saddle point down to the minima on the energy landscape through the steepest decent path in the mass-weighted Cartesian coordinates. To find a saddle point, which presents an extremum of the potential energy, we use a technique from Ref. [122, 123] which is similar to the eigenvector method in Ref. [124]. The most important feature of the algorithm, which makes explicit use of the second derivative matrix of the potential surface, is that it is able to “walk uphill” from the minimum on a potential surface to the transition state (i.e., saddle point).

We start from a minimum of the potential energy corresponding to the ground or a metastable state. In order to find a nearby saddle point, we move to a minimum of the potential energy in all directions except one, which has the lowest eigenvalue, and for which we go to a maximum i.e. saddle point. Starting from different initial states, for which the first small step of the coordinates are chosen randomly, we find all saddle points between the global and local minima on the energy landscape. Repeating this procedure for many different initial state, we find the different saddle point stats between the global and local minima. In this way, we find the path in configurational space from the ground state to the metastable states through the saddle point, from which the geometric properties of the energy landscape are obtained.

### 2.4 MAGNETIC FIELD

It is well known that, the magnetic field does not change the thermodynamic quantities of a classical system of charged particles [125], and consequently also not the structure of the 2D classical system of charges. This is a consequence of the nature of the magnetic force, which only acts on moving particles. On the other hand, the motion of charged particles in a magnetic field is significantly affected due to the presence of the Lorentz force when the cyclotron frequency is larger than the eigenfrequencies of the system, and this is directly reflected on the normal modes of the system.

We followed Ref. [126] to calculate the normal modes of the system in the presence of a perpendicular magnetic field. To obtain the normal modes of a finite system in this case, we assumed an oscillatory solution of each particle around its equilibrium position, namely  $\vec{u}_m(t) = \text{Re}[\vec{R}_m e^{i\omega t}]$  ( $\vec{R}_m$  is a complex vector) for every particle  $m = 1, \dots, N$ . The resulting equations of motion for the  $x, y$  coordinates can be summarized by the Fourier transform the Newton

equations in the following expression

$$(\omega^2 \delta_{\alpha\beta} \delta_{nm} - H_{\alpha\beta, nm} + i\omega\omega_c \varepsilon_{\alpha\beta z} \delta_{nm}) R_{\beta, m} = 0, \quad (2.24)$$

where  $\alpha, \beta = x, y, n, m = 1, 2, \dots, N$ ,  $R_{\beta, m}$  is the particle displacement from its equilibrium position,  $\varepsilon_{\alpha\beta z}$  is the Levi-civita tensor,  $\delta_{\alpha\beta, nm}$  and  $\delta_{nm}$  are the Kronecker deltas,  $\omega_c$  the cyclotron frequency,  $i = \sqrt{-1}$ , and  $\omega$  the frequencies of the normal modes.

Due to the presence of the magnetic field the set of Eq. (2.24) has complex solutions. As a consequence, the eigenvectors have an imaginary component indicating that the response of the system is no longer in phase with an applied oscillating electric field, and each particle performs a rotational motion  $\vec{u}_m(t) = \text{Re}[\vec{R}_m] \cos \omega t - \text{Im}[\vec{R}_m] \sin \omega t$ . Differently from the zero magnetic field case, we have the real and imaginary parts of the eigenvectors field.

As a reference case, it is worth to mention here the solution of the simple problem of a charged particle confined by a parabolic potential moving in a plane, and in the presence of a perpendicular uniform magnetic field. The normal modes of the particle correspond to an oscillatory motion around its equilibrium position in a circular trajectory. It is important to emphasize that the real and imaginary components of the eigenvectors are perpendicular to each other, and of equal magnitude in this case, indicating that they have a difference of phase equal to  $(2n + 1)\pi/2$  ( $n=0,1,2,3,\dots$ ). We will see that in a many-body system this is no longer the case.

# 3

---

## *Structure of Small and Large 2D Clusters*

### 3.1 INTRODUCTION

As mentioned in the introduction, the classical Wigner crystal provides a model system for the study of basic problems in condensed matter physics.

In the present chapter we investigate the ground state configuration for both small and large clusters. The first part of this chapter deals with the study of the system interacting through a pure Coulomb potential and confined in a parabolic trap. A detailed study on the ground state configuration together with the different metastable states will be given. The configuration changes when the system transits from the ground state to different metastable states. The lowest energy barriers connecting those states, i.e. saddle points, are studied. For large clusters we use the defect theory to get a better understanding of the topological nature of the cluster structure and use therefore the Voronoi construction technique [127].

In the second part of this chapter, we study the properties of the clusters interacting through a screened Coulomb potential, i.e. a Yukawa potential, in a complex plasma. The results are compared with the experiment of Ref. [68]. Also results for other different interparticle potential interactions, e.g., dipole potential and logarithmic potential are given.

At the end of this chapter, the structural properties of 2D clusters which are confined in an external hard wall potential are investigated. The ground-state configuration is investigated as a function of the inter-particle interaction (Coulomb, dipole, logarithmic and screened Coulomb). Both small and large clusters are considered.

## 3.2 PURE COULOMB POTENTIAL INTERACTION

In this section, a detailed study on not only the ground-state configuration with both small and large clusters but also on the different metastable states will be given. When the system transits from the ground state to the different metastable states, or between the different metastable states, the configuration changes. Such transitions move through the lowest energy barrier connecting those states, i.e., through a saddle point. The connecting path from the ground state to all metastable states is found and the geometric properties of the energy landscape are discussed. Both small and large clusters are considered.

### 3.2.1 Small systems

Firstly, the structural and static properties of the ground and metastable states for  $N = 1 \sim 40$  will be presented. The configurations are analyzed and compared with available experimental data [29] and the results of previous theoretical approaches [55, 70]. The dependence of the ground-state configuration on the functional form of the confinement potential and the interparticle interaction is calculated for 9 and 16 particles. These dependencies may be responsible for the discrepancies between some of the experimental found configurations and the earlier theoretical results [55, 70, 128].

We list for  $N = 1, 2, \dots, 40$  the energy per particle  $E/N$  in the ground state and in the metastable states, where we also list the energy difference with the ground state  $\Delta E/N$  in the Table I, which is shown in the Appendix A. The configuration is indicated by the number of particles in the different rings, the position of the center of the ring and the radius of the different rings, the width of the ring which is defined as the difference of the maximum radius and minimum radius in the same ring, and the energy of the lowest three normal mode frequencies of the ground state are also given in Table I. This table is rather exhaustive and should be compared with a similar one published in Ref. [128] for a logarithmic interacting system.

For different values of  $N$  there exist different possible values for  $E/N$  which are nothing else than the metastable states. The difference in energy between the metastable and the ground state is given in the third column and the corresponding configuration in the fourth column. Note that with increasing  $N$  the number of metastable configurations increases and in general (but not always) the widths of the rings for metastable configurations are larger and the central ring/particle is not exactly located in the center of the parabolic potential well. For sufficiently large  $N$ , the simple ring structure gradually disappears in the center and the triangular Wigner lattice appears. There is a competition between two types of ordering: ordering into a triangular-lattice structure (Wigner lattice) and ordering into a shell structure, which leads to clusters with interesting self-organized patterns which show concentric shells

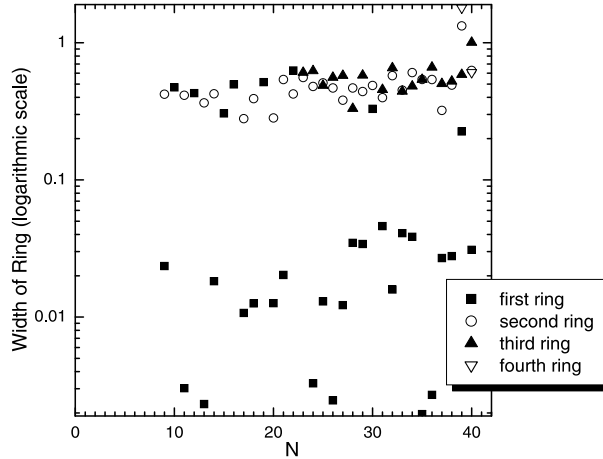


Fig. 3.1 The width of the different shells (logarithmic scale) as function of the number of particles.

at small  $N$  and hexagonal cores surrounded by circular outer shells at large  $N$ .

The rings have sometimes a finite width which are shown in Fig. 3.1 as a function of  $N$ . Notice that the widths fall into three bands; i) width  $\leq 0.003$  which is practically a perfect ring, ii) width  $\sim 0.02$ , and iii) width  $\sim 0.5$ . Usually, but not always, the outer ring has the largest width. The width of the rings increases with increasing  $N$  and at the same time the widest ring becomes often the next to outer ring.

We compare our ground-state configuration with available experimental data [29] and the results of previous theoretical approaches [55, 70, 117, 128–130]. For very small number of particles ( $N < 16$ ), all theoretical and experimental results for the ground state configurations are the same except for  $N = 9$  and 15 whatever kind of interparticle interaction. The experimental observation [29] for the ground state of 9 particles is (1,8) and for 15 particles it is (4,11), which compares to our result (2,7) and (5,10), respectively. For  $16 < N < 30$ , the experimental result and all the calculated patterns present three shells. Our result differs with the experimental data of Ref. [29] for  $N = 16, 17, 20, 22, 24, 25, 27-30$ . Because of the discrepancy between some of the experimental configurations and the ‘numerical exact’ theoretical ground-state configurations it is possible that experimentally the inter-particle interaction is not exactly a Coulombic potential and the confinement potential is not purely quadratic.

Therefore, we investigated the effect of such deviations of these potentials on the ground state configuration. As an example we took  $N=9$  and use confinement potentials  $V \sim r^n$  and for the inter-particle interaction  $V \sim r^{-m}$ . The resulting phase diagram is shown in Fig. 3.2. Notice that, depending on

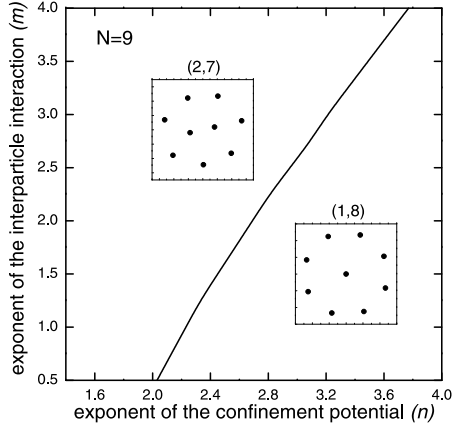


Fig. 3.2 The phase diagram for the ground state of 9 particles. The dependence on the form of the confinement potential and the interparticle interaction is shown.

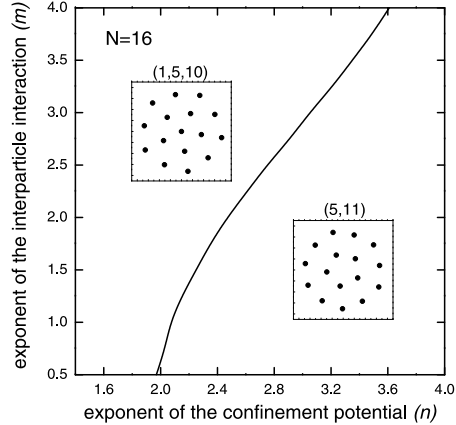


Fig. 3.3 The phase diagram for the ground state of 16 particles. The dependence on the form of the confinement potential and the interparticle interaction is shown.

the values of  $n$  and  $m$ , the system can be either in the (1,8) or the (2,7) configuration. For the harmonic confined Coulomb interacting system i.e.  $(n, m) = (2, 1)$  the system is in the (2,7) configuration but from the phase diagram it is clear that if we change the confinement potential slightly and make it more steep up to  $n \geq 2.2$  the configuration (1,8) becomes the ground state. The experimentally determined ground state configuration for 9 particles was (1,8) [29].

There is also a difference with the experimental data and our results for  $N = 16$  particles. Therefore, we did the same investigation and present the phase diagram in Fig. 3.3. Notice that the harmonic confined Coulomb interacting system, i.e.  $(n, m) = (2, 1)$  is again close to the phase boundary between the configuration (1,5,10) and (5,11). This is probably the explanation why the experimental configuration [29] differs from our simulation results, since it is hard to guarantee that  $(n, m)$  is exactly (2,1) during the experiment.

Notice that for both  $N=9$  and  $N=16$  the metastable configuration has an energy very close to the one of the ground state, the difference is less than 0.2%. These metastable configurations correspond indeed with the experimentally observed ones. Consequently, an alternative explanation for the difference with the experiment is that the experimental configuration got stuck in the metastable configuration.

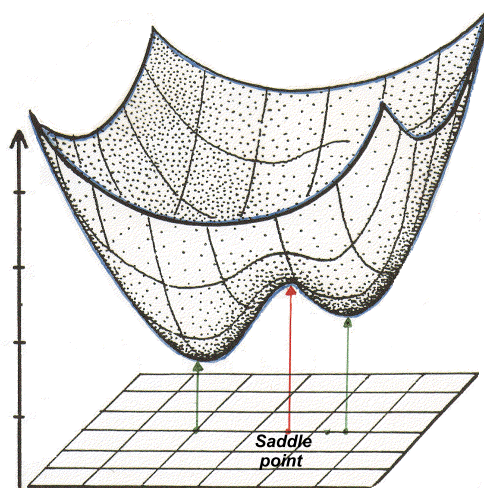


Fig. 3.4 Illustration of a saddle point.

### 3.2.2 Saddle points

Between metastable states and the ground state there are potential barriers. The system will prefer to transfer over the lowest potential barrier, which is the saddle point configuration between these energy minima, in order to transit from one stable configuration to the other. Here we show one illustration in Fig. 3.4. One can see that the saddle point as the local stationary point between the two minima.

We plot in Fig. 3.5 the trajectories of the particles for the  $N=5$  system making a transition from the ground state (5) (see the experimental result in Fig. 3.6) to the metastable state (1,4) and the saddle point connecting them. The trajectories of the particles can also be obtained by moving one of the particles to the center of the system.

For six particles, the ground state (1,5) and the metastable state (6), corresponding to the hexagonal configuration, are obtained. Moreover, the unstable equilibria associated to saddle point configurations are also obtained, and the energy landscape is shown schematically in Fig. 3.7. Similar results for the  $N=6$  energy landscape were found earlier [131]. There are two saddle points for this case, one of them is very close to the metastable state in both energy and configuration, and will therefore be hard to see experimentally [29]. In Fig. 3.7, the insets show the arrangement of the particles for the different states. Using the ‘walking downhill method’, we found the central particle slowly moving to the periphery of the cluster. We would like to stress that the configuration with 6 particles on a perfect ring is a saddle point state in

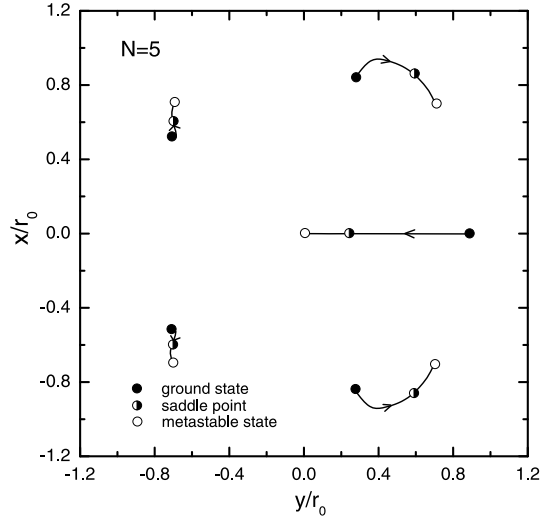


Fig. 3.5 The trajectories of the particles making a transition from the ground state to the metastable state and the saddle point connecting them for 5 particles.

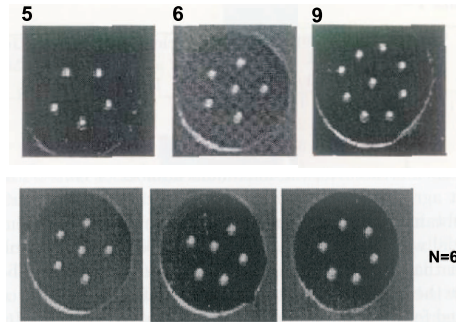


Fig. 3.6 The experimental ground-state configurations for  $N = 5, 6,$  and  $9$  particles. For  $N = 6$  particles: ground-state (1,5) saddle point configuration and the hexagonal metastable state are shown [from Ref. [29]].

contrast to the claim made in Ref. [132]. This can be understood from the following simple model calculation: if 3 particles are placed on a circle with radius  $A$ , on the corners of an equilateral triangle, and the other 3 particles on another equilateral triangle's corners with radius  $B$  rotated over  $60^\circ$ , the energy is

$$E(c) = \frac{9}{2} \left( \frac{1+c^2}{36} \right)^{1/3} \left( \frac{1}{1+c} + \frac{1+c}{\sqrt{3}c} + \frac{2}{\sqrt{1-c+c^2}} \right)^{2/3} \quad (3.1)$$

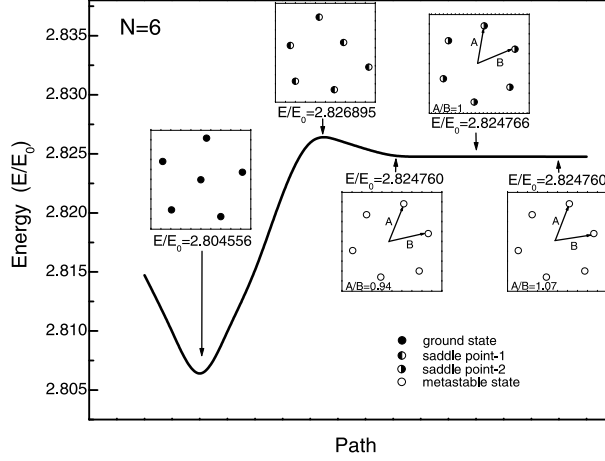


Fig. 3.7 The energy landscape and transition between the ground state to the metastable states for 6 particles.

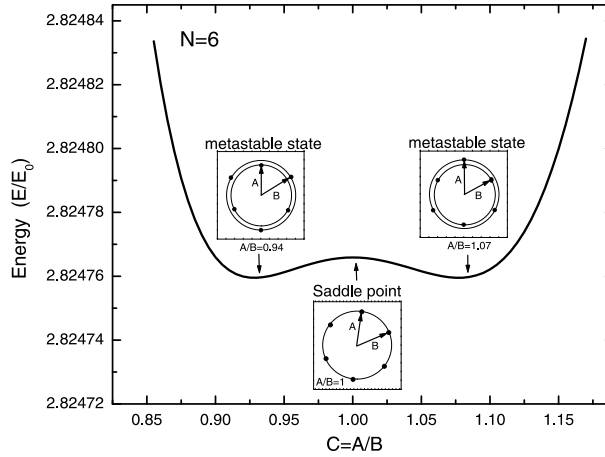


Fig. 3.8 Part of the energy landscape and corresponding configurations near the metastable state for 6 particles.

where  $c = \frac{A}{B}$ . This function is shown in Fig. 3.8. It is clear that the perfect circle configuration i.e.  $c = \frac{A}{B} = 1$  is a saddle point, and that the minimum is obtained if 3 particles move a bit to the center, and the other 3 particles move away from the center (see the insets in Fig. 3.8). Both shown metastable states are connected by a rotation over  $120^\circ$ . The two minima in Fig. 3.8 correspond to the same configuration in which inner and outer ring are interchanged. Comparing our results with Fig. 3.6 of Ref. [29], we see that the other saddle point is observed experimentally.

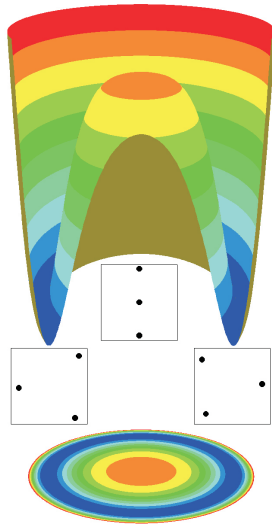


Fig. 3.9 Schematic view of the energy surface and projection of the energy and the corresponding configurations for 3 particles.

A list of the saddle point energies up to 20 particles is given in Table II (see the Appendix B). From this table, we notice that there is only one saddle point state for  $N = 3, 4, 5$  particles. But, on the other hand it is well-known that there are  $(k - 1)$  saddle points when there are  $k$  minima. For  $N=3$  and 4 one saddle point is found, although there is no metastable configuration. The reason is that the saddle point state connects two equilateral ground-state configurations which can be obtained from each other by a simple rotation. For the simple case of 3 particles, we show the energy surface and the corresponding configurations schematically in Fig. 3.9. Notice that there are always more saddle points than minima for  $N > 6$ . With increasing the number of particles, more saddle point states are obtained and the energy landscape gets more complicated. For example for 9 particles, we obtain three saddle points and one metastable state. The results for the trajectories and energy landscape are shown in Fig. 3.10. Again, the ground-state configurations corresponding with the black and the white dot are connected by a simple rotation, i. e. a symmetry operation.

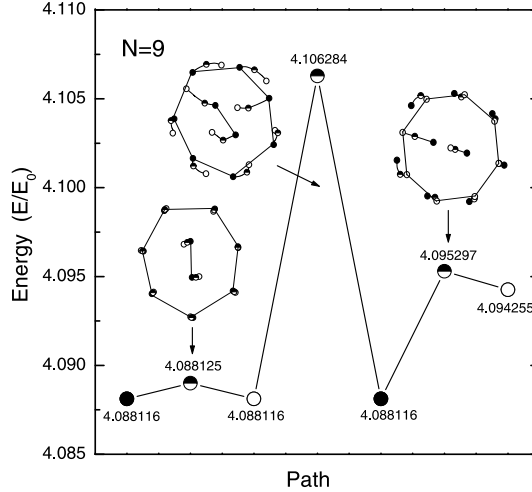
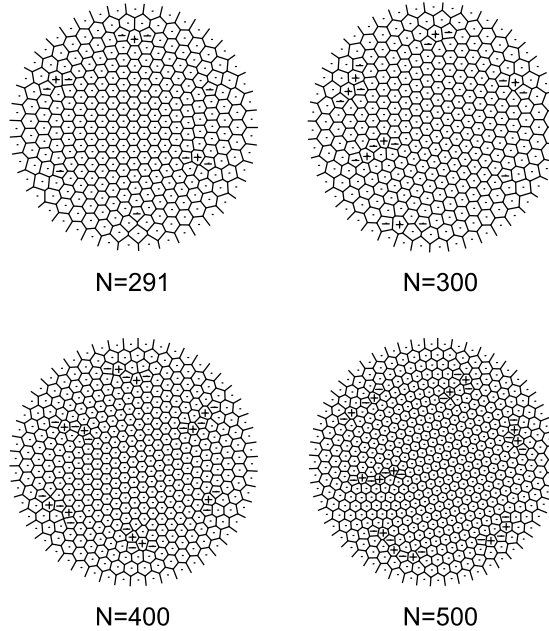


Fig. 3.10 The energy landscape and transition from ground state to metastable states for 9 particles.

### 3.2.3 Large system and topological defect structure

It is well known that the hexagonal lattice is the most energetically favored structure for classical point charges in a two-dimensional infinite plane at low temperature [67, 133]. For a system consisting of a finite number of repelling particles restricted to 2D, which are held together by a circular harmonic potential, the cluster patterns are determined by the need to balance the tendency to form a triangular lattice against the formation of a compact circular shape. The configuration is determined by these two competing effects, namely circular symmetry and triangular structure (Wigner lattice) [70]. This competition leads to intrinsic defects in the 2D circular Coulomb cluster which are *geometry* (of the confinement potential) *induced defects*. This ground state is not a defect-free system. The symmetry breaking is due to the packing of the triangular lattice into a region with a circular boundary. A hexagonal lattice which is cut by a circle without the introduction of any defect has an energy  $E = 56.0499E_0$  which is larger than the ground-state energy  $E = 55.9044E_0$  for  $N = 291$  particles.

We investigate the form and position of the defects in large clusters by the Voronoi construction [127]. The Voronoi construction of a collection of particles consists of a partition of space into cells. Each cell consists of those points which are closer to the given particular particle than to any other particles. Examples of Voronoi constructions are shown in Fig. 3.11 where the ground-state configuration for  $N = 291, 300, 400$  and  $500$  are shown. One can see that there are two kinds of defects, i.e. dislocations and disclinations. Disclinations are orientational defects with five (indicated by ‘-’) or seven (indicated



*Fig. 3.11* The ground state configurations for  $N=291, 300, 400, 500$  particles. The Voronoi structure is shown and the defects (i.e. disclinations) are indicated by ‘+’ for a 7-fold and by ‘-’ for a 5-fold coordination number.

by ‘+’) fold coordination number (the number of sides of the polygon around the particles is nothing else than the coordination number). A dislocation is a pair of two disclinations consisting of a defect with 5-fold (-) and a defect with 7-fold (+) coordination number. In the latter case the ordering at long distances is not disrupted and consequently such a bound pair has a much lower energy [111]. The total number of 5-fold  $N_-$  and 7-fold  $N_+$  disclinations depends on the particular configuration. The number of disclinations in this system is determined by Euler’s theorem and can’t be changed, so the net topological charge  $N_- - N_+$  is always equal to six as was already demonstrated in Refs. [128, 134]. The reason is that every ‘-’ defect can bend the lattice clockwise over  $\pi/3$  from a straight lattice and thus six ‘-’ defects can bend a straight line into a circle. Dislocations will appear when it decreases the energy of the system. From Fig. 3.11 it is apparent that this is more so for larger clusters.

In Refs. [128, 135], the defects in clusters with a logarithmic inter-particle interaction were studied. We want to stress that their way of visualizing the defects is different: nearest neighbours are connected by a line, without

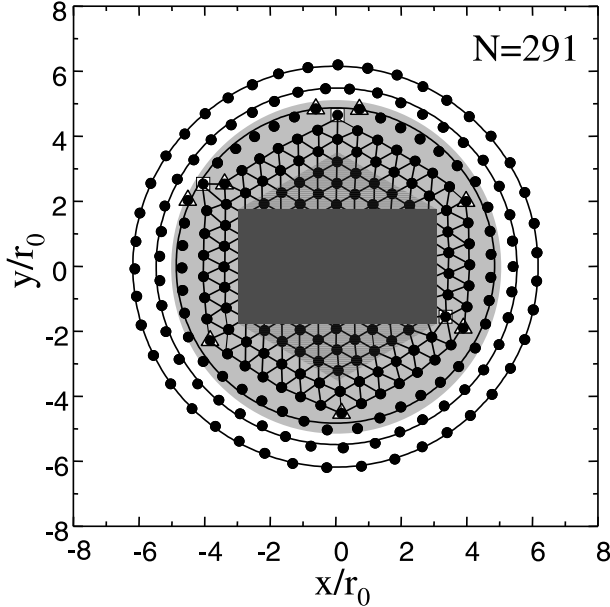


Fig. 3.12 The ground state configuration for  $N = 291$ . The dots give the position of the particles. Three regions are found: I (dark grey colored hexagonal area) is comprised of the defect-free hexagonal lattice; II is a transition region with the defects (light grey colored area), and III consists of the outermost two rings. The ‘+1’ and ‘-1’ topological defects are represented by the open squares and triangles, respectively.

making crossings. However, this does not lead to a unique picture: the total number of 5-fold,  $N_-$ , and 7-fold,  $N_+$ , disclinations can vary in the same configuration, only the net topological charge  $N_- - N_+$  is always equal to six.

In these large clusters, the defects are located on a hexagon, i.e. they form a hexagonal structure. As can be seen in Fig. 3.11 the defects are approximately situated at the six corners of a hexagon, each corner with a net topological charge of ‘-1’. Notice from Fig. 3.11 that a single 5-fold disclination can appear, but never a single 7-fold disclination. For the large strain energy around ‘-1’ topological charge, some dipole defects (i.e. dislocation with ‘-1’ and ‘+1’ defects) will be generated to shield the ‘-1’ topological charge. Those shielding dipole defects do not change the topology of the system.

A clearer example is shown in Fig. 3.12 for the  $N = 291$  ground-state configuration. We considered the  $N = 291$  system as it minimizes the number of defects. The reason is that for this particle number the configuration has 42 particles in the outer ring, which is a multiple of the topological charge. There are three rings at the border with an equal number ( $N = 42$ ) of particles (the 1D Wigner lattice), the central hexagonal structure (the 2D Wigner lattice) and the defects indicated by triangles ( $\triangle$ ) and squares ( $\square$ ) are situated: (i)

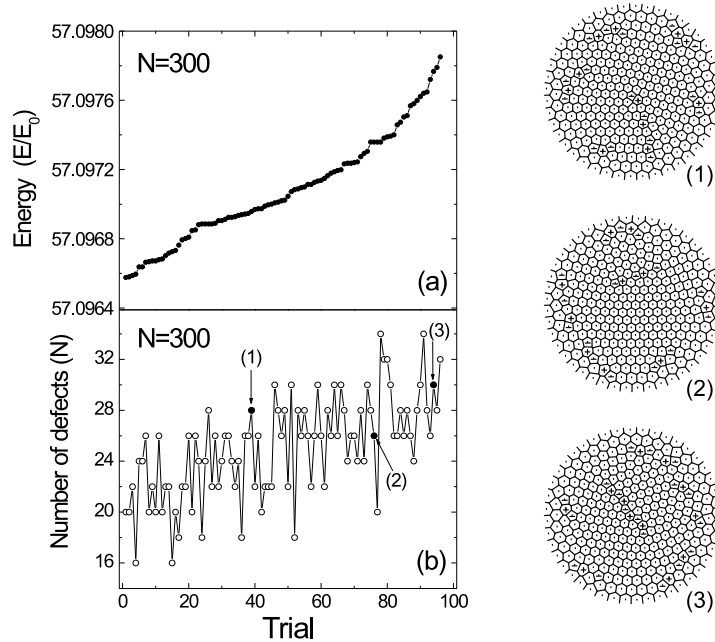


Fig. 3.13 The energy  $E/E_0$  (a) and the total number of defects (b) of different metastable states are shown for  $N = 300$ . Three typical defect configurations with different energy are shown at the right side of the figure.

around the six corners of a hexagon and (ii) in the transition region between the outer rings and the central hexagon.

It should be noted that the search for the global minimum configuration is a difficult problem for large systems because of the existence of a large number of local-minimum configurations, with energy very close to the global minimum. Thus one is never 100% sure to have found the real ground state. Therefore, we investigated the different metastable states. In an experiment, those metastable states may be reached by thermal excitation if the energy barrier between them and the ground state is comparable to or smaller than  $k_B T$ . The saddle points between those metastable states were investigated in an earlier paper [83] for  $N \leq 20$ .

In Fig. 3.13 the energy and the total number of defects of different metastable states are shown for  $N = 300$ . The results for the different metastable configurations are ordered with increasing energy. Note from Fig. 3.13(b) that on average the total number of defects increases with energy, but it shows strong local variations. Only an even number of defects are obtained, because the net topological charge is always six, and the dipole defects (i.e. one disloca-

tion with ‘-1’ and ‘+1’ defects) always appear in pairs. Also the hexagonal position of the defects disappears (see Fig. 3.13(1)) and more free dislocations are found. These defects move from the transition region to the border (see Fig. 3.13(2)) or to the central region (see Fig. 3.13(3)). For configurations with higher energy, the defects arrange themselves in long chains, i.e. dislocation lines. On average the configurations with defects at the border have a lower energy than those with defects in the center.

We also investigated whether or not it is possible to have a configuration with only six 5-fold disclinations and no other defects (like for example for the  $N = 85$  configuration with 24 particles at the outermost ring [134]). Therefore, we started our MC procedure with a perfect hexagonal structure without any defect and then allowed it to relax to its energy minimum. We did this for  $N = 281$  up to 295 particles, because we noted that for these particle numbers the configuration has about 42 particles in the outer ring, which is a multiple of six, i.e. the net topological charge. Only in such a case one can have the situation in which just six 5-fold disclinations are present. We found that our result (from  $N = 281$  up to 295 particles) never converges to a configuration with only six 5-fold disclinations. However, this procedure indeed favorably relaxes to configurations with 42 particles in the outer ring, often resulting in a configuration which has less total number of defects than the corresponding ground-state.

### 3.3 THE YUKAWA INTERACTION POTENTIAL

*Complex plasmas* consist of many strongly-charged dust particles immersed in a gaseous plasma background. The particles in a *Complex plasmas* are strongly coupled and interact through a screened Coulomb potential, i.e., Yukawa potential. The ordered solid phase of dusty plasmas was first predicted theoretically by Ikezi [46] and observed experimentally as *Plasma crystals* [7–10]. The experiment setup and results are already introduced in the first chapter.

The structure of the 2D Yukawa system was studied by several theoretical groups [128, 136]. For a small number of particles (typically  $N < 100$ ) a shell structure was found which compares well with the experiment [68].

Topological defects were also investigated in such a system [61, 128, 135, 137]. Nevertheless, the topological behavior and melting of this system with a Yukawa inter-particle potential has not been investigated in detail. This will be discussed in the following chapter.

In this section we will present the configurational properties of 2D finite Yukawa clusters in a *Complex plasmas*. Firstly, the ground state and the metastable state configurations for the Yukawa system are obtained and compared with the results of a Coulomb, dipole and logarithmic interacting system. Topological defects which are induced by the symmetry of the con-

finement potential will be investigated in larger systems. The saddle point states will be discussed in the next chapter which corresponds to the melting behavior in the *Complex plasmas*.

For a small cluster, particles are packed into concentric shells. Depending on the total number of particles, the functional form of the confining potential, and the mutual repulsion potential, a complicated structure with inner triangular cores surrounded by outer circular shells can be observed [128]. Table 3.1 shows the packing sequences of the ground state for different Yukawa parameter  $\kappa$  for  $N = 4 - 20$  particles. The parameter  $\kappa$  was varied from 0.125 to 8.0. Comparing the configurations for  $\kappa = 0.125$  with the pure Coulomb potential configurations [56], one notices the similarity of the ground-state configuration. However, a slight increase of  $\kappa$  beyond this value can already change the ground state configuration.

Number	$\kappa=0.125$	$\kappa=0.25$	$\kappa=0.5$	$\kappa=1.0$	$\kappa=2.0$	$\kappa=4.0$	$\kappa=8.0$
4	(4)	(4)	(4)	(4)	(4)	(4)	(4)
5	(5)	(5)	(5)	(5)	(5)	(5)	(5)
6	(1,5)	(1,5)	(1,5)	(1,5)	(1,5)	(1,5)	(1,5)
7	(1,6)	(1,6)	(1,6)	(1,6)	(1,6)	(1,6)	(1,6)
8	(1,7)	(1,7)	(1,7)	(1,7)	(1,7)	(1,7)	(1,7)
9	(2,7)	(2,7)	(2,7)	(2,7)	(2,7)	(2,7)	(2,7)
10	(2,8)	(2,8)	(2,8)	(2,8)	(3,7)	(3,7)	(3,7)
11	(3,8)	(3,8)	(3,8)	(3,8)	(3,8)	(3,8)	(3,8)
12	(3,9)	(3,9)	(3,9)	(3,9)	(4,8)	(4,8)	(3,9)
13	(4,9)	(4,9)	(4,9)	(4,9)	(4,9)	(4,9)	(4,9)
14	(4,10)	(4,10)	(4,10)	(4,10)	(4,10)	(4,10)	(4,10)
15	(5,10)	(5,10)	(5,10)	(5,10)	(5,10)	(5,10)	(5,10)
16	(1,5,10)	(1,5,10)	(1,5,10)	(1,5,10)	(1,5,10)	(1,5,10)	(1,5,10)
17	(1,6,10)	(1,6,10)	(1,6,10)	(1,6,10)	(1,6,10)	(1,6,10)	(1,6,10)
18	(1,6,11)	(1,6,11)	(1,6,11)	(1,6,11)	(1,6,11)	(1,6,11)	(1,6,11)
19	(1,6,12)	(1,6,12)	(1,6,12)	(1,7,11)	(1,7,11)	(1,7,11)	(1,6,12)
20	(1,7,12)	(1,7,12)	(1,7,12)	(1,7,12)	(1,7,12)	(1,7,12)	(1,7,12)

*Table 3.1* The configurations for the particle packing sequences for  $N = 4 - 20$  and different screening parameter  $\kappa$ . Here  $\kappa$  is varied from 0.125 to 8.0.

For small  $N \in \{4 - 9\}$ , the parameter  $\kappa$  does not influence the packing of the particles since the confinement dictates the favorable configuration. Table I clearly shows that the structure of the Yukawa clusters with  $N < 10$  is independent of the screening strength  $\kappa$ . Even when  $\kappa$  becomes as large as 8.0, the structure of the cluster is exactly the same as that for the case of  $\kappa = 0$ , only the size of the system is smaller. However, for  $N = 10$  particles the ground state configuration (2,8) will change into (3,7) with increasing  $\kappa$ .

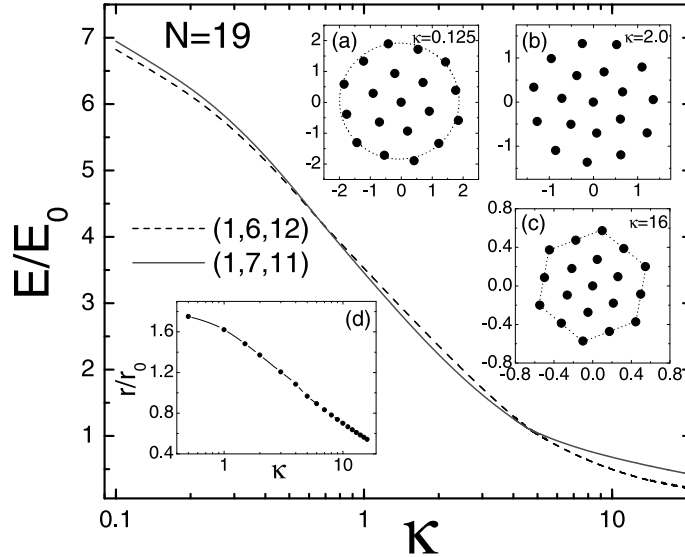


Fig. 3.14 The energy of the  $N = 19$  cluster as a function of the screening parameter  $\kappa$  for two different configurations: (1,6,12) (dashed curve) and (1,7,11) (solid curve). The insets show the ground state configuration for  $N = 19$  particles for (a)  $\kappa = 0.125$ , (b)  $\kappa = 2.0$ , and (c)  $\kappa = 16.0$ .

This is not the case for  $N \in \{11, 13 - 18, 20\}$ , and these configurations appear to be very stable with respect to the screening parameter  $\kappa$ .

To summarize the results of Table 3.1: the screening parameter  $\kappa$  can influence and change the configuration for particular number of particles. With increasing  $\kappa$  the ground state changes from a shell-like structure into a hexagonal lattice, and the radius of the system decreases.

In the following discussion, we focus on the  $N = 19$  system as an interesting example. The energy together with the ground-state configurations for different values of  $\kappa$  are plotted in the insets of Fig. 3.14. One can clearly see that the shell structure for small  $\kappa$  transfers into a hexagonal structure for increased  $\kappa$ . In Fig. 3.14, we plotted the energy of the  $N = 19$  cluster as a function of  $\kappa$  for two states, i.e. with the (1,6,12) and (1,7,11) configuration. Notice that the energy decreases with increasing screening parameter  $\kappa$  because of the decreased radius of the system which decreases the confinement potential energy. When  $\kappa < 0.66$ , the configuration (1,6,12) is the groundstate configuration (see inset Fig. 3.14(a)), while for  $0.66 < \kappa < 4.58$ , the configuration (1,7,11) (see inset Fig. 3.14(b)) becomes the ground state. However, for  $\kappa$  larger than 4.58, a re-entrant behavior of the first ground state is observed (see inset Fig. 3.14(c)). Notice the perfect hexagonal structure for  $\kappa = 16$  in agreement with Ref. [136]. Fig. 3.14(d), one can see that the radius of the system monotonically decreases with increased  $\kappa$ . For large value of  $\kappa$  the

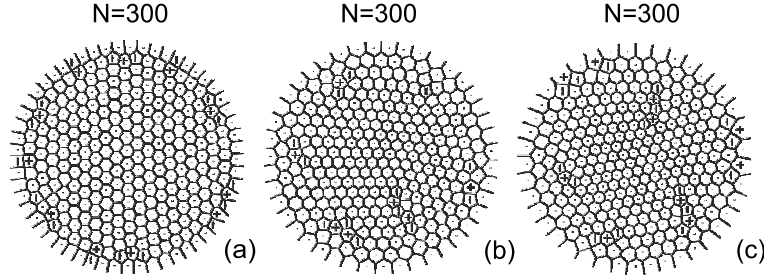


Fig. 3.15 The ground state configurations and the Voronoi construction for  $N=300$  particles with different interaction potentials: (a) for the logarithmic potential  $(-\ln(r_{ij}))$ , (b) for the Coulomb potential  $(1/r_{ij})$  and (c) for the dipole potential  $(1/r_{ij}^3)$ .

particles are located in the central region where the influence of the confinement is very small, and they form a hexagonal structure like in a 2D infinite system.

For larger Yukawa systems, we compare the results with other interparticle potentials in the next section.

### 3.4 NUMERICAL RESULTS FOR OTHER INTERACTION POTENTIALS

We also found that the ground state with the same number of particles but a different interaction potential forms a different configuration and shows a different defect structure [128]. When the interaction potential changes from long range to short range, the defect region will move from the system edge to the center, which is clearly shown Fig. 3.15 for  $N = 300$ : Fig. 3.15(a) corresponds to the logarithmic potential, the defects only appear at the edge; Fig. 3.15(b) corresponds to the pure Coulomb potential, the defects appear in the transition part between the outer rings and the center; Fig. 3.15(c) corresponds to the dipole potential, some defects are situated near the center.

For larger Yukawa systems, we also investigate the topological nature of the cluster structure. When the parameter  $\kappa$  is small, the configuration is similar to the one of a pure Coulomb system ( $\kappa = 0$ ), and large clusters form a hexagonal lattice in the central region with a ring structure near the edge [70]. We make use of the Voronoi construction [127] to picture the cluster structure and to show the coordination number of each of the particles. When those geometry induced defects are present, the net topological charge  $N_- - N_+$  always equals six as was already demonstrated in Ref. [134].

Fig. 3.16, the Voronoi structures are shown as insets for 300 particles with different  $\kappa$  values. Fig. 4.5(a,b,c) show the ground state configurations for

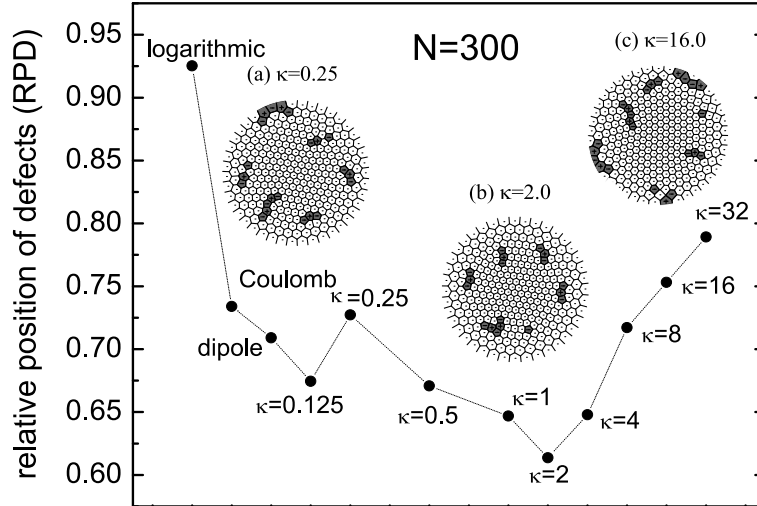


Fig. 3.16 The relative position of the defects (RPD) as a function of  $\kappa$  for  $N = 300$  particles. As a comparison also the results for a logarithmic and dipole interparticle interaction are shown. The ground state configurations for three different values of  $\kappa$  are shown by their Voronoi structures. The defects (i.e. disclinations) are indicated by '+' for a 7-fold and by '-' for a 5-fold coordination number.

$\kappa = 0.25$ ,  $\kappa = 2.0$ , and  $\kappa = 16.0$ , respectively. The location of the defects is strongly influenced by the screening parameter  $\kappa$ . One can see that the defects can move from the edge (Fig. 3.16(a)) to the transition region (between the ring structures and the central region, Fig. 3.16(b)) when  $\kappa$  changes from  $\kappa=0.5$  to  $\kappa=2.0$ . For  $\kappa = 2.0$ , the defects are situated at the six corners of a hexagon, each corner with a single net topological charge. This situation is similar to the case for pure Coulomb inter-particle interaction [138]. Beyond  $\kappa = 4.0$  (see Fig. 3.16(c)) the defect region will move back from the transition area to the edge. Meanwhile the system is reduced in size and the number of particles in the outmost ring changes from: 43 for  $\kappa = 0.25$  to 40 for  $\kappa = 2.0$ , and to 41 for  $\kappa = 16.0$ .

This result is a consequence of the balance between the two competing forces. The cluster patterns are determined by the need to balance the tendency to form a triangular lattice against the formation of a compact circular shape. When increasing  $\kappa$ , the interaction potential will change into a more short-range potential, the defect region is pushed to the center; meanwhile the system radius is reduced. Further increasing the screening parameter  $\kappa$ , the particles move further to the center of the confinement potential reducing its effect, which will squeeze the defect region back to the edge of the system. The same behavior follows from the number of particles in the outmost ring.

This quantity can decrease firstly and increase again while increasing the  $\kappa$  value. In order to measure the relative position of the defects (RPD), we

introduce the following quantity,

$$RPD = \frac{\sum_i^{N_-} r_- + \sum_i^{N_+} r_+}{(N_- + N_+) \cdot R}, \quad (3.2)$$

where  $r_-$  and  $r_+$  denote the position of ‘-’ and ‘+’ defects, respectively,  $R$  is the radius of the system, and  $N_{-(+)}$  is the number of ‘-’ (‘+’) defects. The relative position of the defects for 300 particles with different inter-particle interaction is shown in Fig. 4.5. For the purpose of comparison, the RPD of the long range logarithmic potential, the dipole potential and the Coulomb potential between particles are also shown [139]. Notice that initially the position of the defects moves from the edge of the cluster towards the inner part of the cluster with decreasing range of the inter-particle interaction. A local minimum is reached for  $\kappa \approx 0.125$ . In the range  $\kappa = 0 \rightarrow \kappa = 0.25$  the RPD varies by at most 8%. A pronounced minimum in RPD is found for  $\kappa \approx 2$  where the defects are situated around  $(2/3)R$ . This figure nicely illustrates the effect of the interplay between the confinement potential and the inter-particle potential on the position of the geometry induced topological defects.

### 3.5 HARD WALL CONFINEMENT

Most of such Wigner-like ordering studies focus on systems with an external parabolic confinement, which is similar to the action of a uniform neutralizing background of charges. Other type of confinements which have also been considered are those residing from a fixed positive charge. Such a positive charge keeps the repelling charged particles together, and is in fact the classical analog for atoms [115, 116]. An extreme case of confinement is the one consisting of a *hard wall*. Interesting re-entrant melting behavior was observed for colloidal particles dissolved in water [6, 82] in such a hard wall potential, which is absent in a parabolic confined system. The radial particle fluctuations are responsible for an enhanced locking of adjacent shells [81]. In fact the short range interparticle interaction in combination with the hard wall confinement leads to the unusual reentrant behavior in its orientational order. In Refs. [70, 81] the melting of some specific clusters was investigated theoretically, but no systematic study of the ground state and normal modes was made. Such a study will be presented here, which is further motivated by the fact that in a hard wall confined system the physics is very different, e.g. 1) there is a very inhomogeneous distribution of particles because many of them are pushed to the edge of the system where they create a non-parabolic confinement potential for the other particles; and 2) the average particle density is unaltered with varying inter-particle interaction which is different for parabolic confine-

ment where the density increases with decreasing inter-particle interaction strength.

### 3.5.1 Small clusters

Unlike for the parabolic confinement case with Coulomb interparticle interactions, the particles are not attracted to the center of the confinement potential but they repel each other such that they move to the edge of the system. In this case, the previously [70] found simple polygons are formed at the edge. For a cluster with a small number of particles, one concentric shell at the edge will form and the center region will be empty, while for a large number of particles the center region will resemble a triangular lattice, however the shell structure stays more pronounced than for the parabolic case.

Table 3.2 shows the packing sequences of the ground state for  $N = 2, 3, \dots, 50$  with different inter-particle interactions, including the Coulomb, dipole and screened Coulomb (for  $\kappa = 0.5, 2.0, 4.0$ ) cases. The configuration is indicated by the number of particles in the different rings. The energy per particle  $E/N$  is also given. This table is rather exhaustive and should be compared with a similar one published in Ref. [70, 128] for the parabolic confinement potential.

Firstly, we discuss the case for Coulombic interparticle interaction. From Table 3.2, we can see how shells are filled by the particles and new shells appear. For small  $N \in \{2 - 11\}$ , the particles are situated at the edge of the wall. When a critical number of particles at the edge is achieved, a new shell appears. This occurs for  $N = 12$  and is, as said above, independent of the radius of the confinement potential. From  $N \in \{12 - 29\}$ , the system has a two shell structure. One interesting phenomenon can be observed in such a hard wall case. When there are two shells, the edge is always the preferable position for the new particles. New particles will begin to join into the center shell only if the edge reaches a critical number of particles. When the inner ring has six particles a third ring is created. This occurs for  $N \in \{30 - 50\}$ . Note that this is different from the parabolic confinement case where a new shell forms when the inner ring is filled with five particles.

It was shown in Ref. [128] that for a system with parabolic confinement the configurations do not differ very strongly for short or long range interactions, in contrary to what we find for the hard-wall case. This is nicely illustrated in Table 3.2 if we compare the dipole and Yukawa (with different screening lengths) with the Coulomb case. Note also that the configuration for  $N = 29$  in the case of dipole interaction, namely  $(3, 9, 17)$  corresponds with the experimentally observed configuration in Refs. [6, 82]. For the Yukawa system, the structure is strongly dependent on the screening strength  $\kappa$ . For a small value of  $\kappa = 0.5$  the structure of the system is quite similar to the pure Coulomb case (see the third and sixth column in Table 3.2. When increasing  $\kappa$ , one can see that more and more particles can appear in the center region. The table also shows that for more short-range inter-particle interactions new shells

N	E/N (Coulomb)	Configuration (Coulomb)	E/N (Dipole)	Configuration (Dipole)	Configuration (Yukawa)		
					$\kappa = 0.5$	$\kappa = 2.0$	$\kappa = 4.0$
2	0.25000	2	0.06250	2	2	2	2
3	0.57735	3	0.19245	3	3	3	3
4	0.95711	4	0.41605	4	4	4	4
5	1.37639	5	0.76085	5	5	5	5
6	1.82735	6	1.25495	6	6	6	6
7	2.30477	7	1.92680	7	7	7	1,6
8	2.80487	8	2.56095	1,7	8	1,7	1,7
9	3.32483	9	3.38223	1,8	9	1,8	1,8
10	3.86245	10	4.42647	1,9	10	1,9	1,9
11	4.41597	11	5.63037	2,9	1,10	1,10	2,9
12	4.96464	1,11	6.84760	2,10	1,11	2,10	2,10
13	5.52365	1,12	8.14532	3,10	1,12	2,11	3,10
14	6.09624	1,13	9.55674	3,11	1,13	2,12	3,11
15	6.68141	1,14	11.11835	4,11	1,14	3,12	4,11
16	7.27826	1,15	12.73777	4,12	2,14	3,13	4,12
17	7.87157	2,15	14.60145	5,12	2,15	4,13	5,12
18	8.47100	2,16	16.44619	5,13	3,15	4,14	5,13
19	9.07868	3,16	18.56347	1,5,13	3,16	4,15	5,14
20	9.68150	3,17	20.61187	1,6,13	3,17	5,15	1,5,14
21	10.29425	3,18	22.62037	1,6,14	4,17	5,16	1,6,14
22	10.91463	4,18	24.96092	1,6,15	4,18	1,5,16	1,6,15
23	11.53049	4,19	27.26438	1,7,15	4,19	1,5,17	1,7,15
24	12.15533	4,20	29.87944	1,7,16	5,19	1,6,17	1,7,16
25	12.78663	5,20	32.54436	1,8,16	5,20	1,6,18	1,7,17
26	13.41427	5,21	35.27964	2,8,16	5,21	1,7,18	1,8,17
27	14.05013	5,22	38.10941	2,8,17	6,21	1,7,19	2,8,17
28	14.69087	6,22	40.97470	3,8,17	1,6,21	1,7,20	2,8,18
29	15.32924	6,23	43.81985	3,9,17	1,6,22	1,8,20	3,8,18
30	15.96932	1,6,23	46.82763	3,9,18	1,6,23	1,8,21	3,9,18
31	16.61023	1,6,24	50.03572	4,9,18	1,7,23	2,8,21	3,9,19
32	17.25843	1,6,25	53.20328	4,10,18	1,7,24	2,8,22	3,9,20
33	17.90323	1,7,25	56.45567	4,10,19	1,7,25	3,8,22	4,9,20
34	18.55396	1,7,26	59.96733	4,11,19	1,8,25	3,9,22	4,10,20
35	19.20978	1,8,26	63.51491	5,11,19	1,8,26	3,9,23	4,10,21
36	19.86301	1,8,27	67.00782	5,11,20	2,8,26	3,10,23	4,11,21
37	20.52278	1,8,28	70.81054	1,5,11,20	2,8,27	3,10,24	5,11,21
38	21.18212	2,8,28	74.53620	1,6,11,20	2,9,27	4,10,24	5,11,22
39	21.84389	2,8,29	78.22570	1,6,12,20	2,9,28	4,10,25	1,5,11,22
40	22.50297	2,9,29	81.89272	1,6,12,21	3,9,28	4,11,25	1,5,11,23
41	23.16711	2,9,30	85.98871	1,6,12,22	3,9,29	4,11,26	1,6,11,23
42	23.82918	3,9,30	90.01315	1,6,13,22	3,10,29	5,11,26	1,6,12,23
43	24.49545	3,9,31	94.05687	1,7,13,22	3,10,30	5,11,27	1,6,12,24
44	25.16090	3,10,31	98.43269	1,7,13,23	4,10,30	5,12,27	1,6,13,24
45	25.82957	3,10,32	102.7506	1,7,14,23	4,10,31	1,5,12,27	1,6,13,25
46	26.49958	4,10,32	107.3208	1,8,14,23	4,11,31	1,5,12,28	1,7,13,25
47	27.17037	4,10,33	111.7210	2,8,14,23	4,11,32	1,6,12,28	1,7,13,26
48	27.84116	4,11,33	116.2977	2,8,14,24	5,11,32	1,6,12,29	1,7,14,26
49	28.51431	4,11,34	120.9331	3,8,14,24	5,11,33	1,6,13,29	1,8,14,26
50	29.19165	5,11,34	125.5184	3,8,15,24	5,12,33	1,6,13,30	2,8,14,26

Table 3.2 The ground state for  $N = 2, 3, \dots, 50$  particles confined in a 2D hard wall with coulomb, dipole and screened Coulomb inter-particle interaction, respectively. The energies ( $E/N$ ) and the shell structures ( $N_1, N_2, \dots$ ) of the ground state configuration are shown.

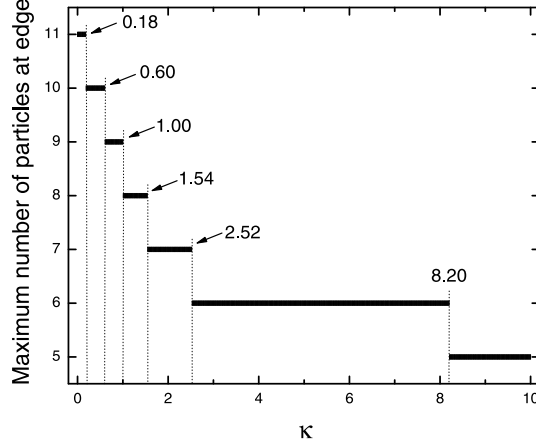


Fig. 3.17 The maximum number of particles at the edge of the hard wall confinement before one particle is situated in the center as a function of the interaction strength  $\kappa$ .

are formed for lower  $N$ -values. This is not surprising because the inter-particle interaction is diminished while the size of the system is not (in contrast to the parabolic case where the size of the system becomes smaller with increasing  $\kappa$  [56, 136]).

We investigated in more detail how many particles can be placed at the edge before one of the particles is placed in the center, in case of a screened Coulomb inter-particle interaction. The energy of the configuration with  $N$  particles equidistantly placed on a single ring at the edge is given by

$$E_{\circ} = \sum_{i=1}^{N-1} \sum_{j=i+1}^N \frac{e^{-2\kappa |\sin \frac{\pi(i-j)}{N}|}}{2 |\sin \frac{\pi(i-j)}{N}|}, \quad (3.3)$$

and the energy of  $N - 1$  particles at the edge with 1 in the center is given by

$$E_{\odot} = \sum_{i=1}^{N-2} \sum_{j=i+1}^{N-1} \frac{e^{-2\kappa |\sin \frac{\pi(i-j)}{N-1}|}}{2 |\sin \frac{\pi(i-j)}{N-1}|} + (N-1)e^{-\kappa}. \quad (3.4)$$

The maximum value of  $N$  for which  $E_{\circ} < E_{\odot}$ , is the maximum number of particles at the edge. This value is shown in Fig. 3.17 as a function of  $\kappa$ . For  $\kappa > 8.2$  the sixth particle always goes to the center.

Another pronounced difference in the configuration for a Yukawa system can be observed. In the parabolic case, the ground state configuration changes from a shell-like structure into a hexagonal lattice with increasing  $\kappa$  [56, 136]. For hard wall confinement the radius of the system does not change and the configuration stays shell-like, even up to large  $\kappa$  values.

The case with logarithmic inter-particle interaction was considered as well. We did not add the result to Table 3.2, since the configuration is always a

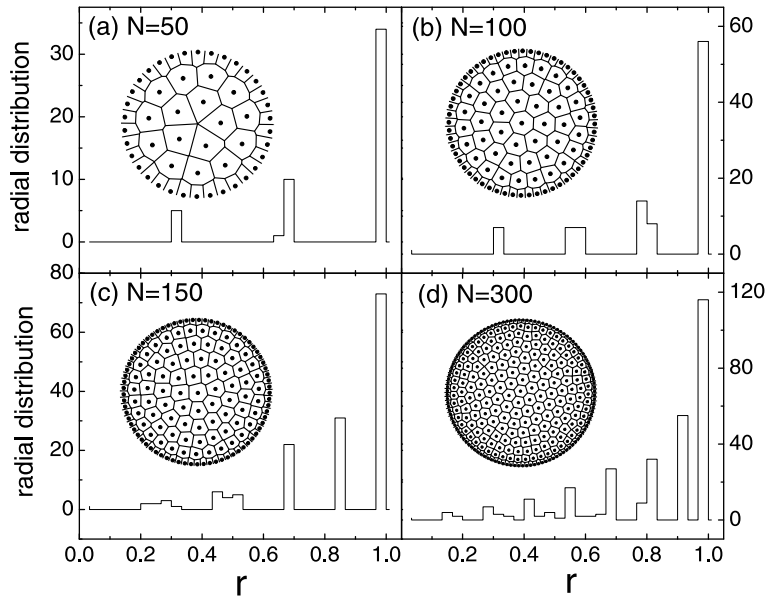


Fig. 3.18 The radial distribution for systems with  $N = 50, 100, 150$  and  $300$  particles. The insets show the configurations and their Voronoi structures.

single shell, which is a consequence of Earnshaw's theorem [140, 141] in two dimensions. The interaction potential is long range, and all particles are situated at the edge of the hard wall.

### 3.5.2 Large clusters

For large systems the configuration is determined by two competing effects, namely, circular symmetry and triangular structure (Wigner lattice). The radial distributions together with the configurations for  $N = 50, 100, 150$  and  $300$  are shown in Fig. 3.18 and this shows that for  $50, 100$  and  $150$  particles a clear shell structure is present. For  $N = 50$  particles (see Fig. 3.18(a)), there are three shells and the configuration is  $(5, 11, 34)$ . For  $N = 100$  particles (see Fig. 3.18(b)), one particle is situated in the center with four shells around it with the configuration  $(1, 7, 14, 22, 56)$ , and for  $N = 150$  (see Fig. 3.18(c) with configuration  $(1, 8, 15, 22, 31, 73)$ ) one more ring is present. Fig. 3.18(d) shows the configuration for  $N = 300$ . Notice that only the outer shells have a well-defined radius while the inner shells have no clear radius, reflecting that the inner region has a more triangular-lattice-like structure which can also be seen from the Voronoi construction in the inset of Fig. 3.18(d). In the parabolic case (and for Coulombic interaction), a triangular structure starts to appear in the center already for about  $100$  particles [70], while for the hard-wall

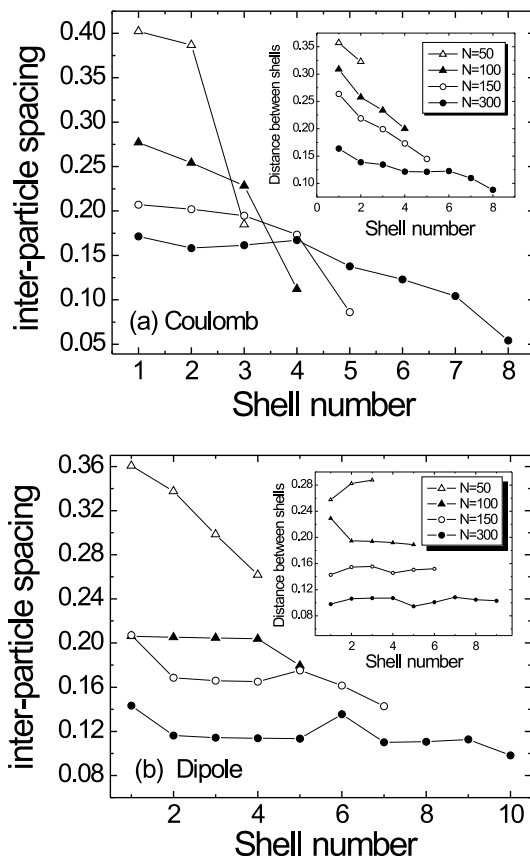


Fig. 3.19 The interparticle spacing within the shell as a function of the shell number for  $N = 50, 100, 150,$  and  $300$  particles interacting through the (a) Coulomb and (b) dipole interaction potential for hard wall confinement. The insets show the distance between shells as a function of the shell number.

system a triangular lattice appears in the central region for  $N \gtrsim 300$ . Also the outer shell structure is more pronounced than for parabolic confinement. Note however that in our hard wall system many particles are situated at the edge, for example for the  $N = 300$  system the outer ring consists of  $N_E = 116$  particles. By excluding these edge particles, the triangular lattice in the center starts to appear from  $300 - N_E = 184$ , which is already closer to but still larger than for the parabolic confinement case.

It was shown before that the topological charge in case of a parabolically confined system is always  $-6$  and that the position of the defects for large systems is in the transition region between the outer rings and the central triangular lattice [138]. The number of defects for the hard wall system is much

larger and are now also situated near the edge, but still the total topological charge always equals  $-6$ .

On each shell, the particles are equally distributed. Unlike the parabolic confinement case with Coulomb interaction, for hard wall confinement the interparticle spacing in a shell decreases with increasing shell number. Those results are shown in Fig. 3.19(a). The inset in Fig. 3.19(a) shows the distance between shells for  $N = 50, 100, 150$ , and  $300$  particles. One can see that the distance between shells always decreases from the inner shell to the outer shell. Both effects together make that the density increases from the center to the edge, in contrast to the parabolic confinement case [70].

It is interesting to compare the results for our hard wall system with Coulomb interacting particles with a more short-range interaction like the dipole inter-particle potential. Fig. 3.19(b) shows the interparticle spacing in the different shells for the dipole system. One can see that it does not depend strongly on the shell number. The same is true for the distance between the shells, as shown in the inset of Fig. 3.19(b). As a result, the particles are more uniformly distributed in the case of the short-range dipole interaction than for the long-range Coulomb interaction. This is again a consequence of the fact that for more short-range inter-particle interactions, particles appear in the center at lower  $N$ -values.

### 3.6 CONCLUSIONS

In this chapter, we presented the results of our numerical calculations for the configurations of the ground and metastable states and their energies, for a system consisting of classical 2D charged particles that are confined in a parabolic confinement potential. Both small and large clusters are considered.

In most papers, one concentrates on the study of the minima in the energy landscape while the barriers between those minima are left out of the discussion. Here the saddle point states, which are the critical states in the transition between the ground state and the metastable states, are studied, from which the potential barriers are obtained.

Sensitivity of the configuration on the form of the confinement potential and the interparticle interaction is investigated and a phase diagram is obtained. This sensitivity on e.g., the form of the confinement potential is probably the explanation why some of the recently found experimental configurations[29] differs from our simulation results.

For a large number of particles in the cluster ( $N > 150$ ) the configuration is determined by two competing effects, namely in the center a hexagonal lattice is formed, which is the ground-state for an infinite 2D system, and the confinement which imposes its circular symmetry on the outer edge. As a result a hexagonal Wigner lattice is formed in the central area while at the border of the cluster the particles are arranged in rings. In the transition

region defects appear as dislocations and disclinations at the six corners of the hexagonal-shaped inner domain. The particles motion is found to be strongly related to the topological structure. The relation between the topological defect and melting of the cluster will be discussed in the following chapter.

For the Yukawa potential in a complex plasma, we find that for a small number of particles, the ground-state configuration consists of a ring structure which transforms into a hexagonal structure with increasing screening parameter  $\kappa$ . For large clusters, geometry induced defects appear and the location of the defects depends on  $\kappa$ . For logarithmic and strongly screened inter-particle interaction those defects occur near, or at the boundary of the cluster. For  $\kappa = 2$  the defects are found deepest inside the cluster near  $(2/3)R$ .

In a hard wall confinement, the configurational properties of 2D clusters show an inhomogeneous distribution and more particles can sit at the edge in comparison with the parabolic case, and the shell structure is much more pronounced, also for large clusters. In the case of long-range Coulomb interaction between the particles, the density of particles is increased towards the edge, while the particles are more uniformly distributed for a short-range interaction potential like e.g. for the dipole interaction.

**Publications.** The results presented in this chapter were published as:

- Minghui Kong, B. Partoens, and F. M. Peeters, *Transition Between Ground State and Metastable States in Classical 2D Atoms*, Phys. Rev. E **65**, 046602 (2002) (13 pages).
- Minghui Kong, B. Partoens and F. M. Peeters, *Topological defects and Non-homogeneous melting of large 2D Coulomb Clusters*, Phys. Rev. E **67**, 021608 (2003) (8 pages).
- Minghui Kong, B. Partoens, and F. M. Peeters, *Structural, dynamical and melting properties of two-dimensional Clusters of Complex Plasmas*, New Journal of Physics **5**, 23 (2003) (17 pages).
- F. M. Peeters, Minghui Kong and B. Partoens, *Geometry induced defects in a confined Wigner lattice*, the third international conference on the physics of dusty plasmas: Dusty Plasmas in the New Millennium, edited by R. Bharuthan et al. (AIP Conf. Proc. Vol 649) (New York: American Institute of Physics) p. 192-195 (2002) (4 pages).
- Minghui Kong, B. Partoens, A. Matulis and F. M. Peeters, *Structure and spectrum of two-dimensional clusters confined in a hard wall potential*, Phys. Rev. E **69**, 036412 (2004) (10 pages).

## 3.7 APPENDIX A - TABLE I

N	E/N	$\Delta E/N$ ( $E_{\text{metastable}} - E_{\text{groundstate}})/N$	Configuration	Radius of the ring	Width of ring	Lowest Eigenfrequency		
						1	2	3
1	–	–	1	–	–			
2	0.75000	–	2	0.50000	0	1.41421	2.44949	
3	1.31037	–	3	0.66090	0	1.41421	1.73205	2.44949
4	1.83545	–	4	0.78219	0	1.25189	1.41421	1.86483
5	2.33845	–	5	0.88288	0	1.02886	1.41421	1.94009
	2.36556	0.02711	1,4	0 0.99280	0			
6	2.80456	–	1,5	0 1.05916	0	0.91889	1.41421	1.72935
	2.82476	0.02020	6	0.96968	0.07205			
7	3.23897	–	1,6	0 1.12232	0	1.09890	1.41421	1.45239
8	3.66890	–	1,7	0 1.18223	0	1.10688	1.22689	1.41421
9	4.08812	–	2,7	0.43211 1.30184	0.02724 0.16201	0.12681	0.77540	0.91669
	4.09426	0.00614	1,8	0 1.23909	0			
10	4.48494	–	2,8	0.42649 1.34879	0 0.17677	0.08910	0.97483	0.98520
	4.48816	0.00322	3,7	0.56774 1.41293	0.05311 0.14064			
11	4.86467	–	3,8	0.56042 1.45220	0.00270 0.14305	0.02451	0.73727	0.83817
12	5.23894	–	3,9	0.55937 1.48975	0 0.14650	0.53084	0.89022	1.15011
	5.24204	0.00310	4,8	0.66623 1.54800	0 0.10544			
13	5.60114	–	4,9	0.66200 1.58123	0.00176 0.11547	6.002E-4	0.75236	0.75546
14	5.95898	–	4,10	0.65950 1.61368	0.01385 0.13137	0.04940	0.79446	0.84578
	5.96269	0.00371	5,9	0.75410 1.66586	0.00947 0.07368			
15	6.30758	–	5,10	0.75105 1.69402	0 0.09015	0.45989	0.68255	0.75956
	6.31554	0.00796	1,5,9	0.02923 0.91617 1.74361	0.04167 0.11835			
16	6.64990	–	1,5,10	0 0.91101 1.76825	0 0.14050	0.49237	0.66241	0.92179
	6.65235	0.00245	5,11	0.74717 1.72320	0.00441 0.12766			
	6.65619	0.00629	1,6,9	0 0.97881 1.81945	0.06197 0.03724			
17	6.98290	–	1,6,10	0 0.96956 1.84176	0 0.00552 0.07609	0.05416	0.54796	0.55927
	6.98433	0.00143	1,5,11	0.00536 0.90549 1.79481	0.00657 0.16168			
18	7.30814	–	1,6,11	0.00300 0.96447 1.86476	0.00653 0.10514	0.00614	0.65492	0.67820

	7.31522	0.00708	1,7,10	0 1.02998 1.90946	0.06694 0.02564			
19	7.63193	-	1,6,12	0 0.96261 1.88679	0 0.13692	0.66759	0.70531	1.09892
	7.63280	8.7E-4	1,7,11	1.12602E-4 1.02314 1.93083	0.00329 0.05476			
20	7.94961	-	1,7,12	0 1.01819 1.95219	0.00619 0.07245	1.031E-4	0.62728	0.69260
	7.95623	0.00662	1,6,13	0.01041 0.95822 1.91011	0.00777 0.21495			
21	8.26588	-	1,7,13	0.00142 1.01487 1.97328	0.01000 0.13711	0.00317	0.63738	0.71452
	8.26645	5.7E-4	2,7,12	0.39273 1.12744 2.01192	0.03627 0.19935 0.15137			
	8.26756	0.00168	1,8,12	0 1.07321 2.01156	0.18661 0.11052			
22	8.57418	-	2,8,12	0.39458 1.17613 2.06959	0 0.27077 0.10297	0.29341	0.40180	0.55690
	8.57568	0.00150	2,7,13	0.38900 1.12400 2.03144	0 0.19724 0.18137			
23	8.87758	-	2,8,13	0.38885 1.16958 2.08895	0.00118 0.24227 0.14446	0.12867	0.40830	0.58505
	8.87859	0.00101	3,8,12	0.50794 1.27214 2.12689	0.05120 0.26208 0.12204			
24	9.17590	-	3,8,13	0.50417 1.26512 2.14415	0.00326 0.19163 0.14418	0.02762	0.40652	0.55310
	9.17756	0.00166	3,9,12	0.51335 1.31367 2.17908	0 0.22226 0.09571			
	9.17987	0.00397	2,8,14	0.38911 1.16535 2.10691	0 0.24188 0.16950			
25	9.47079	-	3,9,13	0.50710 1.30505 2.19669	0.01278 0.19944 0.11122	0.11377	0.50320	0.52713
	9.47292	0.00213	3,8,14	0.50283 1.26038 2.16111	0.00983 0.17317 0.15226			
	9.47485	0.00405	4,8,13	0.60037 1.35438 2.19750	0.02163 0.15541 0.13994			
26	9.76273	-	3,9,14	0.50452 1.29914 2.21296	0.00244 0.18436 0.12611	0.10409	0.56681	0.61503
	9.76383	0.00110	4,9,13	0.59791 1.39030 2.24911	0.03559 0.15296 0.05624			

27	10.05086	–	4,9,14	0.59494 1.38378 2.26391	0.01026 0.13764 0.12630	0.01311	0.37880	0.56307
	10.05273	0.00187	4,10,13	0.59876 1.42670 2.29743	0.06133 0.17691 0.10036			
	10.05382	0.00296	3,9,15	0.50456 1.29489 2.22843	0 0.19007 0.14683			
28	10.33562	–	4,10,14	0.59556 1.41936 2.31219	0.02917 0.16578 0.07189	0.05682	0.17410	0.47678
	10.33778	0.0022	4,9,15	0.59259 1.37843 2.27922	0.01374 0.12710 0.12678			
29	10.61807	–	4,10,15	0.59296 1.41346 2.32654	0.02873 0.15640 0.12364	0.03911	0.12706	0.57988
	10.61926	0.00119	5,10,14	0.67955 1.49439 2.35987	0.05418 0.14576 0.08672			
	10.6204	0.00236	4,11,14	0.60235 1.45375 2.35715	0.01961 0.34364 0.20754			
30	10.89732	–	5,10,15	0.67715 1.48825 2.37299	0 0.11070 0.10212	0.29745	0.48458	0.56208
	10.89852	0.00121	4,11,15	0.60536 1.44557 2.36996	0.05952 0.47214 0.31619			
	10.89999	0.00268	1,5,10,14	0.02842 0.82995 1.56500 2.40474	0.04494 0.19679 0.12020			
31	11.17388	–	5,11,15	0.67540 1.52072 2.41797	0.03417 0.13067 0.09374	0.02351	0.11182	0.27895
	11.17433	4.52E-04	1,5,10,15	0 0.82568 1.55780 2.41745	0 0.16498 0.13735			
	11.17541	0.00153	1,5,11,14	0.13069 0.84077 1.60637 2.43703	0.31263 0.63425 0.13594			
	11.17559	0.00171	5,10,16	0.67428 1.48265 2.38703	0.01149 0.12077 0.12035			
32	11.44658	–	1,5,11,15	0.01272 0.82275 1.58794 2.46152	0.00963 0.18210 0.13245	0.02971	0.18804	0.45106
	11.44793	0.00135	5,11,16	0.67326 1.51515 2.43064	0.01889 0.13987 0.11569			
33	11.71564	–	1,6,11,15	0.00316 0.87730 1.65369 2.50507	0.02335 0.13683 0.08796	0.06805	0.21724	0.41934

	11.71703	0.00139	1,5,11,16	0.00620 0.81977 1.58187 2.47350	0.01483 0.17523 0.14325			
	11.71864	0.00300	1,6,10,16	0 0.87529 1.62032 2.47485	0.00187 0.11129 0.12766			
34	11.98262	-	1,6,12,15	0 0.87864 1.68144 2.54493	0.02189 0.17867 0.09451	0.23793	0.35495	0.78177
	11.98289	0.00027	1,6,11,16	0.00556 0.87354 1.64704 2.51654	0.00939 0.13013 0.12010			
	11.98558	0.00296	1,7,11,15	0.00468 0.93261 1.71734 2.54667	0.06001 0.12580 0.01855			
	11.98727	0.00465	1,5,11,17	0.01113 0.81719 1.57679 2.48571	0.00832 0.18416 0.15459			
35	12.24693	-	1,6,12,16	0 0.87504 1.67373 2.55657	0.00112 0.16105 0.10515	0.06585	0.46277	0.47916
	12.24981	0.00288	1,6,11,17	0.00451 0.87146 1.64141 2.52794	0.01293 0.14624 0.13569			
	12.25002	0.00309	1,7,11,16	0.00420 0.92801 1.70941 2.55834	0.02655 0.09325 0.09193			
	12.25101	0.00408	1,6,13,15	0.01461 0.87903 1.71046 2.58316	0.10204 0.32812 0.12484			
36	12.51081	-	1,6,12,17	0.00184 0.87232 1.66764 2.56767	0.00155 0.16141 0.12828	0.00895	0.52837	0.53908
	12.51106	0.00025	1,7,12,16	0.00410 0.92629 1.73496 2.59790	0.02221 0.10248 0.06247			
	12.51242	0.00161	1,6,13,16	0.00514 0.87411 1.70182 2.59536	0.03819 0.23524 0.13364			
	12.51353	0.00272	1,7,13,15	0.04708 0.93104 1.77162 2.62285	0.11122 0.29709 0.09392			
37	12.77190	-	1,7,12,17	6.69934E-5 0.92319 1.72858 2.60841	0.01460 0.09282 0.09598	0.00321	0.26342	0.4995

	12.77237	0.00047	1,7,13,16	0.00222 0.92651 1.76093 2.63574	0.03263 0.16786 0.08191			
	12.77322	0.00132	1,6,13,17	0.01850 0.87539 1.69396 2.60500	0.09154 0.43213 0.31271			
38	13.03045	–	1,7,13,17	0.00193 0.92338 1.75392 2.64616	0.01505 0.14065 0.09887	0.00613	0.16459	0.46835
	13.03251	0.00206	2,7,13,16	0.39101 1.03060 1.81565 2.67072	0.29219 0.28147 0.46806 0.29041			
	13.03283	0.00238	2,7,12,17	0.38939 1.02573 1.78253 2.64551	0.36450 0.26924 0.37577 0.27405			
	13.03310	0.00265	1,7,14,16	0.00104 0.92882 1.78630 2.67136	0.04978 0.28209 0.13476			
	13.03330	0.00285	1,8,12,17	0.04854 0.97547 1.78442 2.64648	0.29342 0.18298 0.14053			
39	13.28790	–	2,7,13,17	0.38350 1.02814 1.80664 2.68158	0.29403 0.23971 0.45865 0.34537	0.22264	0.31318	0.36571
	13.28822	0.00032	1,7,13,18	0.00341 0.92117 1.74784 2.65621	0.02846 0.19498 0.15742			
	13.28847	0.00057	1,7,14,17	5.51205E-4 0.92531 1.77850 2.68185	0.02216 0.24325 0.15440			
	13.28943	0.00153	2,7,14,16	0.36469 1.03296 1.84277 2.70610	0.00384 0.25912 0.40141 0.14410			
40	13.54192	–	2,8,13,17	0.36712 1.06839 1.86379 2.72046	0.04211 0.29836 0.26452 0.11180	0.12420	0.23757	0.31601
	13.54228	0.00036	2,8,14,16	0.38177 1.07381 1.89825 2.74124	0 0.35609 0.37389 0.12705			
	13.54313	0.00121	2,7,13,18	0.36081 1.02386 1.80203 2.69285	0 0.22699 0.29722 0.23060			
	13.54359	0.00167	1,2,8,14,17	0.29641 0.61782 1.08838 1.82482 2.71541	0.19559 0.20627 0.56223 0.3553			

*Table 3.3* The ground state and the metastable states for  $N=1, \dots, 40$  Coulombic particles confined in a 2D parabolic well. We give the energies ( $E/N$ ),  $\Delta E/N$ , the shell structure ( $N_1, N_2, \dots$ ), the radius and width of the shell, and the lowest three normal mode frequencies of the ground state configuration. The energy is in units of  $E_0$ , the coordinate is in units of  $r_0$  and the frequency is in units of  $\omega_0/\sqrt{2}$ .

## 3.8 APPENDIX B - TABLE II

Number of Particles (N)	Energy of Ground state	Energy of Metastable state	Energy of Saddle point
1	-	-	-
2	0.75000	-	-
3	1.31037	-	1.46201
4	1.83545	-	1.92064
5	2.33845	2.36556	2.36829
6	2.80456	2.82476	2.82477, 2.82689
7	3.23897	-	3.27913, 3.28592
8	3.66890	-	3.68738, 3.68957
9	4.08812	4.09426	4.08813, 4.09530 4.10628
10	4.48494	4.48816	4.48495, 4.48817 4.48940
11	4.86467	-	4.87829, 4.87876 4.88110
12	5.23894	5.24204	5.23955, 5.24209 5.24368
13	5.60114	-	5.61202, 5.61529
14	5.95898	5.96269	5.96335, 5.97235
15	6.30758	6.31554	6.30832, 6.31534 6.31577, 6.31617 6.31689, 6.31702 6.31769, 6.32205
16	6.64990	6.65235 6.65619	6.65117, 6.65490 6.65547, 6.65620 6.65648, 6.65706
17	6.98290	6.98433	6.98614, 6.98978 6.98979, 6.99129 6.99373, 6.99417 6.99441
18	7.30814	7.31522	7.31522, 7.31535 7.31700, 7.32046 7.32095, 7.32154 7.32390
19	7.63193	7.63280	7.63358, 7.63516 7.64155, 7.64258 7.64266, 7.64563
20	7.94961	7.95623	7.95637, 7.95638 7.95639, 7.95640 7.95641, 7.95654 7.95693, 7.95695 7.95709, 7.95725 7.95739, 7.95817 7.96316

Table 3.4 The energies of the ground state, the metastable states and the saddle point states for different number of particles ( $N$ ).



# 4

---

## *Eigenmode Spectrum*

After the discussion of the static properties of a 2D Wigner crystal, we turn to the dynamical properties, i.e. the normal vibration modes of such a crystal. In the next chapter the melting properties will be studied.

Waves and collective oscillations are fundamental dynamical processes which have attracted many scientists' attention. Wigner crystals as a convenient model solid can be used to study the normal mode and wave motion. The normal modes have been obtained from the thermal Brownian motion of the particles around their equilibrium position. The spectral properties of the ground-state configurations were presented in Ref. [55]. The excitation of normal modes of 2D Coulomb clusters was recently observed [47,73] and it agrees well with the theoretical predictions [55]. The mode integrated spectrum shows two broad maxima which are found to be due to "shear-like" and "compression-like" modes [48,55].

The excitation spectrum corresponding to the ground-state configuration of the 2D clusters is discussed in this chapter with different inter-particle interactions (Coulomb potential and Yukawa potential). In a hard wall confinement, the eigenmodes of the cluster are also investigated, which shows different physics in comparison to a parabolically confined cluster.

This chapter is organized as follows. Sec. 4.1 discusses the normal modes for a pure Coulomb system, while Sec. 4.2 is dedicated to the normal modes for a system interacting through a Yukawa potential. In Sec. 4.3, the excitation spectrum of 2D clusters confined in a hard wall potential is discussed. The two-particle problem for a general  $r^n$  confinement potential can be solved exactly and is presented in Sec. 4.4. Sec. 4.5 is devoted to a detailed analysis

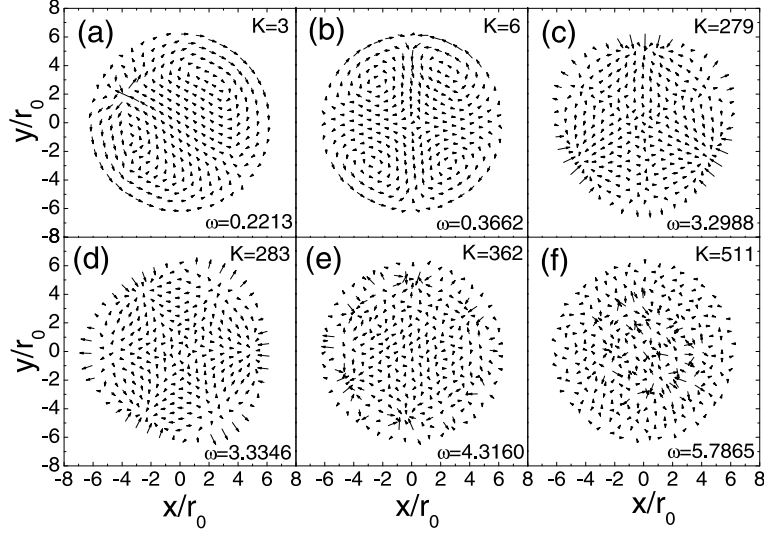


Fig. 4.1 Vector plot of the eigenvectors for the cluster with  $N = 291$  particles for six different values of the mode number  $K$ .

of the radial motion of the particles situated at the edge of the hard wall. Our results are summarized in Sec. 4.6.

#### 4.1 NORMAL MODES IN A PURE COULOMB SYSTEM

To find the excitation spectrum of the cluster we perform a normal mode analysis. By diagonalising the dynamical matrix, one obtains the squared eigenfrequencies of the system. Thus for a cluster of  $N$  particles we have  $2N$  normal modes. In the second chapter we mentioned that after finding the ground-state, we obtain the eigenvalues and eigenvectors of the dynamical matrix

$$H_{\alpha\beta,ij} = \frac{\partial^2 H}{\partial r_{\alpha,i} \partial r_{\beta,j}}$$

[55].

In a pure Coulomb system, it is well known that there are three eigenfrequencies which are independent of  $N$  [55]:  $\omega = 0, \sqrt{2}$  and  $\sqrt{6}$ , which correspond to the rotation of the system as a whole, the center of mass mode and the breathing mode, respectively. The above modes were recently observed experimentally [47, 48, 73]. For small  $N$ ,  $\omega_{min}$  corresponds to inter-shell rotations while for large  $N$  the lowest frequency mode corresponds to a vortex/anti-vortex pair excitation [55]. Configurations with a large value of  $\omega_{min}$  are more stable against deformations and are called the ‘magic number’



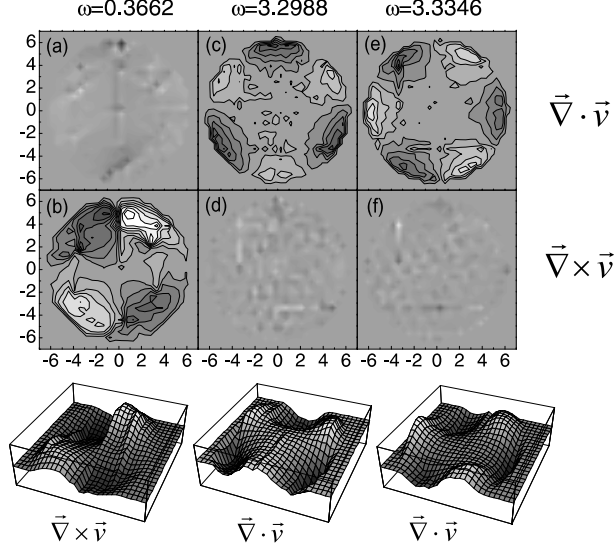


Fig. 4.3 Gray-scale contour maps of the vorticity  $(\vec{\nabla} \times \vec{v})_z$  and the divergence  $\vec{\nabla} \cdot \vec{v}$  of the velocity field of three different eigenmodes. A corresponding 3D plot is shown for those maps which exhibit a clear structure.

the total number of defects present in the ground state. Notice that only an even number of defects are obtained as explained before. On average, configurations with a large number of defects have a smaller lowest eigenfrequency and are thus less stable, and vice versa.

In this 2D lattice, all behaviors of the cluster modes can be classified as shear-like or compression-like modes. In order to characterize the compressional and shear parts of these eigenmodes, we calculated respectively the divergence  $\vec{\nabla} \cdot \vec{v}$  and the vorticity  $(\vec{\nabla} \times \vec{v})_z$  of the velocity field. To calculate the velocity field, we interpolated the displacements of Fig. 4.1 on a  $100 \times 100$  grid (thus neglecting the constant eigenfrequency). The “divergence and vorticity maps” were then calculated at every point of this matrix. Notice that pure shear or compressional modes do not exist in the circular boundary of finite cluster. Fig. 4.3(b) shows the vorticity and thus displays the shear part of the eigenmode of Fig. 4.1(b). The two vortex/antivortex pairs are clearly seen. The “divergence map” for this eigenmode is practically zero everywhere, as there is no compressional part (Fig. 4.3(a)). This is not the case for the eigenmodes (c) and (d) of Fig. 4.1. Fig. 4.3(c) and (e) show the “divergence maps” for both eigenmodes, in which the compression and rarefaction can be clearly seen. Both cases show no shear part (Fig. 4.3(d) and (f)). Fig. 4.3(c) and 4.3(e) (see also the 3D plots at the bottom of Fig. 4.3) exhibit clearly dipole type of compressional oscillations between (Fig. 4.3(c)) and at (Fig. 4.3(e)) the defect regions.

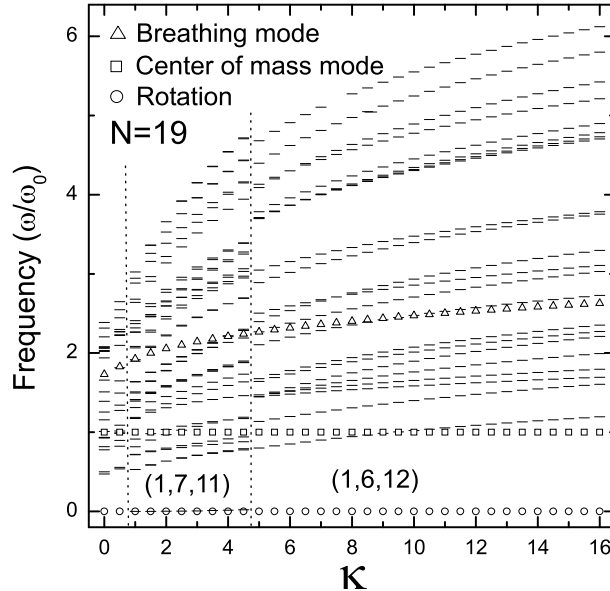


Fig. 4.4 The eigenfrequencies for the  $N = 19$  cluster as a function of  $\kappa$ . The frequencies of the rotation, center of mass mode and breathing mode are shown by the different symbols.

## 4.2 NORMAL MODES IN A YUKAWA SYSTEM

In this section, we discuss the excitation spectrum corresponding to the ground state configuration of the Yukawa system. As we presented, in the pure Coulomb interaction system, it is well known that there are three eigenfrequencies which are independent of  $N$  [55]:  $\omega/\omega_0 = 0, 1$  and  $\sqrt{3}$ , which correspond to the rotation of the system as a whole, the center of mass mode and the breathing mode, respectively. In the Yukawa system, the modes with frequency  $\omega = 0$  and  $\omega/\omega_0 = 1$  do not depend on the interaction between the particles [117]. But the frequency of the breathing mode depends on the screening parameter  $\kappa$  and the number of particles.

In Fig. 4.4 we show the eigenfrequencies for the  $N = 19$  particles as a function of  $\kappa$  where the three previous eigenmodes are indicated by different symbols. The eigenfrequencies of a uniform rotation and the center of mass mode are independent of the value of  $\kappa$ . The eigenfrequency of the breathing mode increases with increasing  $\kappa$ . This agrees with previous theoretical work [136] and recent experimental results [47]. Note also that the spectrum exhibits a discontinuous behavior of the value of the eigenmodes as function of  $\kappa$  at  $\kappa = 0.66$  and  $4.58$  where the ground-state configuration changes between the  $(1,6,12)$  and  $(1,7,11)$  configuration.

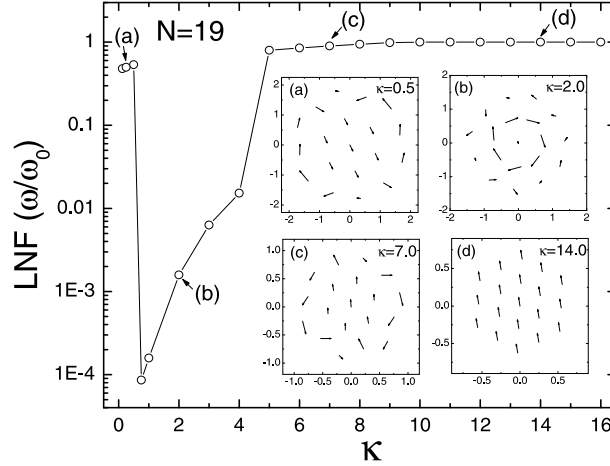


Fig. 4.5 The LNF as a function of  $\kappa$  for  $N = 19$  particles. The inset shows vector plots of the eigenvectors for four different values of  $\kappa$ .

The lowest non-zero normal mode frequency (LNF) is a measure for the stability of the ground state. It tells us how easy (or difficult) it is to deform this state. In general, the LNF will increase when increasing the value of  $\kappa$  for the same configuration, since the radius of the system decreases with increasing  $\kappa$ , and the system becomes stiffer [136]. Notice that the LNF changes sharply when the configuration changes. For example, the LNF as a function of  $\kappa$  for  $N = 19$  particles is shown in Fig. 4.5. When  $\kappa < 0.66$ , the LNF increases with increasing  $\kappa$ . Its groundstate configuration is (1,6,12) and the lowest non-zero frequency eigenmode (see inset (a) of Fig. 4.5) corresponds to a vortex-antivortex excitation [55]. At the critical value  $\kappa = 0.66$ , the LNF suddenly drops almost to zero. When  $0.66 < \kappa < 4.58$  the (1,7,11) is the ground-state configuration and the LNF slightly increases with increasing  $\kappa$ . The LNF excitation now corresponds to an intershell oscillation of the two rings (see inset (b) of Fig. 4.5). Further increasing the value of  $\kappa > 4.58$ , the ground-state configuration changes back to (1,6,12) and the LNF mode is again the vortex-antivortex excitation (see inset (c) of Fig. 4.5). When  $\kappa > 10.0$ , further increasing the value of  $\kappa$  does not change the LNF because it equals  $\omega/\omega_0 = 1$  which is the center of mass vibrational mode (see inset (d) of Fig. 4.5). The (1,6,12) configuration is a so-called “magic number” [55] configuration which is more stable against deformations than the (1,7,11) configuration. In the former the position of the particles on the two rings are commensurable which makes their positions strongly inter-locked, which is not the case for the (1,7,11) configuration.

Note that it was previously found [55] that for small Coulomb systems, the lowest frequency mode (LFM) corresponds to intershell rotation, whereas for larger number of particles it corresponds to the excitation of a vortex-

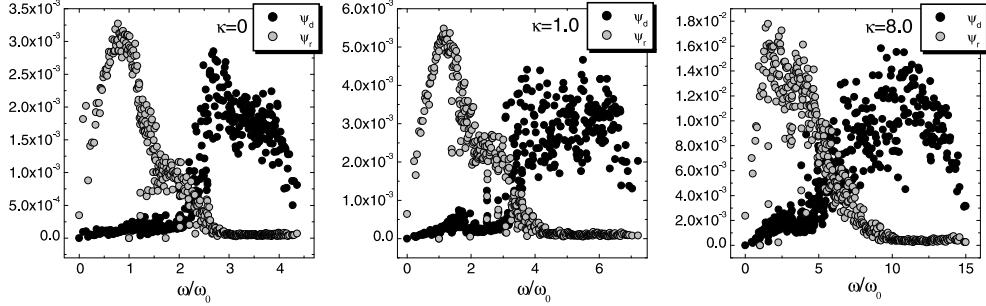


Fig. 4.6 Distribution of the rotor  $\psi_r$  and the divergence  $\psi_d$  as a function of the frequency for  $N = 200$  particles for different values of  $\kappa$ .

antivortex pair [55]. This is not always so for the Yukawa system as we just found. For a fixed value of  $N$  and depending on the value of  $\kappa$  inter-shell as well as vortex-antivortex pair excitations, and even the center of mass mode can be the LNF eigenmode.

The modes can have a shear-like or a compression-like character. The compressional and shear properties can be extracted from the divergence and rotor of the velocity field. Recently, we calculated the spatially resolved divergence and rotor of the different modes [138] for a Coulomb interacting 2D cluster. In this section, we will associate a single number for the shear-like and compression-like character of the different modes by calculating the spatial average of the divergence  $\vec{\nabla} \cdot \vec{v}$  and the vorticity  $(\vec{\nabla} \times \vec{v})_z$  of the velocity field, following the approach of Ref. [55].

The  $z$  component of the rotor  $\psi_r(k) = \vec{e}_z \cdot \text{rot}\psi(k)$  and the divergence  $\psi_d(k) = \text{div}\psi(k)$  of the field of eigenvectors of mode  $k$  are

$$\psi_d(k) = \frac{1}{N} \sum_{i=1}^N \psi_{d,i}^2(k), \quad (4.1)$$

$$\psi_r(k) = \frac{1}{N} \sum_{i=1}^N \psi_{r,i}^2(k), \quad (4.2)$$

where the values of  $\psi_{d,i}(k)$ , and  $\psi_{r,i}(k)$  for the  $i$ th particle are given by

$$\psi_{d,i}(k) = \frac{1}{M} \sum_{m=1}^M (\vec{r}_i - \vec{r}_m) \cdot [\vec{A}_i(k) - \vec{A}_m(k)] / |\vec{r}_i - \vec{r}_m|^2, \quad (4.3)$$

$$\psi_{r,i}(k) = \frac{1}{M} \sum_{m=1}^M |(\vec{r}_i - \vec{r}_m) \times [\vec{A}_i(k) - \vec{A}_m(k)]| / |\vec{r}_i - \vec{r}_m|^2, \quad (4.4)$$

Here,  $m$  and  $M$  denote the index and number of neighboring particles of particle  $i$ ,  $\vec{r}_m$  is the positional coordinate of a neighboring particle and  $\vec{A}_i(k)$  is the eigenvector of particle  $i$  for mode  $k$ . Note that in contrast to Ref. [55] where only the nearest-neighbour particle was used instead of the sum in Eqs. (4.3,4.4), we sum over all the neighbours as was recently also done in Ref. [48]. This turns out to be the correct approach because the position and direction of the nearest-neighbour is strongly influenced by small variations of the local environment of particle  $i$ . Note also that we calculate the squared average over all the particles because the simple spatial average is of course zero.

For small Yukawa clusters (i.e.  $N < 40$ ), the properties of the rotor and divergence were discussed in [48]. Here we extend those results to large clusters. In Fig. 4.5 we plot  $\psi_d(k)$  and  $\psi_r(k)$  as a function of the excitation frequency for  $N = 200$  particles for different values of  $\kappa$ . In general, the lower eigenfrequency spectrum corresponds to rotational-type of excitations which are vortex-antivortex like motions of the particles which lead to practically no density fluctuations. Note that  $\psi_r(k)$  exhibits a peak with a shoulder at intermediate frequencies. The shoulder and peak merge into a broad peak in the limit of large  $\kappa$ . In the second half of the spectrum the divergence  $\psi_d(k)$ , which corresponds to compression-like motion, is appreciably different from zero. Notice that for relatively small  $\kappa$  values there is a clear separation between the shear and the compressional modes. However, for large values of  $\kappa$ , the divergence increases more monotonously with frequency before it reaches a maximum. For smaller  $N$  the separation between rotational and compressional modes is less strict and there is a large range of intermediate frequencies where eigenmodes are partly compressional and partly rotational [48].

### 4.3 NORMAL MODES IN A HARD WALL CONFINEMENT

In this section, we discuss the excitation spectrum of the ground-state configuration of the Coulomb system with a hard wall confinement, and the corresponding divergence and rotor of it, which describe the ‘shear-like’ and ‘compression-like’ nature of the modes, are investigated.

In a hard wall confinement, a special situation arises for the outer-shell particles as they can only move along the perimeter and radial outward movement of the outer-shell particles is forbidden. Therefore it is convenient to diagonalise the dynamical matrix expressed in polar coordinates. The oscillations of the particles around their equilibrium positions have a component along the  $\rho$  direction and one along the  $\theta$  direction. In the hard wall limit, the particles in the outer shell can have only one component, namely along the  $\theta$  direction, and we neglect the eigenmodes along the  $\rho$  direction, since the corresponding eigenfrequencies are infinite.

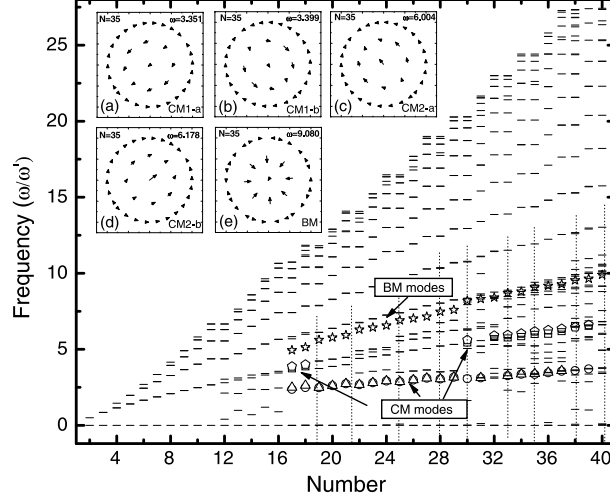


Fig. 4.7 Excitation spectrum of normal modes as a function of the number of particles for  $N = 2 - 40$  for the hard wall confinement. The CM-like and breathing-like modes are marked by symbols. The insets show the four CM-like modes and the breathing-like mode for  $N = 35$ .

The model system and the numerical approach are described in the second chapter.

Next we show our numerical calculation of results for the 2D cluster in the hard wall confinement. Notice that the number of particles at the edge is a considerable part of the whole system. There are  $2N$  normal modes for a  $N$  particle system. In the hard wall case, the radial motion of particles at the edge have a large energy and consequently the number of relevant modes of the hard wall system is  $2N - N_E$ , with  $N_E$  the total number of particles at the edge.

We plot the excitation spectrum of the normal modes as a function of the number of particles for a hard wall confinement and Coulomb inter-particle interaction in Fig. 4.7. For the parabolic confined system, there are three eigenfrequencies, which are independent of  $N$  [55]:  $\omega = 0, \sqrt{2}$  and  $\sqrt{6}$ , which correspond to the rotation of the system as a whole, the center-of-mass mode (CM) and the breathing mode (BM), respectively. In the hard wall case only the  $\omega = 0$  frequency is still present. For  $N = 2 - 11$ , the particles are all situated at the edge, and there is no sense of discussing the CM or BM frequency for hard wall confinement. Starting from  $N > 16$ , more than one particle is situated in the central region.

It is then possible to assign approximately those two eigenmodes (i.e. the CM and BM mode) to some of the eigenmodes of the particles in the central region. Examples of the CM-like and breathing-like modes for  $N = 35$  are shown in the insets of Fig. 4.7, and Fig. 4.9(g) and (h) show the correspond-

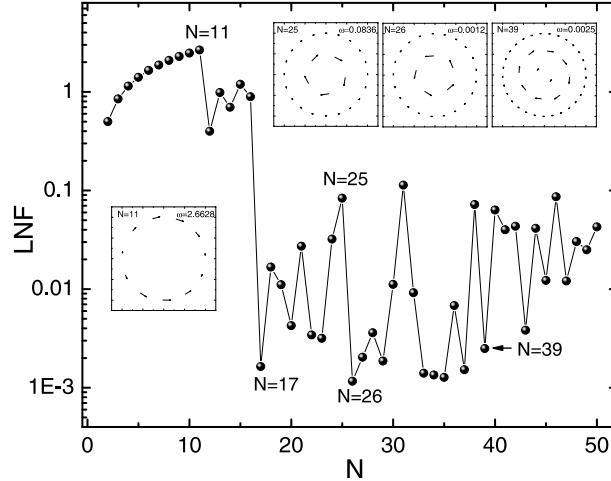


Fig. 4.8 The lowest non-zero eigenfrequency for  $N = 2, \dots, 50$ . The insets show the corresponding eigenmodes for  $N = 11, 25, 26$  and  $39$ .

ing CM-like and breathing-like modes for the central particles for  $N = 100$ , respectively. While for the parabolic case, the amplitudes for all particles are equal, now the particles, which are closest to the center, have the largest amplitudes. The frequencies corresponding with these CM-like and breathing-like modes of the central particles are marked in Fig. 4.7 by symbols. Note that the degeneracy of the CM-like modes is slightly lifted and that for some clusters it is possible to find four CM-like modes. Comparing Fig. 4.7(b) with Fig. 4.7(c) one can see that in these cases the direction of the motion of the outer particles with respect to the direction of the motion of the central particles is different.

It was previously found that for small Coulomb systems, the lowest non-zero frequency mode (LNF) corresponds to intershell rotation, whereas for larger number of particles it corresponds to the excitation of a vortex-antivortex pair [55]. This is not the case anymore for the hard wall system. Fig. 4.8 shows the LNF up to  $N = 50$  particles. When there is more than one particle at the center, the LNF mode corresponds always, also for large systems, with the rotation of all central particles as a whole in the direction opposite to the one for the particles at the edge (see insets of Fig. 4.8 for  $N = 25, 26$  and  $39$  and Fig. 4.9(b) for  $N = 100$ ). For  $N < 12$  all particles are at the edge and the LNF modes are similar to the one shown for  $N = 11$  in the inset of Fig. 4.8, namely the two halves of the wide ring move in opposite direction. The reason why the LNF for  $N = 25$  (configuration (5, 20)) and  $N = 26$  (configuration (5, 21)) differ by two orders of magnitude is similar as for the parabolic confinement system [55]: for  $N = 25$  the number of particles in the outer shell is a multiple of the number of particles in the inner shell,

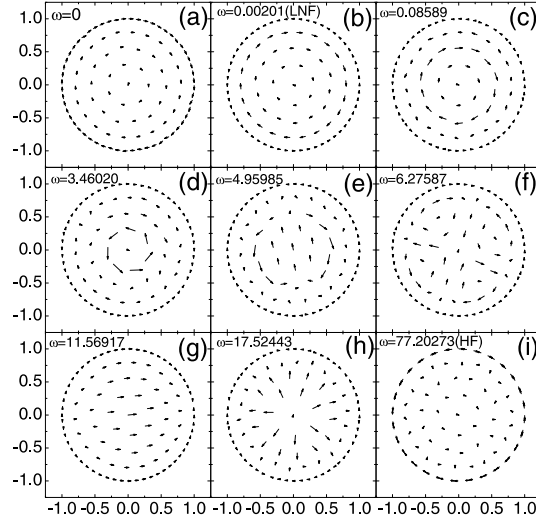
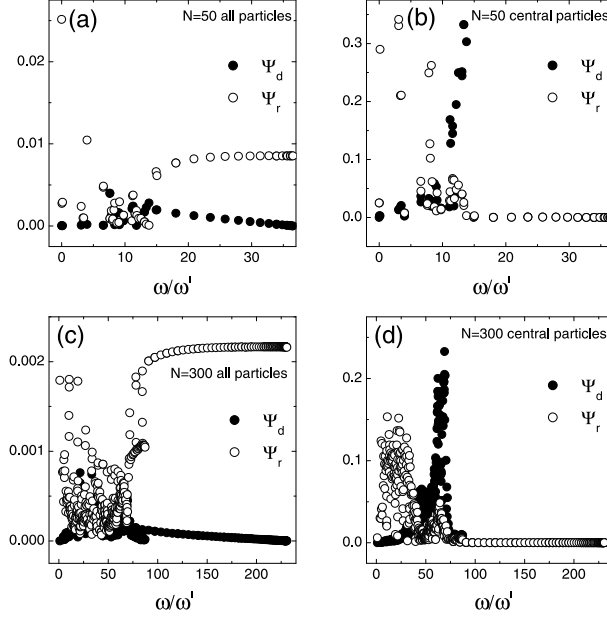


Fig. 4.9 Some eigenvectors for the cluster with  $N = 100$  particles in a hard wall confinement.

resulting in a more stable configuration against intershell rotation (i.e. due to a commensurability effect), and  $N = 25$  corresponds to a magic number clusters. Most of the other peaks in Fig. 4.8 can be explained in a similar way.

As in the system with  $N = 100$  particles in a hard wall confinement, most particles are situated at the edge, and therefore it may be wrong to consider it already as a large system. Therefore we also looked at the LNF of a larger system, namely for  $N = 300$ . Still the LNF corresponds with the rotation of the central particles as a whole and the vortex/antivortex motion appears only for higher frequencies.

It is also interesting to have a look at the higher excited modes as they are much more easy to interpret than in the parabolic case. Fig. 4.9 shows nine modes for  $N = 100$ . With increasing frequency, after the rotation of the cluster as a whole (Fig. 4.9(a)) and the rotation of the central particles as a whole (Fig. 4.9(b)), particles with larger amplitudes appear close to the center of the system, resulting in many different types of intershell rotations (Fig. 4.9(c) and (d)). Higher excitations may consist of a vortex/antivortex pair, or multiples of such pairs (Fig. 4.9(e) and (f)). The highest frequency (HF) mode for parabolic confinement was discussed in Refs. [48, 138]. In these modes the inner particles have larger amplitudes than the outer particles. We found the opposite behavior in the hard wall case. In Fig. 4.9(i), one can see the largest amplitude for the particles at the edge where the nearest particles at the edge move in opposite direction which is typical for the case of an optical mode.



*Fig. 4.10* The  $\psi_d(k)$  and  $\psi_r(k)$  as a function of the excitation frequency for  $N = 50$  (a,b) and 300 (c,d) particles. In Figs. (a) and (c) all particles were included when calculating  $\psi_d(k)$  and  $\psi_r(k)$ , while in Figs. (b) and (d) only the central particles were taken into account in the summation.

In previous results for a 2D classical infinite system [67], two types of waves, with dispersion relations  $\omega \approx k$  (lateral sound waves) and  $\omega \approx \sqrt{k}$  (longitudinal plasma waves) were observed. These waves are related to the compression-like and shear-like modes observed in finite confined cluster. Here we associate a single number to the shear-like and compression-like character of the different modes by calculating the spatial average of the square of the divergence  $\vec{\nabla} \cdot \vec{v}$  and the vorticity  $(\vec{\nabla} \times \vec{v})_z$  of the velocity field, following the approach of Ref. [48, 55].

We calculate the spatial average of the divergence  $\vec{\nabla} \cdot \vec{v}$  and the rotor  $(\vec{\nabla} \times \vec{v})_z$  for the compressional and shear properties of different modes. We will show two kinds of results in which we make the summation in Eqs. (4.1) and (4.2) (i) over all particles and (ii) only over the central particles. So we can clearly see which particles contribute to the compression- and shear-like character of the motion. In the latter case, if we sum in Eqs (4.1) and (4.2) only over the central particles, we sum over all the neighbors in Eqs. (4.3) and (4.4), in contrast to Ref. [55] where only the nearest-neighbour particle was used. This turns out to be the correct approach to get information about the compressional and shear-like properties of the modes of the central particles because the position and direction of the nearest neighbor is strongly

influenced by small variations of the local environment of particle  $i$ . However, we noticed that if we also include the outer particles, it is important to sum in Eqs. (4.3) and (4.4) over all particles. Summation over only the neighbors results in a large divergence for the motion of the particles at the edge, which is not the correct result because the motion of these particles is always tangent to the hard wall.

In Fig. 4.10 we plot  $\psi_d(k)$  and  $\psi_r(k)$  as a function of the excitation frequency for  $N = 50$  and  $300$  particles (for the hard wall system with Coulomb interparticle potential). Similar results were obtained for a dipole interaction. The first column shows results when we sum over all particles, the second column is when we include only the central ones. The large values for  $\psi_r(k)$  for all high frequencies in the first column figures indicate the shear-like character of the motion of the outer particles. The figures in the second column show that both  $\psi_d(k)$  and  $\psi_r(k)$  are almost zero in the high excitation frequency region. This results from the fact that we look only at the motion of the central particles and at high frequencies only the outer particles move. In the parabolic case, the lower eigenfrequency spectrum corresponds to rotational-type of excitations, which are intershell rotation or vortex-antivortex like motions of the particles which lead to practically no density fluctuations. The divergence  $\psi_d(k)$  corresponds to compression-like motion, and in the spectrum  $\psi_d(k)$  can have a maximum at higher frequencies. In the hard wall confinement case, one can see that for small systems with e.g.  $N = 50$  as well as for the large system with  $N = 300$  that  $\psi_d(k)$  and  $\psi_r(k)$  have rather different values in different frequency regions and furthermore two clear separate maxima appear at the lower half of excitation spectrum. In the parabolic case, this clear separation was only present for large systems.

#### 4.4 THE EIGENFREQUENCIES OF TWO PARTICLES

Here we present an illustration of the analytical results of the two particles problem for a general  $r^n$  confinement potential.

The dimensionless expression for the potential energy is already shown in Eq. (2.18). If we choose the  $x$ -axis through both particles, the ground-state configuration is given by

$$x_1 = \left( \frac{n'}{n * 2^{n'+1}} \right)^{1/(n+n')}, \quad x_2 = -x_1, \quad y_1 = y_2 = 0. \quad (4.5)$$

For  $n \rightarrow \infty$  we find  $x_1 = 1$ . The eigenfrequencies are obtained by diagonalising the dynamical matrix, resulting in

$$\omega_1^2 = 0 \quad (4.6)$$

$$\omega_2^2 = n \left( \frac{n'}{n * 2^{n'+1}} \right)^{\frac{n-2}{n+n'}} \rightarrow \frac{n'}{2^{n'+1}} \quad (4.7)$$

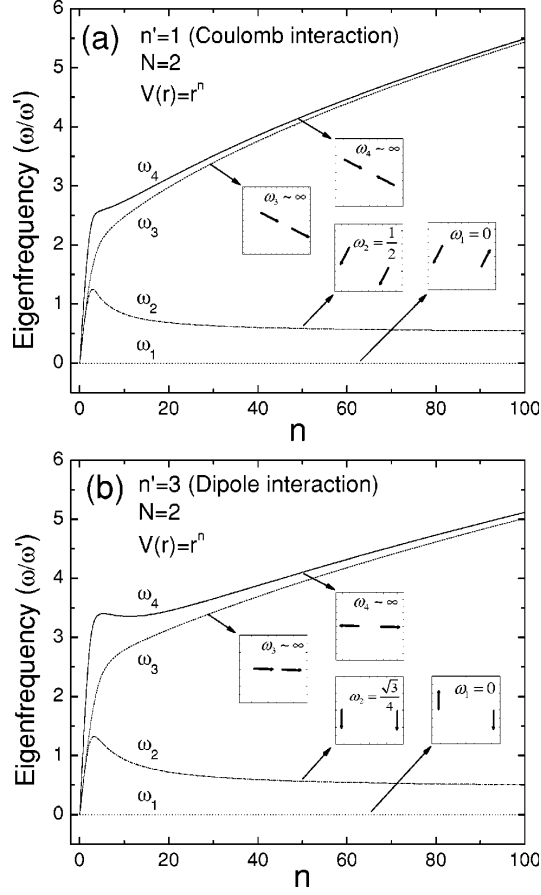


Fig. 4.11 The eigenfrequencies for two particles interacting through a  $r^n$  confinement potential for (a) a Coulomb interparticle potential and (b) a dipole interaction potential. The insets show the motion of the particles and the given frequencies are for  $n \rightarrow \infty$ .

$$\omega_3^2 = n(n-1) \left( \frac{n'}{n * 2^{n'+1}} \right)^{\frac{n-2}{n+n'}} \rightarrow n \frac{n'}{2^{n'+1}} \quad (4.8)$$

$$\omega_4^2 = \frac{nn' + n'^2}{2^{n'+1} \left( \frac{n'}{n * 2^{n'+1}} \right)^{\frac{n'+2}{n+n'}}} \rightarrow n \frac{n'}{2^{n'+1}}, \quad (4.9)$$

where “ $\rightarrow$ ” means the  $n \rightarrow \infty$  (i.e. hard wall) limit. Notice that in the latter limit  $\omega_3 = \omega_4$  diverge. The four eigenmode frequencies for Coulomb and dipole interparticle interaction are illustrated in Fig. 4.11(a) and 4.11(b).

#### 4.5 PERIODIC MOTION OF PARTICLE AT THE EDGE

Since the particles at the edge are practically frozen at the wall, they can only move along the perimeter. A detailed analysis of the radial motion of the particles situated at the edge of the hard wall is given in the following.

We start with the total Hamiltonian with the same potential energy term as used in our calculations, namely  $N$  particles interacting through a  $1/r^{n'}$  potential and confined in the plane by the hard wall potential. In the expansion of the Hamiltonian till lowest order in the small displacements of the particles around the equilibrium ground-state positions the coordinates of the various particles are separable. Therefore it is justified to consider only the motion of a single particle. For a particle at the edge the contribution to the expanded Hamiltonian is of first order for a small displacement in the radial direction, and of second order for a small angular displacement. Therefore, we look only at the radial motion. Let us assume that the ground-state coordinates of particle 1 are given by  $(-R, 0)$  and we introduce a small perturbation in the radial direction for the first particle  $x = -R + \Delta x$ . To the lowest approximation the Hamiltonian becomes

$$\begin{aligned}
 H = & m \frac{(\Delta \dot{x})^2}{2} - n' \frac{e^2}{\varepsilon} \sum_{i=2}^N \frac{\Delta x (-R - x_i)}{[(-R - x_i)^2 + y_i^2]^{(n'+2)/2}} \\
 & + \frac{e^2}{\varepsilon} \sum_{i=1}^{N-1} \sum_{j=i+1}^N \frac{1}{[(x_i - x_j)^2 + (y_i - y_j)^2]^{n'/2}}. \quad (4.10)
 \end{aligned}$$

The equation of motion for the small displacement  $\Delta x$  of the first particle is easily shown to be

$$\Delta \ddot{x} = n' \frac{e^2}{\varepsilon} \sum_{i=2}^N \frac{(-R - x_i)}{[(-R - x_i)^2 + y_i^2]^{3/2}} = C, \quad (4.11)$$

with solution

$$\Delta x = \frac{C}{2} t^2 + v_0 t. \quad (4.12)$$

This expression reminds us of the motion of a bouncing ball in the field of gravity. Its trajectory in time consists of equal pieces of interconnected parabolas. The motion starts at  $t = 0$  at the hard wall. The particle moves in the positive direction and reaches its maximal distance from the wall at  $\Delta x_{\max} = -v_0^2/(2C)$  after  $t_{\max} = -v_0/C$ . Then the particle moves back and at  $t = 2t_{\max}$  it reaches again the wall at  $\Delta x = 0$ . Now the particle is reflected elastically by the wall, it changes its momentum from  $v_0$  to  $-v_0$ , and repeats its periodical motion. The period of this motion is given by

$$T = 2t_{\max} = 2\sqrt{-2\Delta x_{\max}/C}, \quad (4.13)$$

which corresponds to a frequency

$$\omega = \frac{2\pi}{T} = \frac{\pi}{\sqrt{-2\Delta x_{\max}/C}}. \quad (4.14)$$

Consequently, we have a periodic motion whose frequency depends on the amplitude of the oscillatory motion like in the case of an anharmonic oscillator. But the difference is that there is no linear regime, which is the reason that such a motion was not considered in the following chapter of the eigenmodes in a hard wall confinement. Notice that the frequency grows to infinity when the amplitude of the excitation goes to zero.

Thus in conclusion, due to the hard wall confinement potential, the particles at the edge can't perform a harmonic motion in the radial direction. But nevertheless, these particles can perform a periodic bouncing motion against the wall which is purely anharmonic in character.

## 4.6 CONCLUSIONS

The spectral properties of two-dimensional clusters of charged classical particles in a parabolic and hard wall potential were investigated through the Monte Carlo simulation technique.

In particular the lowest non zero eigenfrequency which is a measure for the stability of the cluster was investigated. In the parabolic confinement, the shear and compression content of the modes was calculated and it was found that for large  $N$  the lower half of the eigenfrequency spectrum are mostly "shear-like" modes, while the upper half of the spectrum contain the "compression-like" modes. In a complex plasma, the frequency of the eigenmodes were investigated as function of  $\kappa$ .

In the hard wall confinement, center of mass and breathing modes can be indentified approximately for the central particles, while the lowest non-zero frequency corresponds with a rotation of the central particles as a whole (in the opposite direction to the particles at the edge). Larger frequencies correspond with many different types of intershell rotations, followed by vortex/anti-vortex excitations. The highest frequencies involve large amplitudes for angular movement of particles at the edge, as they are almost frozen in the radial direction.

Also the shear- and compression-like character of the modes was investigated. A clear distinction can be made between low-frequency shear-like modes and high-frequency compression-like modes. The highest frequency modes are again shear-like modes, corresponding with the motion of the particles at the edge.

**Publications.** The results presented in this chapter were published as:

- Minghui Kong, B. Partoens and F. M. Peeters, *Topological defects and Non-homogeneous melting of large 2D Coulomb Clusters*, Phys. Rev. E **67**, 021608 (2003) (8 pages).
- Minghui Kong, B. Partoens, and F. M. Peeters, *Structural, dynamical and melting properties of two-dimensional Clusters of Complex Plasmas*, New Journal of Physics **5**, 23 (2003) (17 pages).
- F. M. Peeters, B. Partoens and Minghui Kong, *The classical electron gas in artificial structures*, in the proceedings of the International School of Physics “Enrico Fermi” (Varenna, Italy, 2003) (20 pages).
- Minghui Kong, B. Partoens, A. Matulis and F. M. Peeters, *Structure and spectrum of two-dimensional clusters confined in a hard wall potential*, Phys. Rev. E **69**, 036412 (2004) (10 pages).



# 5

---

## *Melting of 2D clusters*

### 5.1 INTRODUCTION

There has been considerable progress in the study of melting in classical finite clusters. The melting properties of this system have been studied experimentally [6, 143] and by the Monte Carlo(MC) [121], the path integral Monte Carlo approach [144], and molecular dynamics [81, 135] simulations. In a hard wall confined system with short-range inter-particle interaction, the melting behavior was found to be even more interesting. Reentrant melting of 2D colloidal clusters in a hard wall potential was obtained in both experimental [6] and theoretical work [81].

For the finite classical system confined in a parabolic trap, the clusters consist of well-separated shells [55, 70, 106, 128], and the melting scenario of a laterally confined 2D system was found earlier to be a two step process, upon increasing the temperature: First intershell rotation becomes possible where orientational order between adjacent shells is lost while retaining their internal order. At even higher temperatures, the growth of thermal fluctuations leads to radial diffusion between the shells, which finally destroys the positional order. The temperature of radial melting  $T_r$  may be many orders of magnitude higher than the orientational melting temperature  $T_o$  [55]. Large clusters with  $N > 100$  have a regular triangular lattice structure and exhibit only radial melting [70].

In the quantum regime, Wigner crystallization of electrons in 2D quantum dots exists and it is accompanied by two distinct-radial and orientational-ordering transitions too [144]. It proceeds in two stages: (i) via radial or-

dering of electrons on shells and (ii) freezing of the intershell rotation. This melting scenario which is caused by quantum fluctuations exists even at zero temperature.

In the present chapter, we first report the melting process in a large system in which the particles interact with a pure Coulomb interaction. In the subsequent section, the melting properties of a complex plasma are given which shows a complicated scenario because of the different inter-particle interaction potential. At the end, we summarize our results.

## 5.2 NON-HOMOGENEOUS MELTING IN A COULOMB SYSTEM

In this section we apply the MC method and relate the melting to the dynamical properties to investigate how the ordered state is lost with increasing temperature. Previously several groups used the molecular dynamics [137, 145] simulation technique to investigate melting of a finite 2D system.

In the present work we consider a finite 2D system where we take  $N = 291$  for our numerical simulation. Here we present a calculation of the melting phase diagram by performing MC simulations. In Ref. [135] molecular dynamics was used to investigate the melting of a cluster of particles interacting through a logarithmic interaction. As compared to our Coulomb interaction where the geometry induced defects are situated in the third and fourth outer shells (i.e., the transition region) and around the six corners of the “defect” hexagon, in the logarithmic interacting system [135] those defect are mainly situated in the outer two shells. In Ref. [135], the number and type of defects were studied as function of the noise (i.e. temperature). Here we will use several different criteria such as the total energy, the radial dependent mean square displacement, the bond-angular order factor and the angular square deviation to characterize the melting behavior of the cluster.

There are several different criteria that can be used to find the melting temperature. In order to determine the melting transition point, we calculated the potential energy of the system as a function of temperature (see Fig. 5.1). In the crystalline state the potential energy of the system increases almost linearly with temperature and then after the critical temperature is reached ( $T/T_0 = 0.01$  for  $N = 291$ ), it increases more steeply as shown in Fig. 5.1. This is a signature of melting and is related to the unbinding of dislocation pairs. The dotted assurgent line in Fig. 5.1 indicates the linear temperature dependence of the potential energy for low temperatures before melting. In the upper inset Fig. 5.1(a), we plot  $\Delta E$  which is the difference between the numerical obtained energy and the linear T-behavior. After the melting point,  $\Delta E$  increases sup-linear.

The lower inset, Fig. 5.1(b), shows the averaged number of defects as function of temperature  $T/T_0$ . The number of defects were obtained as follows. We considered 40 configurations for every temperature  $T/T_0$ . Every 500 MC

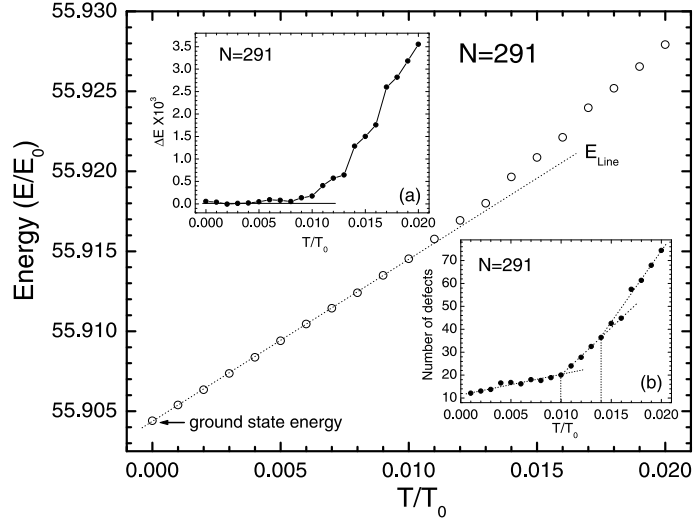


Fig. 5.1 The potential energy ( $E/E_0$ ) of the 2D Coulomb cluster as a function of temperature  $T/T_0$  for  $N = 291$ . The insets show  $\Delta E = E - E_{line}$  (a) and the number of defects (b) as a function of temperature  $T/T_0$ .

steps a new configuration was obtained. For all these configurations the number of defects were counted. Finally we averaged over the 40 configurations, which is the reason why the number of defects can be non-integer. With increasing temperature, the system generates more and more defects and after the melting point the defect number grows very fast. Notice that two clear critical temperatures emerge from this figure at the crossing points of the dotted lines, i.e.  $T/T_0 = 0.01$  and  $T/T_0 = 0.014$ .

Fig. 5.2 shows typical particle trajectories for two temperatures which show that the melting of this system is very complex and non-homogeneous. It clearly indicates that the melting starts around the six corners of the hexagon which are exactly the defect regions. With increasing temperature, the particles in the defect region start to move radially and destroy order locally. With further increase of temperature the total system completely melts and the order is destroyed.

In order to better describe the spatial dependence of the melting process in a large system, we separate the configuration into three regions as shown in the inset of Fig. 5.4. Region I (dark grey colored hexagonal area) is comprised of the defect-free hexagonal center; region II is a transition region with the defects (light grey colored area), and region III consists of the outermost two rings. For the case of  $N = 291$  particles region I consists of 91 particles, region II consists of 116 particles and region III of 84 particles. We calculate for each region the mean square displacement  $\langle u_R^2 \rangle$ , which was also introduced in Eq. (1.2) in the first chapter. Fig. 5.3 shows the  $\langle u_R^2 \rangle$  as a function of the reduced

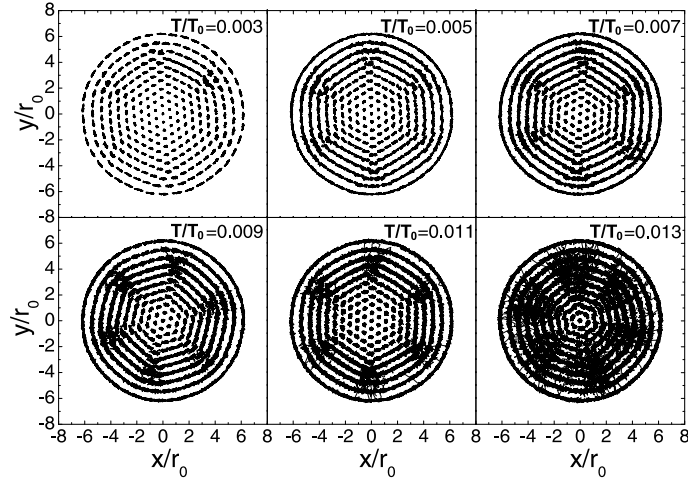


Fig. 5.2 Typical snapshots of particles trajectories for different temperatures  $T/T_0$  for  $N = 291$ .

temperature  $T/T_0$  for the three different regions. At low temperatures the particles exhibit harmonic oscillations around their  $T = 0$  equilibrium position, and the oscillation amplitude increases linearly and slowly with temperature: the particles are well localized and display still an ordered structure. This linear dependence is accentuated by the thin straight lines in Fig. 5.3.

Here, we already notice that the amplitude of the local particle thermal vibrations in these different regions are different. The amplitude is largest at the defect region and lowest in the center of the cluster. Melting occurs when  $\langle u_R^2 \rangle$  increases very sharply with  $T$ . Because of the finite number of particles one has rather a melting region, instead of a well-defined melting temperature. After the melting “point”, the particles exhibit liquid-like behavior. Fig. 5.3 exhibits three different melting temperatures corresponding to the three different regions. Firstly region II, i.e. the transition region containing the defects, starts to melt, then the outermost two rings melt, and finally the hexagonal region melts. Following Ref. [120], we can “define” a melting temperature at the point where  $\langle u_R^2 \rangle \approx 0.10$  which results into the melting temperatures  $T_{melt}/T_0 \simeq 0.0115, 0.0125$  and  $0.0138$  for the defect region, the outer rings and the center region, respectively.

In order to investigate the melting in the defect region in further detail we consider two new small regions as shown in the inset of Fig. 5.4. One region is around the defect, the other doesn’t contain a defect and is situated between two defect regions. For  $N = 291$  each of the two regions contains respectively eight and seven particles. In Fig. 5.4, the  $\langle u_R^2 \rangle$  of these two different regions show a different melting temperature: the melting clearly starts first around the defect as expected. The particle motion is strongly

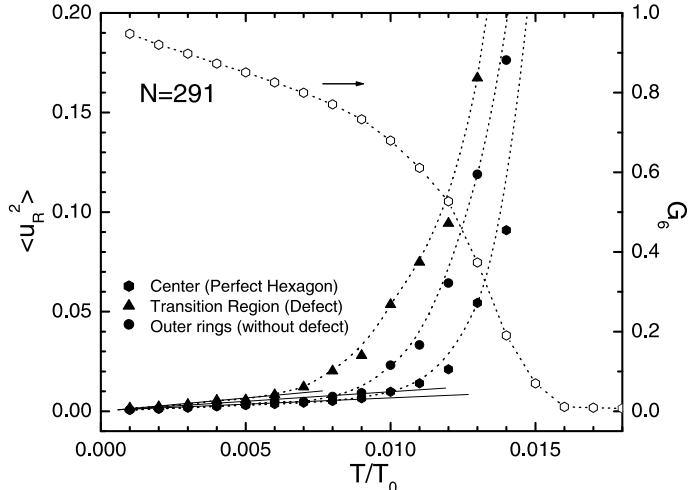


Fig. 5.3 The mean square displacements as a function of the temperature  $T/T_0$  for the three regions defined in the inset of Fig. 5.4 for  $N = 291$  particles. The linear dependence at low temperature is accentuated by the thin straight lines. The open symbols are the results for the correlation function  $G_6$  referred to the right scale, for the inner hexagonal region. The dotted curves are guides to the eye.

influenced by the topological defects, i.e. the particles in the defect regions are less well interlocked and have a larger diffusion constant than the undistorted lattice regions and their thermal motions are easier to be excited [146].

Notice that for the two separate regions a much sharper melting behavior is found than for the intermediate region as a whole (see Fig. 5.3). The reason of course is that in Fig. 5.3 one averages over defect and defect-free regions. The criterion  $\langle u_R^2 \rangle \approx 0.10$  results into  $T_{melt}/T_0 \simeq 0.0118, 0.0138$  for the defect and the defect-free regions, respectively. These two melting temperatures are very similar to the melting temperature of the transition region and the hexagonal region of Fig. 5.3.

The third independent parameter is the bond-orientational correlation function. This quantity determines the type of melting transition and the melting point for an infinite system. Our finite system is too small in order to have a reliable analysis of the asymptotic decay of the density correlation function. Therefore, we calculate the bond-angular order factor which was originally presented in Ref. [147], but following Ref. [121] we modified it into,

$$G_6 = \left\langle \frac{1}{N} \sum_{j=1}^N \frac{1}{N_{nb}} \exp(iN_{nb}\theta_{j,n}) \right\rangle, \quad (5.1)$$

This quantity is calculated only for region I which exhibits a hexagon structure, where  $j$  means the  $N_{nb}$  nearest neighbours of particle  $i$ , for ideal hexag-

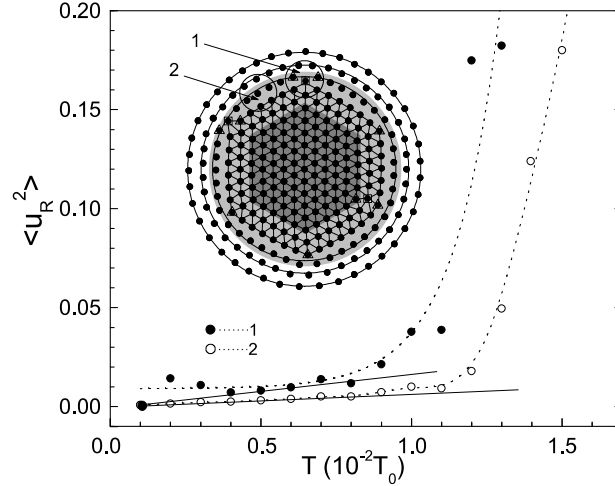


Fig. 5.4 The mean square displacements as function of the temperature  $T/T_0$  for the small defect-free (open symbols) and defect regions (solid symbols) in the intermediate region as indicated by the circular areas in the inset. The thin straight lines show the low temperature linear dependence. The inset figure is the ground state configuration for  $N = 291$ . The dots give the position of the particles. Three regions are found: I (dark grey colored hexagonal area) is comprised of the defect-free hexagonal lattice; II is a transition region with the defects (light grey colored area), and III consists of the outermost two rings. The '+1' and '-1' topological defects are represented by the open squares and triangles, respectively.

onal lattice  $N_{nb} = 6$ , where  $\theta_{j,n}$  is the angle between some fixed axis and the vector which connects the  $j^{th}$  particle and its nearest  $n^{th}$  neighbour.

For a perfect hexagonal system,  $G_6 = 1$ . In our system for  $N = 291$ , the initial value of  $G_6$  is 0.96, which means that the structure in region I is almost perfect hexagonal. Our numerical results (see open dots in Fig. 5.3) show that  $G_6$  decreases linearly with increasing temperature. When  $G_6$  is around 0.6, it more rapidly drops to zero with increasing temperature.  $G_6$  should be zero for the liquid state. This can be compared with the infinite system where a universal melting criterion was found in Ref. [121]: melting occurs when the bond-angle correlation factor becomes  $G_\theta \approx 0.45$ , which was found to be independent of the functional form of the interparticle interaction. For our system the value  $G_\theta \approx 0.45$  is probably not correct because in our finite system  $G_6$  does not drop to zero at  $T_{melt}$ , but is smeared out around  $T_{melt}$ . Therefore, the midpoint  $G_6 \approx 0.45/2 \approx 0.225$  is expected to describe better the melting temperature. This leads to  $T_{melt}/T_0 \approx 0.0136$  which is similar to the result  $T_{melt}/T_0 \approx 0.0138$  obtained from the radial displacement criterion.

In contrast to bulk systems, the melting scenario of small laterally confined 2D systems was found earlier [70] to be a two-step process. Upon increasing the temperature, first intershell rotation becomes possible where orientational

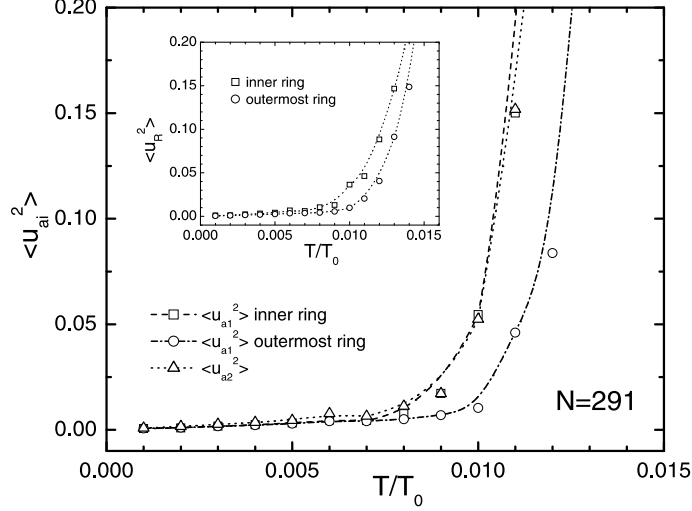


Fig. 5.5 The relative angular intrashell square deviation  $\langle u_{a1}^2 \rangle$  and relative intershell square deviation  $\langle u_{a2}^2 \rangle$  of the outermost two rings as a function of temperature for  $N = 291$ .

order between adjacent shells is lost while retaining their internal order and the shell structure. At even higher temperatures, the growth of thermal fluctuations leads to radial diffusion between the shells, which finally destroys the positional order. To characterize the relative angular intrashell and the relative angular intershell, we use the functions as defined in Ref. [70]. The equations of the relative angular intrashell square deviation  $\langle u_{a1}^2 \rangle$  and the relative angular intershell square deviation  $\langle u_{a2}^2 \rangle$  are given in Eqs. (1.3) and (1.4) in the first chapter, where the number in the outermost two rings  $N_R$  is the same and equals 42 for our  $N = 291$  system. Only the two outermost rings have a clear shell structure. Both two outer rings are strongly interlocked which is a consequence of the 1D Wigner lattice arrangement of the two rings.

From Fig. 5.2, one can see that the inner ring will melt before the outermost ring. In Fig. 5.5, we find that the result for  $\langle u_{a1}^2 \rangle$  of the inner ring is almost the same as  $\langle u_{a2}^2 \rangle$  which is the relative angular intershell square deviation. It means that when the inner ring loses its order, the relative order is lost simultaneously. The outermost ring can still keep its order and it will melt at even higher temperature. Comparing this with Fig. 5.3, we see that the radial and angular displacements start to increase rapidly at approximately the same temperature. Thus for large clusters intershell rotation will not occur below the melting temperature, but appears at the same temperature when the radial displacements increase.

### 5.3 MELTING AND ENERGY BARRIERS IN A YUKAWA SYSTEM

In this section, the phase transitions and energy barriers of a complex plasma are reported. MC simulation is used to study in detail the order-disorder transition (“melting”) of the cluster. In most papers, one concentrates on the study of the minima in the energy landscape while the barriers between those minima are left out of the discussion. Here the saddle point states, which are the critical states in the transition between the ground state and the metastable states, are studied, from which the potential barriers are obtained.

We use the same criteria such as the radial-dependent mean square displacement and the angular-square deviation to characterize the melting behavior of the cluster.

Fig. 5.6 shows  $\langle u_R^2 \rangle$  as a function of the scaled temperature  $T/T_0$  for  $N = 18, 19$ , and  $300$  for different  $\kappa$ . At low temperatures the particles exhibit harmonic oscillations around their  $T = 0$  equilibrium position, and the oscillation amplitude increases linearly but slowly with temperature: the particles are well localized and display still an ordered structure. Melting occurs when  $\langle u_R^2 \rangle$  increases very sharply with  $T$ . Because of the finite number of particles one has rather a region than a well-defined melting temperature. After the melting point, the particles exhibit liquid-like behavior. Following Ref. [120], we can “define” a melting temperature at the point where  $\langle u_R^2 \rangle \approx 0.10$ , which in fact is the Linderman melting criterion.

The melting temperature as defined in this way is depicted in Fig. 5.7. Notice that the ground-state configuration for  $N = 19$  changes from (1,6,12) to (1,7,11) in the same range of  $\kappa$ . This may influence the melting behavior. To avoid this, we calculated the melting properties for a cluster with  $N = 18$  particles (see Fig. 5.6(b)) which has the same structure (only different radius) for all  $\kappa$ . Again we found that the melting temperature decreases with increasing screening parameter  $\kappa$ . Therefore we conclude that the melting temperature of a small Yukawa cluster will decrease with increasing screening parameter  $\kappa$ . However, from Fig. 5.6(c), we see that this conclusion is not valid for a large system, in fact the opposite  $\kappa$  dependence is found as is clearly shown in Fig. 5.7.

In the third chapter, we mention that the system becomes stiffer with increasing  $\kappa$  [136]. Therefore we expected a higher melting temperature with increasing  $\kappa$  which is as just shown, not the case except for large clusters. To understand this unexpected melting behavior, we investigated the energy landscape. It is well known that the number of saddle points increases rapidly with the particle number  $N$  which leads to a very complex energy landscape. Therefore, we considered first the case with six particles. We obtained the barrier height between the ground state and the metastable state. For the six particle system, there are always two saddle point states, one ground state (1,5) and one metastable state (6) for every value of  $\kappa$ . One of these two

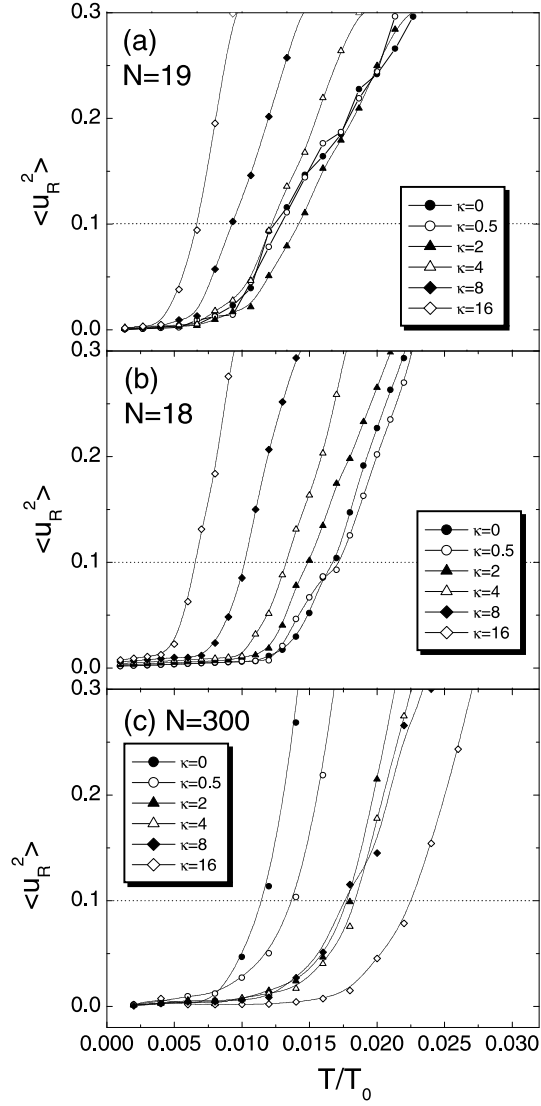


Fig. 5.6 The mean square displacement as function of temperature  $T/T_0$  for  $N = 19$  particles (a), 18 particles (b) and 300 particles (c) for different values of  $\kappa$ .

saddle point states is between the ground state and the metastable state. The other saddle point is between the same metastable state and another one which are simply rotated with respect to each other.

The potential barriers and the melting temperature for  $N = 6$  particles as function of the parameter  $\kappa$  are plotted in Fig. 5.8. One can see that the melting temperature has a maximum in the range  $1 < \kappa < 2$ . Notice that the

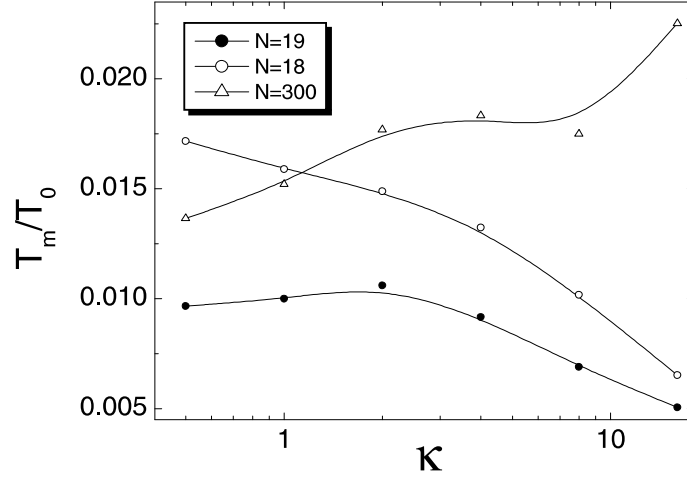


Fig. 5.7 The melting temperature as a function of the screening parameter  $\kappa$  for  $N = 18, 19$  and 300 particles.

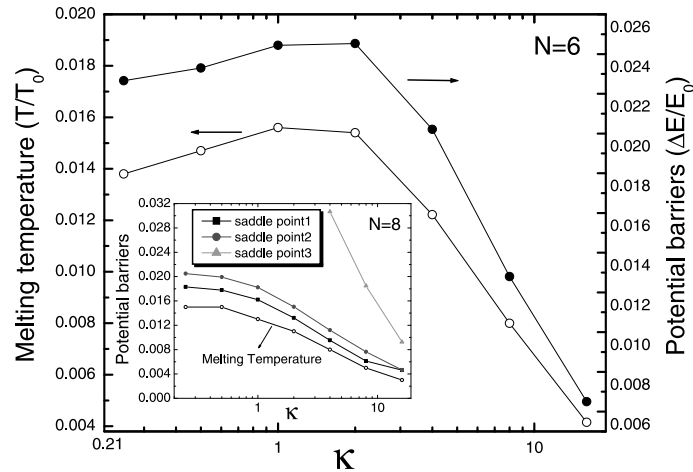


Fig. 5.8 The melting temperature and the potential barriers for  $N = 6$  and 8 particles (inset of figure) as function of the screening parameter  $\kappa$ .

potential barrier between the ground state and the metastable state is closely related to the melting temperature. The melting occurs through thermal excitation of one of the particles which hops from the center of the system to the shell. We made a similar investigation for  $N = 8$  particles which is a more complex system having several saddle points and the results are shown in the inset of Fig. 5.8. Notice that the lowest two potential barriers and the melting temperature have the same  $\kappa$  dependence.

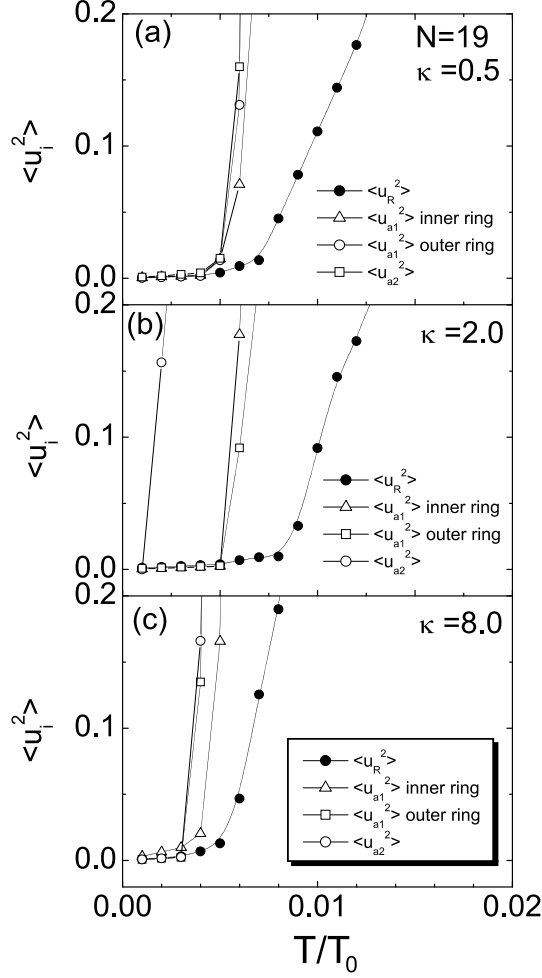


Fig. 5.9 The mean square displacements  $\langle u_R^2 \rangle$ , the relative angular intrashell square deviation  $\langle u_{a1}^2 \rangle$  and relative intershell square deviation  $\langle u_{a2}^2 \rangle$  as a function of temperature  $T/T_0$  for  $N = 19$  and (a)  $\kappa = 0.5$ , (b)  $\kappa = 2.0$ , and (c)  $\kappa = 8.0$ .

To characterize the angular motions of particles, the relative angular intrashell and the relative angular intershell displacement are used again following the functions in Ref. [70]. The relative angular intrashell square deviation  $\langle u_{a1}^2 \rangle$  characterizes the angular motion in a particular shell, while the relative angular intershell square deviation  $\langle u_{a2}^2 \rangle$  shows if the motion of the two adjacent shells is correlated or not.

A clear two-step melting process is also found for the Yukawa system. The radial-dependent mean square displacement and the angular-square deviation for  $N = 19$  particles with different  $\kappa$  are plotted in Fig. 5.9. From Fig. 5.9(a)-

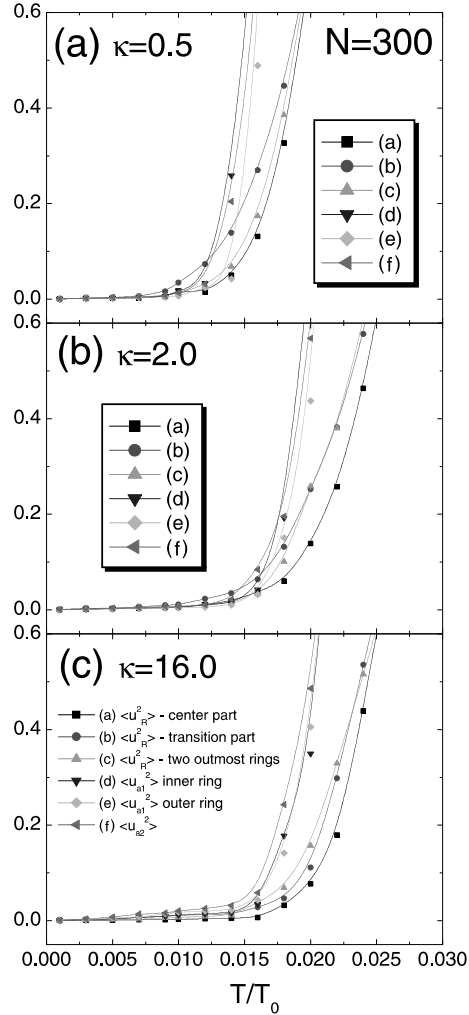


Fig. 5.10 The mean square displacement  $\langle u_R^2 \rangle$  for the three different regions in the cluster, the relative angular intrashell square deviation  $\langle u_{a1}^2 \rangle$  and the relative intershell square deviation  $\langle u_{a2}^2 \rangle$  as a function of temperature  $T/T_0$  for  $N = 300$  and different values of  $\kappa$ : (a)  $\kappa = 0.5$ , (b)  $\kappa = 2.0$  and (c)  $\kappa = 16.0$ .

(c), one can see that the radial melting always appears at higher temperature than the angular melting. In Fig. 5.9(a), the  $\langle u_{a1}^2 \rangle$  of the inner ring and the outer ring are almost the same as  $\langle u_{a2}^2 \rangle$  which is the relative angular intershell square deviation. This means that when the inner ring loses its order, the relative order is lost simultaneously, and the outer ring has almost the same melting temperature as the inner ring. For  $\kappa = 2.0$  (see Fig. 5.9(b)), the  $\langle u_{a2}^2 \rangle$  displacement starts for much lower temperature than the  $\langle u_{a1}^2 \rangle$ .

It should be noted that when  $\kappa = 2.0$ , the ground-state configuration for  $N = 19$  is (1,7,11), which is more unstable against intershell rotation than the configuration (1,6,12). Therefore, the relative intershell order disappears for very low temperature, and the two-shell structure still exist and they melt at higher temperature. The radial melting will start at even higher temperature. Fig. 5.9(c) is quite similar to Fig. 5.9(a), due to the same structure of the ground-state configuration. Using the definition  $\langle u_i^2 \rangle = 0.1$  as the melting criterion we found for the loss of angular intershell correlations the melting temperature  $T_{a2}/T_0 = 0.0042, 0.0012, 0.0033$ , and for the loss of intrashell correlation  $T_{a1}/T_0 = 0.0061, 0.0055, 0.0045$  and for the radial melting  $T_R/T_0 = 0.0097, 0.011, 0.0067$  for  $\kappa = 0.5, 2.0$ , and  $8.0$ , respectively.

In order to better describe the spatial dependence of the melting process in large clusters, we separate the large system, for example  $N = 300$ , into three regions as we did earlier in last section: region I is comprised of the defect-free hexagonal center, region II is a transition region between the two outer rings and the center region, and region III consists of the outermost two rings. The outer two rings have the same number of particles which varies between  $N_R=40$  and  $44$  depending on the value of  $\kappa$ .

We plot the radial-dependent mean square displacement for the three different regions and the angular square deviation of the two outer rings for three different values of  $\kappa$  in Fig. 5.10. We find that the melting always starts from the defect region as explained in the subchapter 5.2 (see also in Ref. [138]). From Fig. 5.10(a)-(c) we find that for a large system the melting temperature obtained from  $\langle u_{a1}^2 \rangle$  of the two outer rings is almost the same as the melting temperature obtained from  $\langle u_{a2}^2 \rangle$ . It means that the outer rings are always locked which is different for small clusters. Comparing Fig. 5.10(a,b) with Fig. 5.9, we see that in the case of a large system with small  $\kappa$  the radial and angular displacements start to increase rapidly at approximately the same temperature. Thus for large clusters with small  $\kappa$  value angular melting of the outer rings appears at the same temperature as the radial melting. But this is not the case for  $N = 300$  and  $\kappa = 16$  as shown in Fig. 5.10(c). The angular melting of the outer rings starts before the radial melting. The reason is that for large  $\kappa$  the defects are situated at the edge. This results in a radial melting of the outer rings which starts before the radial melting of the transition region and the center region. Moreover, the angular motion of the outer part is even easier to excite than the radial motion in the outer ring. This results in a lower angular than radial melting temperature at the edge. Thus also here the melting is a two-step process: first angular melting occurs than the radial melting.

## 5.4 CONCLUSIONS

In this chapter, we investigate the melting properties of 2D clusters. In the pure Coulomb system, the particle motion is found to be strongly related to the local topological structure. Our results clearly show that the melting of the clusters starts near the geometry induced defects, and that three melting temperatures can be obtained: for the defect region, the outer rings and the center region, respectively.

In the Yukawa system, the melting behavior is found to be strongly influenced by the screening parameter  $\kappa$ : a small cluster with a short-range interaction melts earlier than the one with long-range interaction. This was explained by the dependence of the energy barriers on  $\kappa$ . The two step melting processes are also found for small Yukawa clusters. Large clusters have a different melting scenario which is strongly influenced by the location of the defect region. The angular and radial melting temperatures coincide. A two-step melting can appear again for large systems with a high value of  $\kappa$ , if the defect region is situated at the edge of the system.

**Publications.** The results presented in this chapter were used in the following publications:

- Minghui Kong, B. Partoens and F. M. Peeters, *Topological defects and Non-homogeneous melting of large 2D Coulomb Clusters*, Phys. Rev. E **67**, 021608 (2003) (8 pages).
- Minghui Kong, B. Partoens, and F. M. Peeters, *Structural, dynamical and melting properties of two-dimensional Clusters of Complex Plasmas*, New Journal of Physics **5**, 23 (2003) (17 pages).

# 6

---

## *2D Clusters in a Magnetic Field*

### 6.1 INTRODUCTION

Recently, there has been an increased interest in the properties of complex plasmas in the presence of an axial magnetic field. Depending on the discharge conditions, rigid-body rotation and sheared rotation are observed [148]. Similar behaviors of a dust cluster is observed by experiments in an inductively-coupled rf plasma [149]. A coordinated study of a laboratory experiment found that the charged dust particles which were ordered in a ring showed angular rotation in which the structure stays intact, while they oscillate radially around the equilibrium orbit. This oscillatory rotational nature can be explained as a result of coupling between the Lorentz force and the harmonic confinement potential [150].

In the present chapter, the magnetic-field dependence of the normal mode spectra of 2D finite clusters of complex plasmas, which are confined by an external harmonic potential is presented. The dependence of the normal mode spectrum as a function of a perpendicular magnetic field is discussed. The nature of the eigenmodes is investigated and the corresponding divergence and rotor were calculated which describe the “shear-like” and “compression-like” modes, respectively.

The potential energy for such a system is already introduced in the second chapter of the model system, here we recall the main features. The dimen-

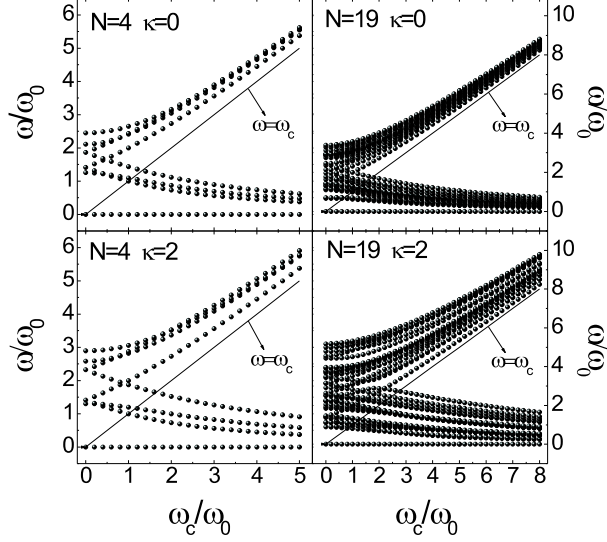


Fig. 6.1 Frequencies of the normal modes as a function of the cyclotron frequency for clusters with  $N = 4$  and  $N = 19$  ( $\kappa = 0$  and  $\kappa = 2$ ).

sionless Hamiltonian is given by

$$H = \sum_{i>j=1}^N \frac{\exp(-\kappa r_{ij})}{r_{ij}} + \sum_{i=1}^N r_i^2, \quad (6.1)$$

where we choose the units  $r_0 = (2q^2/m\epsilon\omega_0^2)^{1/3}$  for the length and  $E_0 = (m\omega_0^2 q^4/2\epsilon^2)^{1/3}$  for the energy. When  $\kappa = 0$ , the interaction between particles is a pure Coulomb potential.

The technique to obtain the ground state and the normal modes of the system in the presence of a perpendicular magnetic field is introduced before, in the following we only present the main numerical results.

## 6.2 RESULTS ON COMPLEX PLASMAS

In Fig. 6.1 we show typical spectra as a function of the cyclotron frequency  $\omega_c$  obtained for clusters with  $N = 4$  and  $N = 19$  ( $\kappa = 0$ ,  $\kappa = 2$ ) particles. The frequencies are split into two sets or bands with the same number of modes, which we call now “upper” band, in which the frequencies follow the cyclotron frequency (solid thin line), and “lower” band, in which the value of the frequencies decreases with the cyclotron frequency. In spite of the reduced number of particles, this behavior is in qualitative agreement with the experimentally observed spectrum of a gas of electrons (density  $\approx 10^8 \text{ cm}^{-2}$ )

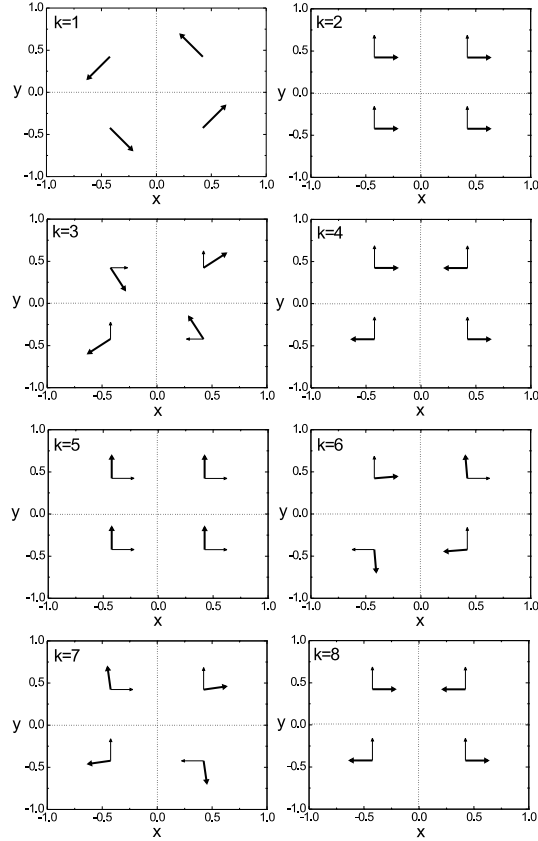


Fig. 6.2 Real (thick arrows) and imaginary (thin arrows) components of the eigenvectors for the cluster  $N = 4$ ,  $\kappa = 2$  in the presence of a perpendicular magnetic field  $\omega_c/\omega_0 = 5$ .

trapped in surface states above a liquid-helium surface [151]. The finite width of the two branches is not observed in an infinity system, and this effect is a consequence of the finite size of the cluster.

As can also be observed in Fig. 6.1, more clearly for  $N = 4$ , there are crossings of modes for some specific values of magnetic field. In general, the value of magnetic field in which the crossing of modes takes place is shifted to high values of  $\omega_c$  with increasing  $\kappa$ . For non-parabolic confinement this crossing becomes an anti-crossing of modes [152].

Under an applied magnetic field the degenerated center of mass ( $CM$ ) mode is split due to the fact that the magnetic field couples the  $x$ - and  $y$ -direction. One of the  $CM$  modes is observed in the lower band, while the other one in the upper band. This is a consequence of the coupling between the restoring force due to the confinement potential and the magnetic force.

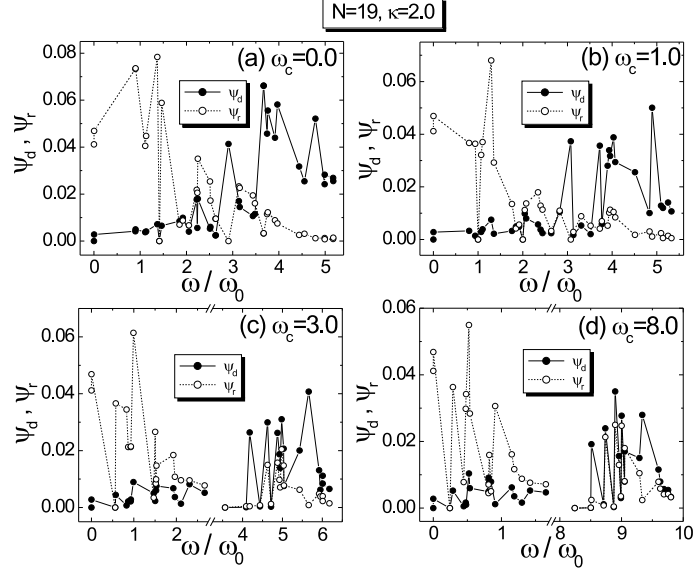


Fig. 6.3 The divergence ( $\psi_d$ ) and the rotor ( $\psi_r$ ) of the real components of the eigenvectors field as a function of the normal mode frequencies for the cluster  $N = 19$  ( $\kappa = 2$ ) in the presence of different axial magnetic field:  $\omega_c/\omega_0 = 0, 1, 3, 8$ .

When the magnetic force is in the same direction of the restoring force due to the parabolic confinement, the total restoring force is large, leading to the upper frequency. On the other hand, when the forces are in opposite directions, the resulting restoring force is small leading to a frequency which diminishes with increasing magnetic field, *i.e.* it behaves as  $1/\omega_c$  for large  $\omega_c$ .

In our finite cluster we specially noticed two kinds of excitation in the presence of a magnetic field. In the first one, all particles in the cluster can oscillate around their respective equilibrium position in a circular uniform motion, while in the other kind of mode some describe a rotational motion with a non-uniform velocity. In order to illustrate these modes we show, in Fig. 6.2, the real (thick arrows) and the imaginary (thin arrows) components of the eigenvectors field for the cluster  $N = 4$  ( $\kappa = 2$ ) in the presence of a uniform magnetic field ( $\omega_c/\omega_0 = 5$ ). The modes  $k = 1, 2, 3, 4$  are in the lower band, while the modes  $k = 5, 6, 7, 8$  are in the upper band. We noticed that, with exception of the mode  $k = 1$  ( $\omega/\omega_0 = 0$ ) which does not have an imaginary component, in some modes the real and imaginary components of the eigenvectors of all particles becomes perpendicular to each other and of equal magnitude for large magnetic field, resulting in a circular uniform motion. In the particular case showed in Fig. 6.2, only modes  $k = 2, 4, 5, 8$  have their real and imaginary eigenvectors already perpendicular to each other, and are of equal magnitude. However, we found that for larger values of the magnetic

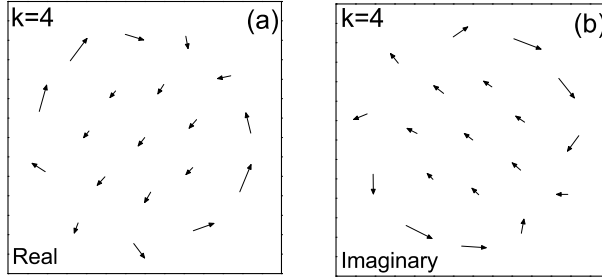


Fig. 6.4 Real (a) and imaginary (b) components of the eigenvectors for the mode  $k = 4$  of the cluster  $N = 19$ ,  $\kappa = 2$  in the presence of a perpendicular magnetic field  $\omega_c/\omega_0 = 5$ .

field the modes  $k = 6, 7$  also behave in the same way, while for the mode  $k = 3$  this behavior is not observed. In this last case, the real and imaginary eigenvectors never become perpendicular to each other with increasing magnetic field, and as a consequence, the particles describe a rotational motion with nonuniform velocity around their respective equilibrium positions.

All modes can have a shear-like or a compression-like character. The compressional and shear properties can be extracted from the divergence and rotor of the eigenvectors field. The results of the spatially resolved divergence and rotor of the different modes [138] for a Coulomb interacting 2D cluster in the absence of a magnetic field are presented in the fourth chapter.

Associating a single number, the shear-like and compression-like character of the different modes can be calculated by the spatial average of the divergence  $\vec{\nabla} \cdot \vec{A}$  and the rotor  $(\vec{\nabla} \times \vec{A})_z$  of the eigenvectors field. This approach follows from Ref. [48, 55] and is already introduced in the fourth chapter.

Depending on its value, the magnetic field can drastically modify the normal modes of the cluster introducing a more pronounced shear-like character. In order to emphasize the changing in the character of the modes, we calculated the divergence ( $\psi_d$ ) and the rotor ( $\psi_r$ ) of the real and imaginary components of the eigenvectors field. In Fig. 6.3, we show the real component of the eigenvectors as a function of the normal mode frequencies for the cluster  $N = 19$  ( $\kappa = 2$ ) in the presence of different magnetic fields ( $\omega_c/\omega_0 = 0, 1, 3, 8$ ). In the zero magnetic field case (see Fig. 6.3(a)), as already known [56], the rotor is activated only in the low frequency region, while the divergence is activated in the high-frequency limit. With increasing magnetic field, and as it can be observed in Fig. 6.3, the value of the rotor becomes equivalent to the one of the divergence in the high-frequency region of each band. The same behavior is observed for different values of the screening parameter  $\kappa$ . The divergence also presents a different behavior since it is smaller than the rotor in the high-frequency limit of the down band, when we increase the value of the magnetic field. The imaginary component of the eigenvectors presents a

very similar behavior of the real one. The presented features of the quantities  $\psi_r$  and  $\psi_d$  allow us to conclude that the shear-like character of the modes is increased due to the presence of the magnetic field.

The real and the imaginary part of the eigenvectors are not always directed perpendicular to each other, as was already commented. Another example of such a behavior is illustrated in Fig. 6.4, where the real and imaginary components of the eigenvectors for the cluster  $N = 19$  ( $\kappa = 2$ ) (in the presence of a magnetic field  $\omega_c/\omega_0 = 5$ ) are presented for the mode  $k = 4$ . As can be observed, both components exhibit a vortex-antivortex pair excitation which are  $90^\circ$  rotated with respect to each other. The central particle and the ones localized in the internal shell have their real and imaginary eigenvectors perpendicular to each other, while the particles in the most external shell do not present this feature.

In conclusion, we studied numerically the normal mode spectra and the eigenvectors of two-dimensional complex plasmas in the presence of an axial magnetic field. For large values of the magnetic fields the normal modes fall into two bands, a low frequency band with frequency  $\sim 1/\omega_c$ , and a high frequency band with frequency  $\sim \omega_c$ . We found that the frequencies of the normal modes are strongly dependent on the magnetic field intensity and the screening strength  $\kappa$ . It is shown that the “shear-like” character of the modes is increased due to the presence of the magnetic field.

**Publications.** The results presented in this chapter were used in the following publication:

- Minghui Kong, W. P. Ferreira, B. Partoens and F. M. Peeters, *Magnetic field dependence of the normal mode spectrum of a planar complex plasma cluster*, IEEE Transactions on Plasma Science, Vol. **32**, No. 2, 569, (2004) (4 pages).

7

---

# *Nonlinear Screening in Large 2D Coulomb Clusters*

## 7.1 INTRODUCTION

Classical point charges in a 2D infinite plane crystallise into a hexagonal lattice at low temperatures [67]. When the particles are confined by an external parabolic potential, there is a competition between the interparticle potential to form the bulk hexagonal lattice and the ring-like structure at the edge imposed by the circular-confinement potential [70]. In the transition region defects appear as dislocations and disclinations at the six corners of the hexagonal-shaped inner domain in the specific case of pure Coulomb interaction [138]. Much experimental [61, 69, 84] and theoretical work [121, 128, 134, 135, 138, 153] was devoted to the study of those topological defects in an infinite 2D classical Wigner Crystal and recently also in a finite size system.

However, in real experiments clusters are not always clean, impurities and/or defect particles with deviating mass and/or charge can be present. It will be very interesting to know the general role of the impurity potential on the ordered (lattice) structure. How such an impurity potential affects essential characteristics of a system such as, the topological charge, the density of states (DOS) of the normal modes, and the normal modes of the system, requires extensive studies.

Recently, the influence of a single mobile defect particle on the structure of a small classical 2D cluster was investigated [85], which explained recent experimental results of the configurations of a system of rotating magnetic disks [84]. Theoretical work on the structure of classical clusters consisting of two-species of charged particles with the same mass was reported recently

[154], where it was found that the species with the largest charge move towards the outer edge of the system. Very recently, nonlinear quantum screening in 2D electron gases was also investigated in Ref. [155] by using the density functional theory method.

Here we study the screening of a single fixed impurity (defect) with variable charge in a large 2D classical Coulomb system, which is confined by a circular parabolic potential. This case is essentially different from the previous studied system [85]: (1) the impurity is immobile, i.e. has an infinite mass, and (2) we consider large systems. Also unlike the study of Ref. [154] this impurity can have an arbitrary charge. In contrast to Refs. [85] and [154] we will also investigate the topological charge and the normal modes of the system.

This chapter is organized as follows. In Sec. 7.2, we shortly explain our theoretical model and the numerical approach. Sec. 7.3 discusses the ground state configuration and topological defects, while Sec. 7.4 is dedicated to the normal modes. In Sec. 7.5, the nonlinear screening of the impurity charge in these clusters are discussed. Our results are summarized in Sec. 7.6.

## 7.2 NUMERICAL APPROACH

The Hamiltonian of a 2D system of  $N$  equally charged particles in the presence of a single impurity with arbitrary charge placed in a parabolic confinement potential and interacting through pure Coulomb interaction is given by

$$H = \sum_{i=1}^N \frac{1}{2} m \omega_0^2 r_i^2 + \frac{e^2}{\varepsilon} \sum_{i>j}^N \frac{1}{|\vec{r}_i - \vec{r}_j|} + \frac{e^2}{\varepsilon} \sum_{i=1}^N \frac{q}{|\vec{r}_i - \vec{r}_q|}, \quad (7.1)$$

where  $m$  is the mass of the mobile particles,  $\omega_0$  the radial confinement frequency,  $\varepsilon$  the dielectric constant of the medium the particles are moving in,  $e$  the particle charge,  $q$  the impurity charge located at  $\vec{r}_q$ , and  $\vec{r}_i = (x_i, y_i)$  the position of the  $i$  particle with  $r_i \equiv |\vec{r}_i|$ , where the third term in Eq. (7.1) corresponds to the interaction between the mobile identical particles and the single fixed impurity with charge  $q$ .

We can write the Hamiltonian in dimensionless form if we express the coordinates and energy in the following units [70]:  $r_0 = (e^2/\varepsilon/\alpha)^{1/3}$ ,  $E_0 = (e^2/\varepsilon)^{2/3} \alpha^{1/3}$ , with  $\alpha = m\omega_0^2/2$ . The dimensionless Hamiltonian is given by

$$H = \sum_{i=1}^N r_i^2 + \sum_{i>j}^N \frac{1}{|\vec{r}_i - \vec{r}_j|} + \sum_{i=1}^N \frac{q}{|\vec{r}_i - \vec{r}_q|}. \quad (7.2)$$

To find the thermodynamic equilibrium configurations, we employed the Newton optimization technique [55] after the standard Monte Carlo (MC) routine [114]. This procedure was outlined and compared with the standard MC technique in the second chapter. The eigenmode frequencies are obtained

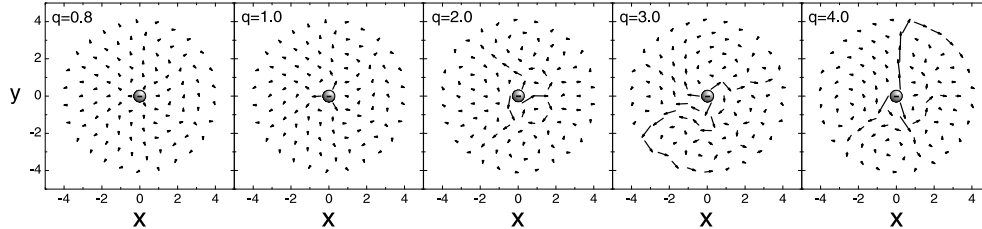


*Fig. 7.1* The displacement of the particles for different values of the impurity charge  $q$ . The impurity is situated in the center and its position is indicated by the solid dot. The arrows show the direction and length of the particles' displacement.

from the square root of the eigenvalues of the dynamical matrix and the eigenfrequencies will be expressed in units of  $\omega' = \sqrt{2}\omega_0$ .

### 7.3 GROUND STATE CONFIGURATIONS AND TOPOLOGICAL DEFECTS

In order to investigate the influence of the impurity, we consider clusters which are large enough to show a hexagonal lattice structure in the center. This is realized starting from around  $N = 100$  particles, although larger systems will also be simulated.

First, the ground state of a cluster with equal charges with one impurity fixed in the center is obtained. The displacement of the particles due to the presence of the impurity which is located in the center of the cluster is shown in Fig. 7.1 for  $N = 100$  particles and different values of the charge  $q$  of the impurity. The vectors show the direction and length of the displacement of the particles as a consequence of the introduction of the impurity.

From Fig. 7.1, we notice that when the impurity charge  $q \leq 1$ , only the center particles which are very close to the impurity are mainly displaced, in spite of the long range Coulomb interaction between the particles. In fact, a very small screening length was observed in this case. This will be discussed in more details in the next section. For larger values of the impurity charge, more particles are influenced. As can be seen in Fig. 7.1, the particles undergo vortex-like movements. This is a consequence of the circular confinement potential which keeps the particles in a finite region. Such a motion does not lead to any compression and guarantees the same density. For large values of the impurity charge the distortion in the lattice is larger and it propagates further away from the center of the cluster.

Next we resort to the Voronoi construction [127] in order to investigate the ordering of the particles and to reveal the topological nature of the particles arrangement. A detailed study of the topological defects in a confined 2D Coulomb cluster, in the absence of the impurity, was previously reported in

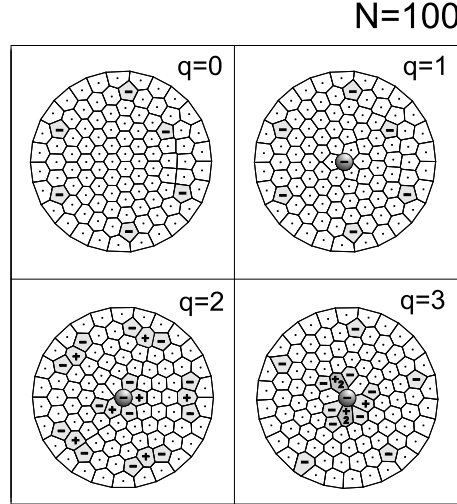


Fig. 7.2 The Voronoi structure where the defects (i.e. disclinations) are indicated by ‘2+’ for a 8-fold, ‘+’ for a 7-fold and by ‘-’ for a 5-fold coordination number.

the third chapter (see also Ref. [138]). These defects appear as a consequence of the adjustment of a triangular lattice to a circular region. However, when an impurity charge is present, and depending on its value, the number of defects increases.

In Fig. 7.2 we show the Voronoi constructions of the ground-state configuration of a cluster with  $N = 100$  particles and with an impurity charge of variable value fixed at the point  $(0, 0)$ . In the absence of the impurity charge, the ground-state configuration of the system with  $N = 100$  particles presents the minimum number of defects, i.e., six, which is equal to the net topological charge. In addition, all topological defects are located at the transition region which is between the central hexagonal structure and the outer rings.

When the system has one identical impurity charge ( $q = 1$ ) at the center, the number of defects is still equal to six, and all of them are located in the transition region of the cluster. For larger values of the impurity charge, topological defects start to appear in the center region of the cluster, and the lattice distortion gets bigger. Because a large impurity charge will strongly repel the neighboring particles, an empty space will appear in the center region. As a consequence the hexagonal lattice structure is strongly distorted and more defects will appear around this circle. Notice that some defects near the circle can have an eight fold coordinate number (indicated by ‘+2’), which does not happen in 2D clusters in the absence of the impurity charge. However, we want to stress that for all values of the impurity charge, the net topological charge  $N_- - N_+$  is always equal to six.

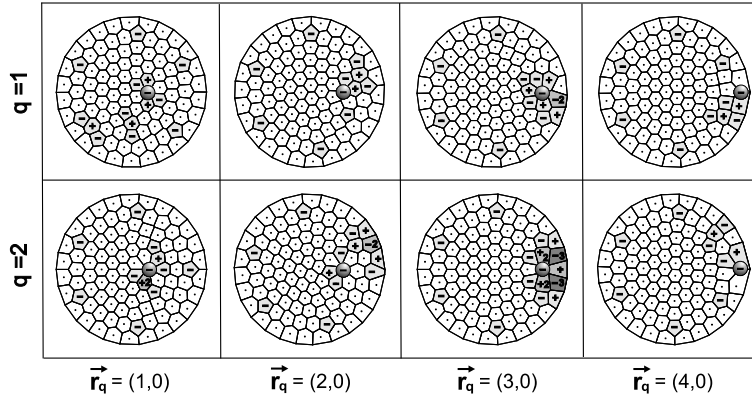


Fig. 7.3 The same as Fig. 2 but where now the impurity charge is displaced from its central location. The upper (lower) row of figures corresponds to an impurity with single (double) charge and results are given for different positions of the impurity  $\vec{r}_q$ .

Another interesting phenomena is that the total number of defects ( $N_- + N_+$ ) first increases with increasing impurity charge till  $q \simeq 2.4$ . Further increasing the impurity charge leads to a decrease of the total number of defects. This can be explained together with the nonlinear screening behavior in the next section by the competition between the different forces active in the system.

In Fig. 7.3 we present the Voronoi construction for the ground state configurations in the cases of two particular values of the impurity charge, i.e.,  $q = 1$  and  $q = 2$ . In addition the impurity's position is moved away from the center of the system. As can be observed, the net topological charge  $N_- - N_+$  of the system, in spite of the different values and positions of the impurity charge is always equal to six.

These results are in agreement with the Euler theorem [134], which is based on the circular symmetry of the confinement potential. It is clear that the presence of the impurity does not change the net topological charge.

## 7.4 NORMAL MODES

For systems without impurity, it is known that the lowest non-zero excitation corresponds with an intershell rotation for small clusters and with a vortex-antivortex motion for large clusters [55]. Fig. 7.4 shows some examples of these lowest non-zero frequency (LNF) modes for  $N = 100$  particles in the presence of an impurity charge  $q$ . Notice that for  $q < 5$ , a vortex-antivortex excitation still corresponds with the LNF, while for larger values of the im-

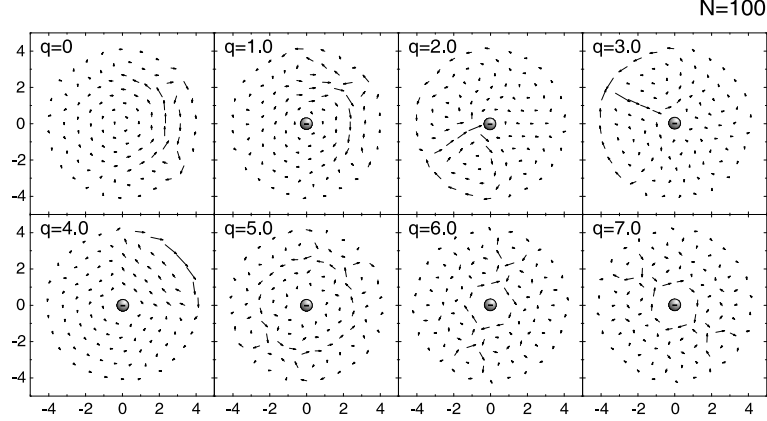


Fig. 7.4 Vector plot of the lowest non-zero eigenfrequency for the cluster with  $N = 100$  particles for different values of the impurity charge  $q$ .

purity charge ( $q \geq 5$ ) the LNF mode corresponds to a circular motion around the impurity and concomitant smaller local circular motions near the edge.

For a parabolic confinement, it is well known that there are three eigenfrequencies which are independent of  $N$  [55]:  $\omega = 0, \sqrt{2}$  and  $\sqrt{6}$ , which correspond to the rotation of the system as a whole, the center of mass (CM) mode and the breathing mode (BM), respectively. The BM mode was recently measured experimentally [47, 73]. In the system with a central impurity, the rotation of the system as a whole does not change, because the symmetry of the system is not broken. The CM mode is destroyed by this fixed impurity and the new mode will go around the impurity in the center, so it can no longer be called a CM mode.

However, the BM mode with  $\omega/\omega' = \sqrt{6}$  still survives and its value does not depend on the charge of the impurity. This can also be obtained analytically. From Eq. (7.2), the Hamilton equation of motion yields

$$\dot{v}_{xi} = -\frac{\partial H}{\partial x_i} = -2x_i + \sum_{j \neq i}^N \frac{x_i - x_j}{|\mathbf{r}_i - \mathbf{r}_j|^3} + q \sum_{i=1}^N \frac{x_i - x_q}{|\mathbf{r}_i - \mathbf{r}_q|^3}. \quad (7.3)$$

Here the impurity is fixed in the center, so  $\vec{r}_q \equiv (x_q, y_q) = (0, 0)$ . With this result, one obtains for the mean square radius  $R^2 = \sum_1^N (x_i^2 + y_i^2)$ ,

$$\frac{d^2 R^2}{dt^2} = -6R^2 + 2(H + T), \quad (7.4)$$

with  $T = \sum_i (\dot{x}_i^2 + \dot{y}_i^2)$  the total kinetic energy. So we see that the breathing mode still survives with frequency  $\sqrt{6}$  for the system with a fixed central impurity.

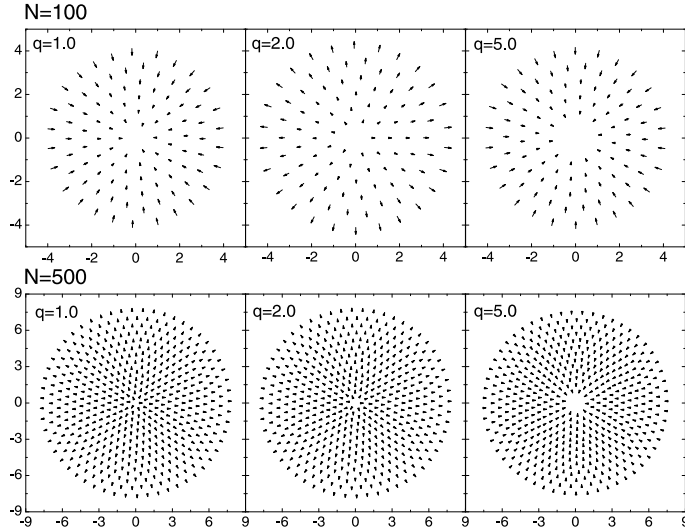


Fig. 7.5 The breathing-modes for some particular values of the impurity charge  $q$  for the clusters with  $N = 100$  and  $N = 500$  particles. In all cases, the BM has the same frequency  $\omega' = \sqrt{6}$ .

We plot in Fig. 7.5 several typical cases for the breathing mode for  $N = 100$  and  $N = 500$  particles in the case the impurity is located in the center of the confinement potential. But when the impurity is not in the center, the BM is strongly modified and its frequency is different from  $\sqrt{6}$ .

The density of states (DOS) of the normal modes (phonons), in the absence of the impurity, was investigated before [55]. This is obtained by a summation of the energy levels within some small energy region. It shows that all large clusters have two clear broad maxima which is in qualitative agreement with the case for an infinite system[67]. We compare the DOS for a large system with  $N = 500$  particles with the situation for a fixed central impurity with two different values of its charge, i.e.,  $q = 1, 2.6$ . Here a larger system with  $N = 500$  particles is considered and we take  $\delta\omega = \omega_{max}/20$  as the frequency interval, where  $\omega_{max}$  is the maximum eigenfrequency. In Fig. 7.6, one can see that the system's DOS does not change too much in these two cases with or without the fixed impurity.

As we know, a finite confined cluster has compression-like and shear-like modes. The compressional and shear-like properties can be extracted from the divergence and rotor of the velocity field, respectively. In this paper, we will associate a single number to the shear-like and compression-like character of the different modes by calculating the spatial average of the square of the divergence  $\vec{\nabla} \cdot \vec{v}$  and the rotor  $(\vec{\nabla} \times \vec{v})_z$  of the velocity field, following the approach of Refs. [48, 55, 56].

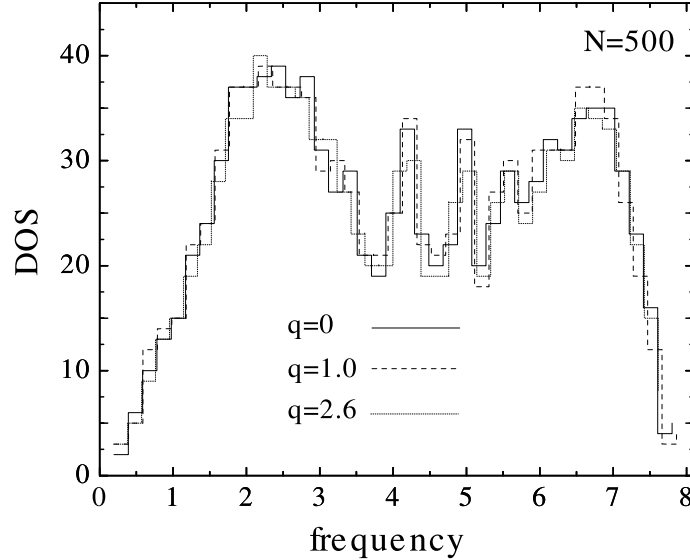


Fig. 7.6 Density of phonon states for clusters with  $N = 500$  particles in the presence of a central impurity for different values of the impurity charge  $q$ .

We plotted in Fig. 7.7 the divergence  $\psi_d(k)$  and rotor  $\psi_r(k)$  as a function of the excitation frequency for  $N = 500$  particles for different values of the charge of the impurity. One can see from this picture that the system doesn't change qualitatively its overall shear-like and compression-like character when an impurity is present even when the impurity charge is increased.

## 7.5 NONLINEAR SCREENING

Screening of the impurity charge is a fundamental property of a gas of charge carriers. Such a screening is characterized by the displacement of the carriers when an impurity is placed in a uniform gas of carriers [156].

We investigate the behavior of the screening length as function of the charge of the impurity for a large 2D cluster with  $N = 500$  charged particles. In order to quantify the influence of the impurity charge on the system, we will consider here an average deviation of the particles' position before and after the impurity charge is placed in the system. To do so, we initially define, for each particle, the displacement due to the presence of the impurity charge  $\Delta_i = |\mathbf{r}_i^{after} - \mathbf{r}_i^{before}|$ .

The system is divided into 25 concentric rings with a certain width each containing 20 particles. In every ring  $i$  an average displacement is calculated  $\Delta_j = \sum \Delta_i / 20$  where the summation  $i$  sums over the particles in ring  $j$ . In

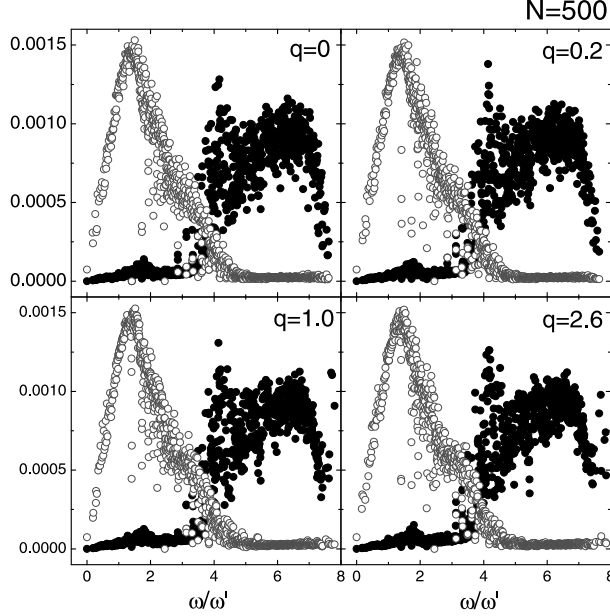


Fig. 7.7 Divergence  $\psi_d(k)$  (solid dots) and rotor  $\psi_r(k)$  (open dots) as a function of the excitation frequency for  $N = 500$  particles for different values of the impurity charge  $q$ .

this way we obtain the average deviation  $\Delta$  as a function of the distance in the radial direction from the center of the cluster.

In Fig. 7.8, we present  $\Delta$  as a function of the distance along the radial direction  $r$ , for different values of the impurity charge  $q$  in a cluster with  $N = 500$  particles. The inset shows the same plot, but in a logarithmic scale. As can be observed, the edge particles are much less affected by the impurity charge than the central particles. The interaction between the impurity and the particles clearly presents two different regimes, which are related to the value of the impurity charge. When  $q < 1$ , the quantity  $\Delta$  becomes almost zero at the extremity of the cluster, indicating that the interaction is strongly screened. On the other hand, when  $q > 1$ , the quantity  $\Delta$  is considerable larger even at the edge of the cluster. Notice also that the value of  $\Delta$  at the border of the system seems to saturate when  $q > 2$ .

We fit these deviation curves  $\Delta(r)$  using the function (i.e. Yukawa potential formation)

$$\Delta r_i = \alpha(e^{-r_i/\lambda}/r_i) + r_0 \quad (7.5)$$

where  $\lambda$  is the screening length,  $\alpha$  a constant and  $r_0$  is a measure of the expansion of the system as a whole. The results for the screening length as a function of the impurity charge  $q$  are shown in Fig. 7.9. There is a clear nonlinear relationship between  $\lambda$  and the impurity charge  $q$ . The screening

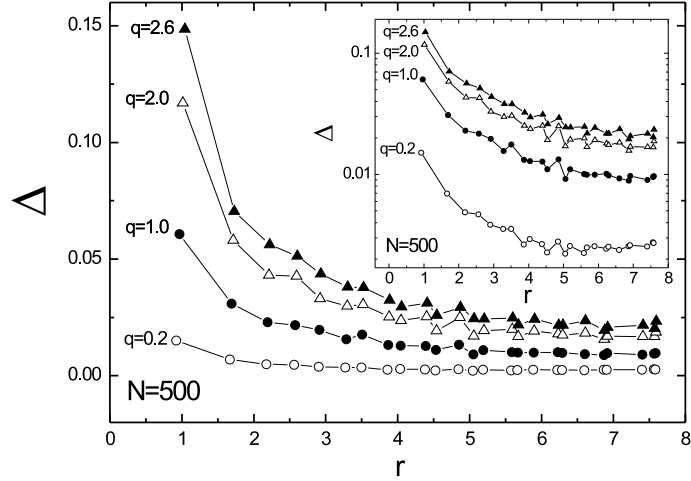


Fig. 7.8 The deviation  $\Delta$  of the radial position of the particles as function of  $r$  for different values of the impurity charge  $q$  for a system consisting of  $N = 500$  particles. The inset shows  $\Delta$  in a logarithmic scale.

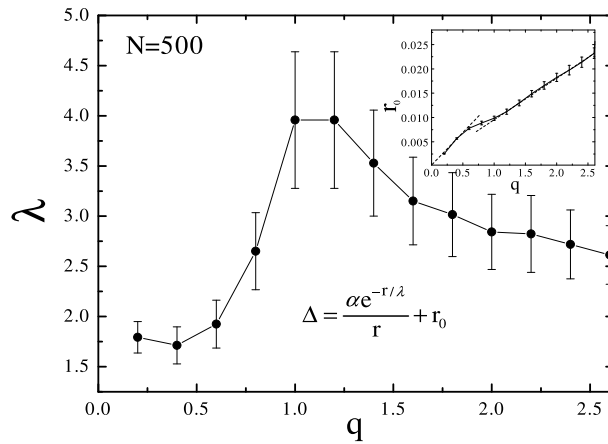


Fig. 7.9 The screening length as a function of the impurity charge  $q$  for clusters consisting of  $N = 500$  particles. The inset shows the  $q$ -dependence of the radial displacement at large distances from the impurity. The dotted lines show the extrapolated small and large  $q$  behaviour.

length is almost constant for  $q < 0.5$ , it rapidly increases with increasing value of the impurity charge, in the interval  $0.5 \leq q \leq 1$ . For  $1.0 \leq q \leq 1.2$ , the screening length reaches its maximum value. When  $q > 1.2$ , the screening parameter decreases slowly with increasing value of the impurity charge. In the inset of Fig. 7.9, we notice that the  $r_0 - q$  dependence exhibits three

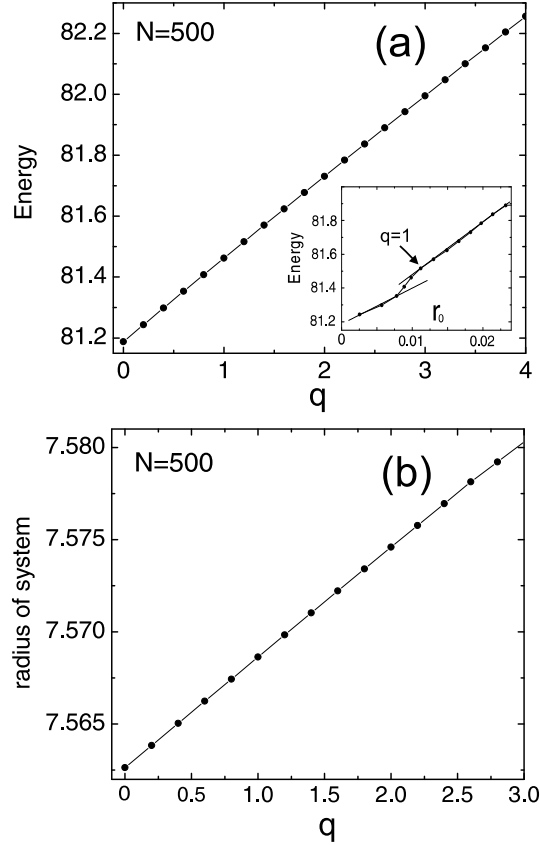


Fig. 7.10 The energy(a) and radius(b) of the system as a function of the impurity charge  $q$ . The inset of (a) shows the energy of the system as a function of  $r_0$ .

different regimes with a  $r_0 - q$  linear dependence for  $q < 0.5$  and  $q > 1$ , and a transition region for  $0.5 < q < 1$ .

This non-linear screening behavior can be understood as follows. From Fig. 7.1, we know that for small values of  $q$  till  $q < 1.2$  the particles near the central region have much larger displacements than the particles near the edge, which are less influenced by the external impurity charge. In this case the system is strongly screened. By increasing the impurity charge  $q$ , the radius of the system grows linearly (see Fig. 7.10(b)). However, the displacement of the particles is not homogeneous in the clusters. The maximum of the screening length is reached for  $q = 1.0 \sim 1.2$ . In this case the difference between the displacements of particles around the center and the edge is largest. At the same time, more defects will appear in the system. Further increasing the impurity charge  $q$  leads more and more to a homogenous displacement in all

regions (i.e. a central hole is created by the impurity as is clearly seen in Fig. 7.4 and Fig. 7.5), leading to a decrease of the screening length.

The non-linear behavior of the screening length is a consequence of the balance among the effect of the impurity repulsive force, the interaction between the charged particles of the system, and the circular confinement potential.

We plot the energy and outer radius of the system as a function of the impurity charge  $q$  in Fig. 7.10. In the inset of Fig. 7.10(a), the energy of the system as a function of  $r_0$  is shown. Notice that both the energy and the radius of the system present an almost linear dependence on the impurity charge. The size of the system linearly increases with the impurity charge (Fig. 7.10 (b)). Notice that the outer radius and the uniform increment  $r_0$  (see Eq. (7.5)) do not have a one-to-one relation because of the first term on the right hand side of Eq. (7.5) which is different from zero at the edge of the system. From the inset of Fig. 7.10(a), we notice two regimes with a different linear  $E - r_0$  dependence. The transition region occurs for  $r_0 \simeq 0.01$  which corresponds to  $q \simeq 1$  and this is just the region where  $\lambda$  is maximal.

## 7.6 CONCLUSIONS

In this chapter, we investigated 2D large clusters consisting of identical charged classical particles having a single probe impurity. All interactions are pure Coulombic. The ground-state configuration is obtained through the Monte Carlo simulation technique. The presence of an impurity charge in the system does not modify the net topological charge ( $N_- - N_+$ ) of the system, which is always equal to six. In comparison with a 2D cluster without impurity charge, only the breathing mode remains unchanged if the impurity is located in the center of the confinement potential. The DOS and the shear-like or compression-like character of normal modes of the system do not change considerably by this impurity as well. A clear nonlinear relationship between the screening length  $\lambda$  and the impurity charge is found. For values of the impurity charge smaller than the charge of the other particles, the system has almost a screening strength independent on the charge of the impurity. For larger values of the impurity charge, the system exhibits a clear nonlinear screening length. This result can be explained by the competition between the different forces active in the system.

**Publications.** The results presented in this chapter are submitted for publication as:

- Minghui Kong, A. Vagov, B. Partoens, F. M. Peeters, W. P. Ferreira, and G. A. Farias, *Nonlinear screening in large two-dimensional Coulomb clusters*, submitted to Phys. Rev. B.

# 8

---

## *Summary*

The aim of this thesis is to study in detailed how the structural, dynamical and melting properties of a *finite* size classical Wigner crystal are modified with respect to an infinite two-dimensional (2D) Wigner lattice .

In **chapter 1**, a general overview of the present PhD work is given. Also the concept of Wigner crystallization is introduced and examples of experimental realized systems are given. For example, electrons above liquid He, complex plasmas, colloidal systems, stainless-steel balls on a plane conductor, and the magnetized disks located at the liquid-air interface are described in detail. Other related systems are also introduced. Additionally, previous theoretical results obtained on classical clusters are discussed.

In **chapter 2**, I give a description of the model system and the numerical approach which is used to obtain the ground-state configuration and the eigenmodes. The Monte Carlo simulation technique, the Newton method and the method to calculate the saddle points in the energy landscape are given. To investigate the temperature dependence of the system, we use the standard Metropolis algorithm. The numerical technique to calculate 2D classical clusters in a perpendicular magnetic field is presented.

In **chapter 3**, we extend the previous results of Bedanov and Peeters for the ground-state configurations of small pure Coulomb clusters to other functional forms for the interparticle interaction and to different functional forms for the confinement potential.

In this chapter we investigate the ground state configuration for both small and large clusters. The first part of this chapter deals with the study of the system interacting through a pure Coulomb potential and confined in a parabolic

trap. A detailed study on the ground state configuration together with the different metastable states is given. The configuration changes when the system transits from the ground state to different metastable states. Here the saddle point states, which are the critical states in the transition between the ground state and the metastable states, are studied, from which the potential barriers are obtained.

We also investigate large systems. For large clusters we use the defect theory to get a better understanding of the topological nature of the cluster structure and use therefore the Voronoi construction technique. For a large number of particles in the cluster the configuration is determined by two competing effects, namely in the center a hexagonal lattice is formed, which is the ground-state for an infinite 2D system, and the confinement which imposes its circular symmetry on the outer edge. As a result a hexagonal Wigner lattice is formed in the central area while at the border of the cluster the particles are arranged in rings. In the transition region defects appear as dislocations and disclinations at the six corners of the hexagonal-shaped inner domain. The topological charge ( $N_- - N_+$ ) is always found to be equal to six. The particles motion is found to be strongly related to the topological structure.

In the second part of this chapter, we study the properties of the clusters interacting through a screened Coulomb potential, i.e. a Yukawa potential, in a complex plasma. We find that for a small number of particles, the ground-state configuration consists of a ring structure which transforms into a hexagonal structure with decreasing screening length. For large clusters, geometry induced defects appear and the location of the defects depends on the screening length. Also results for other different interparticle potential interactions, e.g., dipole potential and logarithmic potential are given.

At the end of this chapter, the structural properties of 2D clusters which are confined in an external hard wall potential are investigated. In a hard wall confined system the physics is very different, e.g. there is a very inhomogeneous distribution of particles because many of them are pushed to the edge of the system where they create a non-parabolic confinement potential for the other particles. The configurational properties of 2D clusters show an inhomogeneous distribution and more particles can sit at the edge in comparison with the parabolic case, and the shell structure is much more pronounced, also for large clusters. The ground state configuration is investigated as a function of the inter-particle interaction (Coulomb, dipole, logarithmic and screened Coulomb) and compared with the parabolic case. In the case of long range Coulomb interaction between the particles, the density of particles is increased towards the edge, while the particles are more uniformly distributed for a short range interaction potential like e.g. for the dipole interaction.

We studied the dynamical properties, i.e. the normal vibration modes of such a crystal in **chapter 4**. The excitation spectrum corresponding to the ground-state configuration of the 2D clusters is discussed in this chapter with

different inter-particle interactions (Coulomb potential and Yukawa potential).

For parabolic confinement, the shear and compression content of the modes was calculated and it was found that for large  $N$  the lower half of the eigenfrequency spectrum are mostly “shear-like” modes, while the upper half of the spectrum contains the “compression-like” modes. In a complex plasma, the frequency of the eigenmodes were investigated as function of the screening length.

In a hard wall confinement potential, the eigenmodes of the cluster were also investigated, which showed different physics in comparison to a parabolically confined cluster. In this case, center of mass and breathing modes can be identified approximately for the central particles, while the lowest non-zero frequency (which is related to the stability of the cluster) corresponds with a rotation of the central particles as a whole (in the opposite direction to the particles at the edge). Larger frequency modes correspond with many different types of intershell rotations, followed by vortex/anti-vortex excitations. The highest frequencies involve large amplitudes for angular movement of particles at the edge, as they are almost frozen in the radial direction. Also the shear- and compression-like character of the modes was investigated. A clear distinction can be made between low-frequency shear-like modes and high-frequency compression-like modes. The highest frequency modes are again shear-like modes, corresponding with the motion of the particles at the edge.

In **chapter 5**, we investigated the melting properties in classical finite clusters. We first reported the melting process in a large system in which the particles interact with a pure Coulomb interaction. The particle motion is found to be strongly related to the local topological structure. Our results clearly show that the melting of the clusters starts near the geometry induced defects, and that three different melting temperatures can be obtained: for the defect region, the outer rings and the center region, respectively.

In the subsequent section, the melting properties of a complex plasma were studied which showed a complicated scenario because of the different inter-particle interaction potential. The melting behavior is found to be strongly influenced by the screening length: a small cluster with a short-range interaction melts earlier than the one with long-range interaction. This was explained by the dependence of the energy barriers on the screening length. The two-step melting processes are also found for small Yukawa clusters. Large clusters have a different melting scenario which is strongly influenced by the location of the defect region. The angular and radial melting temperatures coincide. A two-step melting process was found for large systems with a small value of the screening length, if the defect region is situated at the edge of the system.

In previous chapters, no magnetic field was present. We investigated the influence of a magnetic field on the classical 2D clusters in **chapter 6**. In this chapter, the magnetic field dependence of the normal mode spectra of 2D finite clusters of complex plasmas which are confined by an external harmonic

potential is presented. The dependence of the normal mode spectrum as a function of a perpendicular magnetic field is discussed. For large values of the magnetic field the normal modes fall into two bands, a low frequency band with frequency  $\sim 1/\omega_c$ , and a high frequency band with frequency  $\sim \omega_c$ . The nature of the eigenmodes is investigated and the corresponding divergence and rotor were calculated which describe the “shear-like” and “compression-like” modes, respectively. We found that the frequencies of the normal modes are strongly dependent on the magnetic field intensity and the screening length. It is shown that the “shear-like” character of the modes is increased due to the presence of the magnetic field.

In the last chapter, **chapter 7**, we investigated the screening of a single fixed impurity (defect) with variable charge in a large 2D classical Coulomb system which is confined by a circular parabolic potential.

The distortion due to a fixed point impurity with variable charge placed in the center of a classical harmonically confined two-dimensional (2D) large Coulomb cluster was studied. We find that the net topological charge ( $N_- - N_+$ ) of the system is always equal to six independent of the position and charge of the impurity. In comparison with a 2D cluster without impurity charge, only the breathing mode remains unchanged. The screening length is found to be a highly nonlinear function of the impurity charge. For values of the impurity charge smaller than the charge of the other particles, the system has almost the same screening strength. When the impurity charge is larger, the screening length is strongly enhanced. This result can be explained by the competition between the different forces active in the system.

# 9

---

## *Samenvatting*

Deze thesis bestudeert in detail de structurele en dynamische eigenschappen en het smelten van een eindig Wignerkristal en onderzoekt hoe deze verschillen met die van een oneindig tweedimensionaal (2D) Wignerrooster.

In **hoofdstuk 1**, wordt een algemeen overzicht gegeven van dit doctoraatswerk en wordt ook het begrip Wignerkristal ingevoerd. Verder in het hoofdstuk worden verschillende voorbeelden gegeven van experimentele systemen die gerealiseerd werden om de statische en dynamische eigenschappen van klassieke 2D Wignerkristallen te bestuderen. Zo worden bijvoorbeeld elektronen boven vloeibaar He, complexe plasma's, colloïdale systemen, roestvrij stalen ballen op een vlakke geleider, en magnetische schijfjes op een vloeistof/lucht-scheidingsvlak in detail beschreven. Andere verwante systemen worden ook geïntroduceerd. Daarenboven worden de vorige theoretische resultaten op klassieke clusters besproken.

In **hoofdstuk 2** geef ik een beschrijving van het modelsysteem en de numerieke benadering die gebruikt wordt om de grondtoestandsconfiguratie en de eigentrillingen te bekomen. De Monte-Carlo-simulatietechniek, de Newtonmethode en de methode om de zadelpunten in het energielandschap te berekenen, worden toegelicht. Om de temperatuursafhankelijkheid van het systeem te bestuderen, gebruiken we het standaard Metropolis-algoritme. Eveneens wordt de numerieke methode voorgesteld om de 2D klassieke clusters in een loodrecht magneetveld te berekenen.

In **hoofdstuk 3** breiden we de vorige resultaten van Bedanov en Peeters voor de grondtoestandsconfiguraties van parabolische Coulombclusters uit

naar andere interactietypes en naar verschillende functionele vormen van de opsluitingspotentiaal.

In dit hoofdstuk onderzoeken we de grondtoestandsconfiguraties voor kleine en grote clusters. Het eerste deel van dit hoofdstuk handelt over de studie van het systeem, interagerend via een zuivere Coulombpotentiaal en opgesloten in een parabolische potentiaal. Een gedetailleerde studie van de grondtoestandsconfiguratie, tesamen met de verschillende metastabiele toestanden, wordt gegeven. De configuratie verandert wanneer het systeem overgaat van de grondtoestand naar meta-stabiele toestanden. Hier bestuderen we de zadelpunttoestanden, de kritieke toestanden tijdens de overgang tussen de grondtoestand en de metastabiele toestanden, om zo de potentiaalbarrières te bekomen.

We onderzoeken ook grote systemen. Voor grote clusters gebruiken we de defecttheorie om de topologische natuur van de clusterstructuur beter te begrijpen en daarvoor gebruiken we de Voronoiconstructietechniek. Voor een groot aantal deeltjes in de cluster wordt de configuratie bepaald door twee concurrerende effecten, namelijk het hexagonale rooster, de grondtoestand voor een oneindig 2D systeem, en de opsluiting die de cirkelsymmetrie van de buitenrand oplegt. Het resultaat is dat een hexagonaal Wignerrooster gevormd wordt in het centrale gebied, terwijl de deeltjes naar de rand toe in ringen geordend zijn. In het overgangsgebied verschijnen defecten als dislokaties en disclinaties op de zes hoeken van het hexagonaal gevormde inwendige domein. De beweging van de deeltjes blijkt sterk verbonden te zijn met de topologische structuur.

In het tweede deel van dit hoofdstuk bestuderen we de eigenschappen van de clusters die interageren via een afgeschermd Coulombpotentiaal, of een Yukawapotentiaal, in een complex plasma. We vinden dat voor een klein aantal deeltjes, de grondtoestandsconfiguratie bestaat uit een ringstructuur die verandert in een hexagonale structuur met afnemende afschermingslengte. In het geval van grote clusters verschijnen door de geometrie geïnduceerde defecten en de posities van de defecten hangen af van de afschermingslengte. Ook worden de resultaten van andere interactiepotentialen tussen de deeltjes gegeven, bv. de dipoolpotentiaal en de logaritmische potentiaal.

Op het einde van dit hoofdstuk worden de structurele eigenschappen van 2D clusters onderzocht, die opgesloten zijn door een harde-wand opsluitingspotentiaal. In een systeem, opgesloten in een harde-wand, is de fysica heel verschillend. Er is, bijvoorbeeld, een inhomogene verdeling van de deeltjes omdat vele deeltjes naar de rand van het systeem geduwd worden waar ze zo een niet-parabolische opsluitingspotentiaal creëren voor de andere deeltjes. De configurationele eigenschappen van 2D clusters tonen een inhomogene verdeling en meerdere deeltjes kunnen aan de rand zitten in vergelijking met de parabolische opsluiting, en de schillenstructuur is meer uitgesproken, zelfs voor grotere clusters. De grondtoestandsconfiguratie is onderzocht als functie van de vorm van de interactiepotentiaal tussen de deeltjes (Coulomb, dipool, logaritmisch en afgeschermd Coulomb) en vergeleken met de resultaten voor de parabolis-

che opsluitingspotentiaal. In het geval van lange-dracht-Coulombinteractie tussen de deeltjes vermeerderd de deeltjesdichtheid naar de rand toe, terwijl deeltjes meer uniform verdeeld zijn in het geval van een korte-dracht-interactiepotentiaal, zoals bijvoorbeeld bij de dipoolinteractie.

In **hoofdstuk 4** bestuderen we de dynamische eigenschappen, d.w.z. de eigenfrequenties en eigentrillingen van zo'n kristal. In het volgende hoofdstuk zullen we dan de smelteigenschappen bestuderen. Het excitatiespectrum van de grondtoestandsconfiguratie van 2D clusters wordt besproken in dit hoofdstuk voor verschillende vormen van de interactiepotentiaal (Coulombpotentiaal en Yukawapotentiaal).

In de parabolische opsluiting werden de schuif-mode en compressie-mode inhoud van de modes berekend en we vonden dat voor een groot aantal deeltjes de laagste helft van het frequentiespectrum vooral schuif-modes zijn, terwijl in de bovenste helft van het spectrum de compressie-modes terug te vinden zijn. In een complex plasma werd de frequentie van de eigenmodes als functie van de afschermingslengte onderzocht.

Ook in een harde-wandopsluitingspotentiaal werden de eigenmodes van de cluster onderzocht, wat een andere fysica toont in vergelijking met een parabolisch opgesloten cluster. In dit geval kunnen de massa-centrum-mode en de 'breathing'-mode voor de centrale deeltjes bij benadering geïdentificeerd worden, terwijl de laagste frequentie verschillend van nul (die verband houdt met de stabiliteit van de cluster) overeenkomt met een gezamenlijke rotatie van de centrale deeltjes (in tegengestelde richting van de deeltjes aan de rand). Hogere frequenties corresponderen met vele verschillende soorten rotaties van de ringen onderling, gevolgd door vortex/anti-vortex excitaties. De hoogste frequenties omvatten grotere amplitudes voor angulaire bewegingen van de deeltjes aan de rand, alsof ze in de radiale richting bijna aan de rand bevroren zijn. Ook werd het schuif-mode- en compressie-mode-karakter van de modes onderzocht. Een duidelijke onderscheiding tussen lage frequentie schuif-modes en hoge frequentie compressie-modes kan gemaakt worden. De hoogste frequentiemodes zijn echter opnieuw schuif-modes die overeenkomen met de beweging van de deeltjes aan de rand.

In **hoofdstuk 5** onderzochten we de smelteigenschappen in klassieke eindige clusters. We bestuderen eerst het smeltproces in een groot systeem waarin de deeltjes interageren via een zuivere Coulombinteractie. De beweging van de deeltjes is sterk verbonden met de locale topologische structuur. Onze resultaten tonen duidelijk aan dat het smelten van de clusters begint in de buurt van de door de geometrie geïnduceerde defecten, en dat drie verschillende smelttemperaturen verkregen kunnen worden: voor de defectenzone, de buitenste ringen en het centrale gebied.

In het daaropvolgende deel worden de smelteigenschappen van een complex plasma behandeld wat een ingewikkeld scenario toont omwille van de verschillende interactiepotentialen. Het smeltgedrag wordt sterk beïnvloed door de afschermingslengte: een kleine cluster met een korte-drachtinteractie smelt

eerder dan een met een lange-drachtinteractie. Dit werd verklaard door de afhankelijkheid van de energiebarrières van de afschermingslengte. Het twee stappen smeltproces werd ook gevonden voor kleine Yukawaclusters. Grotere clusters hebben een verschillend smeltscenario, dat sterk beïnvloed wordt door de locatie van de defectzone. De angulaire and radiale smelttemperaturen vallen samen. Het twee stappen smeltproces kan opnieuw verschijnen voor grote systemen met een kleine afschermingslengte, als de defectzone gesitueerd is aan de rand van het systeem.

We hebben de invloed van een magneetveld op de klassieke 2D clusters onderzocht in **hoofdstuk 6**. In dit hoofdstuk wordt de magneetveldafhankelijkheid onderzocht van de frekwentiespectra van 2D eindige clusters van complexe plasma's, die opgesloten zijn door een externe harmonische potentiaal. De afhankelijkheid van dit spectrum als functie van een loodrecht magneetveld wordt besproken. Voor hoge magneetvelden valt het frekwentiespectrum uiteen in twee banden, een lage frekwentieband met frekwentie  $\sim 1/\omega_c$  en een hoge frekwentieband met frequentie  $\sim \omega_c$ . De natuur van de eigentrillingen werd onderzocht en de corresponderende divergentie en rotor werden berekend, die de schuif-mode en de compressie-mode inhoud beschrijven. We vonden dat de frekwenties van de modes sterk afhankelijk zijn van de magneetveldintensiteit en de afschermingslengte. Er wordt aangetoond dat het schuif-mode karakter van de modes verhoogd is tengevolge van de aanwezigheid van het magneetveld.

In het laatste hoofdstuk, **hoofdstuk 7**, onderzochten we de afscherming van één enkele vaste onzuiverheid (een defect) met variabele lading in een groot 2D klassiek Coulombsysteem dat opgesloten is door een cirkelvormige parabolische potentiaal. We bestudeerden de vervorming te wijten aan een vaste puntonzuiverheid met een variabele lading, geplaatst in het centrum van een klassieke harmonisch opgesloten 2D grote Coulombcluster. We vonden dat de netto topologische lading ( $N_- - N_+$ ) van het systeem altijd gelijk is aan zes, ongeacht de positie en de lading van de onzuiverheid. In vergelijking met een 2D cluster zonder onzuiverheidslading, blijft enkel de 'breathing' mode onveranderd. We vonden dat de afschermingslengte een sterk niet-lineaire functie van de onzuiverheidslading is. Dit resultaat kan uitgelegd worden als een gevolg van een competitie tussen de verschillende krachten die actief zijn in het systeem.

# *References*

1. E. P. Wigner, Phys. Rev. **46**, 1002 (1934).
2. R. S. Crandall and R. Williams, Phys. Lett. A **34**, 404 (1971).
3. C. C. Grimes and G. Adams, Phys. Rev. Lett. **42**, 795 (1979).
4. R. C. Ashoori, Nature (London), **379**, 413 (1996).
5. S. Neser, C. Bechinger, P. Leiderer, and T. Palberg, Phys. Rev. Lett. **79**, 2348 (1997).
6. R. Bubeck, C. Bechinger, S. Neser, and P. Leiderer, Phys. Rev. Lett. **82**, 3364 (1999).
7. J. H. Chu and L. I, Phys. Rev. Lett. **72**, 4009 (1994).
8. H. Thomas, G. E. Morfill, V. Demmel, J. Goree, B. Feuerbacher, and D. Möhlmann, Phys. Rev. Lett. **73**, 652 (1994).
9. Y. Hayashi and K. Tachibana, Jpn J. Appl. Phys. **33**, L804 (1994).
10. A. Melzer, T. Trottenberg, and A. Piel, Phys. Lett. A **191**, 301 (1994).
11. D. J. Wineland and W. M. Itano, Phys. Today **40** (6), 34 (1987).
12. S. L. Gilbert, J. J. Bollinger, and D. J. Wineland, Phys. Rev. Lett. **60**, 2022 (1988).

13. B. G. Levi, *Phys. Today* **41** (9), 17 (1988).
14. F. Diedrich, E. Peik, J. M. Chen, W. Quint, and H. Walther, *Phys. Rev. Lett.* **59**, 2931 (1987).
15. A. Rahman and J. P. Schiffer, in: *Condensed Matter Theories*, Vol **2**, eds. P. Vashishta et al, (Plenum Press, New York, 1987), p. 33.
16. J. Beebe-Wang, N. Elander, and R. Schuch, *Phys. Scripta* **46**, 506 (1992).
17. D. H. E. Dubin and T. M. O'Neil, *Phys. Rev. Lett.* **60**, 511 (1988).
18. R. Rafac, J. P. Schiffer, J. S. Hangst, D. H. E. Dubin, and D. J. Wales, *Proc. Natl. Acad. Sci. U.S.A.* **88**, 483 (1991).
19. K. Tsuruta and S. Ichimaru, *Phys. Rev. A* **48**, 1339 (1993).
20. M. Zuzic1, A. V. Ivlev, J. Goree, G. E. Morfill, H. M. Thomas , H. Rothermel, U. Konopka, R. Sütterlin, and D. D. Goldbeck, *Phys. Rev. Lett* **85**, 4064 (2000).
21. Y. Kondo, J. S. Korhonen, M. Krusius, V. V. Dmitriev, E. V. Thuneberg, and G. E. Volovik, *Phys. Rev. Lett.* **68**, 3331 (1992).
22. E. J. Yarmachuk and R. E. Packard, *J. Low Temp. Phys.* **46**, 479 (1982).
23. W. I. Galberston and K. W. Schwarz, *Physics Today* **40**, 54 (1987).
24. F. Chevy, K. W. Madison, and J. Dalibard, *Phys. Rev. Lett.* **85**, 2223 (2000).
25. D. Reefman and H. B. Brom, *Physica C* **183**, 212 (1991).
26. E. O. Budrene and C. B. Howard, *Nature (London)* **376**, 49 (1995).
27. L. Tsimring, H. Levine, I. Aranson, E. Ben-Jacob, I. Cohen, O. Shochet, and W. N. Reynolds, *Phys. Rev. Lett.* **75**, 1859 (1995).
28. G. E. Volovik and U. Parts, *Pis'ma Zh. Eksp. Teor. Fiz.* **58**, 826 (1993) [*JETP Lett.* **58**, 774 (1993)].
29. M. Saint Jean, C. Even, and C. Guthmann, *Europhys. Lett.* **55**, 45 (2001).
30. B. A. Grzybowski, H. A. Stone, and G. M. Whitesides, *Nature (London)* **405**, 1033 (2000).
31. B. A. Grzybowski, H. A. Stone, and G. M. Whitesides, *Applied Physical Sciences* **99**, 4147 (2002).
32. P. Leiderer, W. Ebner, and V. B. Shikin, *Surf. Sci.* **113**, 405 (1987).

33. P. L. Elliott, S. S. Nazin, C. I. Pakes, L. Skrbek, W. F. Vinen, and G. F. Cox, *Phys. Rev. B* **56**, 3447 (1997).
34. S. Ichimaru, *Rev. Mod. Phys.* **54**, 1017 (1982). D. H. E. Dubin and T. M. O'Neil, *ibid.* **71**, 87 (1999).
35. V. N. Tsytovich, G. E. Morfill, and H. Thomas, *Plasma Phys. Rep.* **28**, 623 (2002). G. E. Morfill, V. N. Tsytovich, and H. Thomas *ibid.* **29**, 1 (2003).
36. S. V. Vladimirov and K. Ostrikov, *Physics Reports*, **393**, 175 (2004).
37. C. K. Goertz, *Rev. Geophys.* **27**, 271 (1989).
38. T. G. Northrop, *Physica Scripta* **45**, 475 (1992).
39. G. S. Selwyn, J. Singh, and R. S. Bennett, *J. Vac. Sci. Technol. A* **7**, 2758 (1989).
40. G. S. Selwyn, J. S. McKillop, K. Haller, and J. Wu, *J. Vac. Sci. Technol. A* **8**, 1726 (1990).
41. A. Bouchoule, A. Plain, L. Boufendi, J. P. Blondeau, and C. Laure, *J. Appl. Phys.* **70**, 1991 (1991).
42. P. Belenguer, J. P. Blondeau, L. Boufendi, M. Toogood, A. Plain, A. Bouchoule, C. Laure, and J. P. Boeuf, *Phys. Rev. A* **46**, 7923 (1992).
43. C. Hollenstein, *Plasma Phys. Control. Fusion* **42**, R93 (2000).
44. J. Perrin, J. Schmitt, C. Hollenstein, and A. Howling, *Plasma Phys. Control. Fusion* **42**, B353 (2000).
45. J. M. Liu, W. T. Juan, J. W. Hsu, Z. H. Huang, and L. I, *Plasma Phys. Controlled Fusion* **41**, A47 (1999); A. Piel and A. Melzer, *ibid.* **44**, R1 (2002).
46. H. Ikezi, *Phys. Fluids*. **29**, 1764 (1986).
47. A. Melzer, M. Klindworth, and A. Piel, *Phys. Rev. Lett.* **87**, 115002 (2001).
48. A. Melzer, *Phys. Rev. E* **67**, 016411 (2003).
49. S. Peters, A. Homann, A. Melzer, and A. Peil, *Phys. Lett. A* **223**, 389 (1996).
50. G. Praburam and J. Goree, *Phys. Plasmas* **3**, 1212 (1996); J. B. Pieper and J. Goree, *Phys. Rev. Lett.* **77**, 3137 (1996).
51. J. B. Pieper and J. Goree, *Phys. Rev. Lett.* **77**, 3137 (1996).

52. S. Nunomura, D. Samsonov, and J. Goree, *Phys. Rev. Lett.* **84**, 5141 (2000).
53. S. Nunomura, J. Goree, S. Hu, X. Wang, A. Bhattacharjee, and K. Avinash, *Phys. Rev. Lett.* **89**, 035001 (2002).
54. V. Nosenko, S. Nunomura, and J. Goree, *Phys. Rev. Lett.* **88**, 215002 (2002).
55. V. A. Schweigert and F. M. Peeters, *Phys. Rev. B* **51**, 7700 (1995).
56. M. Kong, B. Partoens, and F. M. Peeters, *New Journal of Physics* **5**, 23 (2003).
57. R. A. Quinn, C. Cui, J. Goree, J. B. Pieper, H. Thomas, and G. E. Morfill, *Phys. Rev. E* **53**, 2049 (1996).
58. A. Melzer, A. Homann, and A. Piel, *Phys. Rev. E* **53**, 2757 (1996).
59. A. Melzer, V. Schweigert, I. Schweigert, A. Homann, S. Peters, and A. Piel, *Phys. Rev. E* **54**, R46 (1996).
60. H. M. Thomas and G. E. Morfill, *Nature (London)* **379**, 806 (1996).
61. C. H. Chiang and L. I, *Phys. Rev. Lett.* **77**, 647 (1996).
62. L. I, W. T. Juan, C. H. Chiang, and J. H. Chu, *Science* **272**, 1626 (1996).
63. B. Annaratone, *J. Phys. IV France* **7**, C4 155 (1997).
64. Y. J. Lai and L. I, *Phys. Rev. Lett.* **89**, 155002 (2002).
65. W. T. Juan and L. I, *Phys. Rev. Lett.* **80**, 3073 (1998).
66. U. Konopka, G. E. Morfill, and L. Ratke, *Phys. Rev. Lett.* **84**, 891 (2000).
67. L. Bonsall and A. A. Maradudin, *Phys. Rev. B* **15**, 1959 (1977).
68. W. T. Juan, Z. H. Huang, J. W. Hus, Y. J. Lai, and L. I, *Phys. Rev. E* **58**, 6947 (1998).
69. W. Y. Woon and L. I, *Phys. Rev. Lett.* **92**, 065003 (2004).
70. V. M. Bedanov and F. M. Peeters, *Phys. Rev. B* **49**, 2667 (1994).
71. U. Konopka, G. E. Morfill, and L. Ratke, *Phys. Rev. Lett.* **84**, 891 (2000).
72. S. G. Amiranashvili, N. G. Gusein-zade, and V. N. Tsytovich, *Phys. Rev. E* **64**, 016407 (2001).
73. T. E. Sheridan, C. R. Buckley, D. J. Cox, R. J. Merrill, and W. L. Theisen, *Phys. Lett. A* (2004).

74. D. Samsonov, J. Goree, Z. Ma, A. Bhattacharjee, H. M. Thomas, and G. E. Morfill, *Phys. Rev. Lett.* **83**, 3649 (1999).
75. D. Samsonov, J. Goree, H. M. Thomas, and G. E. Morfill, *Phys. Rev. E* **61**, 5557 (2000).
76. D. H. E. Dubin, *Phys. Plasmas* **7**, 3895 (2000).
77. A. Homann, A. Melzer, S. Peters, and A. Piel, *Phys. Rev. E* **56**, 7138 (1997).
78. G. Piacente, I. V. Schweigert, J. J. Betouras, and F. M. Peeters, *Phys. Rev. B* **69**, 045324 (2004).
79. B. Liu, K. Avinash, and J. Goree, *Phys. Rev. Lett.* **91**, 255003 (2003).
80. D. A. Weitz and W. B. Russel, *MRS Bulletin* **29**, 82 (2004).
81. I. V. Schweigert, V. A. Schweigert, and F. M. Peeters, *Phys. Rev. Lett.* **84**, 4381 (2000).
82. R. Bubeck, C. Bechinger, S. Nesper, and P. Leiderer, *Europhys. Lett.* **60**, 474 (2002).
83. M. Kong, B. Partoens, and F. M. Peeters, *Phys. Rev. E* **65**, 046602 (2002).
84. B. A. Grzybowski, X. Jiang, H. A. Stone, and G. M. Whitesides, *Phys. Rev. E* **64**, 011603 (2001).
85. K. Nelissen, B. Partoens, and F. M. Peeters, *Phys. Rev. E* **69**, 046605 (2004).
86. K. Nelissen, Master thesis, Universiteit Antwerpen, 2003.
87. R. Ashoori, *Nature (London)* **379**, 413 (1996).
88. M. A. Kastner, *Phys. Today* **46**, 24 (1993).
89. R. Egger, W. Häusler, C. H. Mak, and H. Grabert, *Phys. Rev. Lett.* **82**, 3320 (1999).
90. B. Szafran, F. M. Peeters, S. Bednarek, and J. Adamowski, *Phys. Rev. B* **69**, 125344 (2004).
91. B. Szafran and F. M. Peeters, *Europhys. Lett.* **66**, (2004).
92. B. Szafran, S. Bednarek, and J. Adamowski, *Phys. Rev. B* **67**, 045311 (2003)
93. L. P. Kouwenhoven, T. H. Oosterkamp, M. W. S. Danoesastro, M. Eto, D. G. Austing, T. Honda, and S. Tarucha, *Science* **278**, 1788 (1997).

94. A. Wojs and P. Hawrylak, Phys. Rev. B **53**, 10 841 (1996).
95. I. M. Jiang, M. S. Tsai, C. K. Lu, C. C. Shih, J. V. Chiang, and H. E. Horng, Appl. Phys. Lett. **84**, 245 (2004).
96. T. B. Mitchell, J. J. Bollinger, D. H. E. Dubin, X.-P. Huang, W. M. Itano, and R. H. Baughman, Science **282**, 1290 (1998).
97. D. J. Wineland, J. C. Bergquist, W. M. Itano, J. J. Bollinger, and C. H. Manney, Phys. Rev. Lett. **59**, 2935 (1987).
98. H. F. Hess, R. B. Robinson, R. C. Dynes, J. M. Valles, Jr., and J. V. Waszczak, Phys. Rev. Lett. **62**, 214 (1989).
99. A. A. Abrikosov, Zh. Eksp. Teor. Fiz. **32**, 1442 (1957).
100. B. J. Baelus, PhD thesis, Universiteit Antwerpen, 2002.
101. J. J. Thomson, Philos. Mag. **7**, 237 (1904);
102. A. K. Geim, I. V. Grigorieva, S. V. Dubonos, J. G. S. Lok, J. C. Maan, A. E. Filippov, and F. M. Peeters, Nature (London) **390**, 259 (1997).
103. V. A. Schweigert, F. M. Peeters, and P. Singha Deo, Phys. Rev. Lett. **81**, 2783 (1998).
104. B. J. Baelus, L. R. E. Cabral, and F. M. Peeters, Phys. Rev. B **69**, 064506 (2004).
105. G. Blatter, M. V. Feigel'man, V. B. Geshkenbein, A. I. Larkin, and V. M. Vinokur, Rev. Mod. Phys. **66**, 1125 (1994).
106. Yu. E. Lozovik and E. A. Rakoch, Phys. Rev. B **57**, 1214 (1998).
107. L. Pollack, Bulletin of the American Physical Society, Vol. **49**, No. 1, 115, March 22-26, Montréal, Canada (2004).
108. A. M. Mayer, Nature (London) **18**, 258 (1878).
109. B. Partoens, PhD thesis, Universiteit Antwerpen, 2000.
110. K. J. Strandburg, Rev. Mod. Phys. **60**, 161 (1988); J. G. Dash, *ibid.* **71**, 1737 (1999).
111. E. g. see F. M. Peeters, *Two-Dimensional Electron Systems*, edited by E. Y. Andrei (Kluwer Academic Publishers, Netherlands) 1997, p 17.
112. B. Partoens, V. A. Schweigert, and F. M. Peeters, Phys. Rev. Lett. **79**, 3990 (1997).
113. S. Tarucha, D. G. Austing, T. Honda, R. J. V. der Hage, and L. P. Kouwenhoven, Phys. Rev. Lett. **77**, 3613 (1996).

114. N. Metropolis, A. W. Rosenbluth, M. N. Rosenbluth, A. M. Teller, and E. Teller, *J. Chem. Phys.* **21**, 1087 (1953).
115. G. A. Farias and F. M. Peeters, *Solid State Commun.* **100**, 711 (1996).
116. W. P. Ferreira, A. Matulis, G. A. Farias, and F. M. Peeters, *Phys. Rev. E* **67**, 046601 (2003).
117. B. Partoens and F. M. Peeters, *J. Phys.: Condens. Matter* **9**, 5383 (1997).
118. P. A. Maksym and T. Chakraborty, *Phys. Rev. Lett.* **65**, 108 (1990); L. Brey, N. F. Johnson and B. I. Halperin, *Phys. Rev. B* **40**, 10647 (1989); F. M. Peeters, *Phys. Rev. B* **42**, 1486 (1990).
119. F. Lindemann, *Z. Phys.* **11**, 609 (1910).
120. V. M. Bedanov, G. V. Gadiyak, and Yu. E. Lozovik, *Phys. Lett. A* **109**, 289 (1985).
121. I. V. Schweigert, V. A. Schweigert, and F. M. Peeters, *Phys. Rev. Lett.* **82**, 5293 (1999).
122. V. A. Schweigert and F. M. Peeters, *Phys. Rev. Lett.* **83**, 2409 (1999).
123. B. J. Baelus, F. M. Peeters, and V. A. Schweigert, *Phys. Rev. B* **63**, 144517 (2001).
124. C. J. Cerjan and W. H. Miller, *J. Chem. Phys.* **75** (6), 2800 (1981).
125. J. H. Van Leeuwen, *J. Physique* **6**, 361 (1921); R. Kubo, *Statistical Mechanics* (Amsterdam: North-Holland, 1965).
126. V. A. Schweigert and F. M. Peeters, *J. Phys.: Condens. Matter* **10**, 2417 (1998).
127. S. Fortune, *Algorithmica* **2**, 153 (1987).
128. Y. J. Lai and L. I, *Phys. Rev. E* **60**, 4743 (1999).
129. L. J. Campbell and R. M. Ziff, *Phys. Rev. B* **20**, 1886 (1979).
130. P. Cheung, M. F. Choi, and P. M. Hui, *Solid Stat. Commun.* **103**, 357 (1997).
131. F. Bolton and U. Rössler, *Superlatt. Microstruct.* **13**, 139 (1993).
132. G. Date, M. V. N. Murthy, and R. Vathsan, *J. Phys.: Condens. Matter* **10**, 5875 (1998).
133. R. C. Gann, S. Chakravarty, and G. V. Chester, *Phys. Rev. B* **20**, 326 (1979).

134. A. A. Koulakov and B. I. Shklovskii, *Phys. Rev. B* **57**, 2352 (1998).
135. Y. J. Lai and L. I, *Phys. Rev. E* **64**, 015601 (2001).
136. L. Cândido, J. P. Rino, N. Studart, and F. M. Peeters, *J. Phys.: Condens. Matter* **10**, 11627 (1998).
137. I. V. Schweigert, V. A. Schweigert, A. Melzer, and A. Piel, *Phys. Rev. E* **62**, 1238 (2000).
138. M. Kong, B. Partoens, and F. M. Peeters, *Phys. Rev. E* **67**, 021608 (2003).
139. F. M. Peeters, Minghui Kong and B. Partoens, the third international conference on the physics of dusty plasmas: Dusty Plasmas in the New Millennium, edited by R. Bharuthan et al. (AIP Conf. Proc. Vol 649) (New York: American Institute of Physics) p. 192-195 (2002).
140. S. Earnshaw, *Trans. Camb. Phil. Soc.* **7**, 97 (1842).
141. B. Partoens and P. Singha Deo, *Phys. Rev. B* **69**, (2004).
142. N. W. Ashcroft and N. D. Mermin, *Solid State Physics* (Saunders College Publishing, USA, 1976).
143. K. Zahn, R. Lenke, and G. Maret, *Phys. Rev. Lett.* **82**, 2721 (1999); K. Zahn and G. Maret, *Phys. Rev. Lett.* **85**, 3656 (2000).
144. A. V. Filinov, M. Bonitz, and Yu. E. Lozovik, *Phys. Rev. Lett.* **86**, 3851 (2001).
145. H. Totsuji, *Phys. Plasmas* **8**, 1856 (2001).
146. M. A. Moore and A. Pérez-Garrido, *Phys. Rev. Lett.* **82**, 4078 (1999).
147. B. I. Halperin and D. R. Nelson, *Phys. Rev. Lett.* **41**, 121 (1978).
148. U. Konopka, D. Samsonov, A. V. Ivlev, J. Goree, and V. Steinberg, *Phys. Rev. E* **61**, 1890 (2000).
149. F. Cheung, A. Samarian, and B. James, *New Journal of Physics* **5**, 75 (2003).
150. O. Ishihara, T. Kamimura, K. I. Hirose, and N. Sato, *Phys. Rev. E* **66**, 046406 (2002).
151. D. B. Mast, A. J. Dahm, and A. L. Fetter, *Phys. Rev. Lett.* **54**, 1706 (1985).
152. W. P. Ferreira, G. A. Farias, and F. M. Peeters, *Phys. Rev. E* **68**, 066405 (2003).

153. C. Reichhardt and C. J. O. Reichhardt, Phys. Rev. Lett. **90**, 095504 (2003).
154. J. A. Drocco, C. J. Olson Reichhardt, C. Reichhardt, and B. Jankó , Phys. Rev. E **68**, 060401 (2003).
155. E. Zaremba, I. Nagy, and P. M. Echenique, Phys. Rev. Lett. **90**, 046801 (2003).
156. T. Ando, A. B. Fowler, and F. Stern, Rev. Mod. Phys. **54**, 437 (1982).



# *List of publications*

## **Resulting from this work**

1. Minghui Kong, B. Partoens, A. Matulis and F. M. Peeters, *Structure and spectrum of two-dimensional clusters confined in a hard wall potential*, Phys. Rev. E **69**, 036412 (2004) (10 pages).
2. Minghui Kong, W. P. Ferreira, B. Partoens and F. M. Peeters, *Magnetic field dependence of the normal mode spectrum of a planar complex plasma cluster*, IEEE Transactions on Plasma Science, Vol. **32**, No. 2, 569 (2004) (4 pages).
3. Minghui Kong, B. Partoens and F. M. Peeters, *Topological defects and Non-homogeneous melting of large 2D Coulomb Clusters*, Phys. Rev. E **67**, 021608 (2003) (8 pages).
4. Minghui Kong, B. Partoens, and F. M. Peeters, *Structural, dynamical and melting properties of two-dimensional Clusters of Complex Plasmas*, New Journal of Physics **5**, 23 (2003) (17 pages).
5. Minghui Kong, B. Partoens, and F. M. Peeters, *Transition Between Ground State and Metastable States in Classical 2D Atoms*, Phys. Rev. E **65**, 046602 (2002) (13 pages).
6. F. M. Peeters, B. Partoens and Minghui Kong, *The classical electron gas in artificial structures*, in the proceedings of the International School of Physics “Enrico Fermi” (Varenna, Italy, 2003) (20 pages).

7. F. M. Peeters, Minghui Kong and B. Partoens, *Geometry induced defects in a confined Wigner lattice*, the third international conference on the physics of dusty plasmas: Dusty Plasmas in the New Millennium, edited by R. Bharuthan et al. (AIP Conf. Proc. Vol 649) (New York: American Institute of Physics) p. 192-195 (2002) (4 pages).
8. Minghui Kong, A. Vagov, B. Partoens, F. M. Peeters, W. P. Ferreira, and G. A. Farias, *Nonlinear screening in large two-dimensional Coulomb clusters*, submitted to Phys. Rev. B.

#### Related to this work

9. Zhaoyang Chen, Minghui Kong, M. V. Milošević, and Yican Wu, *Ground state configurations of the two-dimensional plasma crystals under long-rang attractive particles interaction force*, Physica Scripta **67**, 439 (2002). (4 pages).

#### Other publications

10. Wu YC, Chen YX, Huang QY, Liu BX, Zhu XX, and Kong MH *Analysis on nuclear heating in the superconducting coils of HT-7U tokamak fusion device*, Fusion Engineering and Design **66-8**, 1013 (2003).
11. Huang QY, Chai ZX, Chen YX, Wu YC, Chen CB, and Kong MH *Design and analysis of the radiation shield and safety system for HT-7U tokamak*, Fusion Engineering and Design **69**, (1-4), 749 (2003).
12. Kong MH, Huang QY, Wu YC, and Chen CB *Calculation and analysis on the dose of radiation for the HT-7U tokamak fusion device by 1D Photon/Neutron transportation code ANISN*, Chinese Journal of Nuclear Technology Vol. **8**, (2000).
13. Kong MH, Huang QY, and Wu YC *Computer simulation of Particle Transportation Analysis on Circumstance Radiation Field by ANISN Code*, in the proceedings of the Pacific-Asia International Conference on Micro-computer Application, May 28th-30th, Hefei, China (2000).
14. Chen CB, Wu YC, Huang QY, and Kong MH *Research on radiation safety and shield for the HT-7U tokamak fusion device by code DOT3.5*, Chinese Journal of Nuclear Technology Vol. **8**, (2000).



## *Curriculum Vitae*

*KONG Minghui*

Born on Feb. 20, 1972  
in LiaoNing / P. R. China

*Education and Professional Experience:*

**Sept. 1990 - July 1994:** obtained Bachelor of Science degree, Department of Physics, Anhui University, majored in Applied Physics.

**Sept. 1994 - July 1997:** Staff scientist in Institute of Plasma Physics, Chinese Academy of Sciences.

**Sept. 1997 - July 2000:** obtained Master of Engineering degree, Institute of Plasma Physics, Chinese Academy of Sciences, Hefei, P. R. China.

**Sept. 2000 - Sept. 2004:** Research Assistant in Condensed Matter Theory group, Physics Department, University of Antwerp (Campus Drie Eiken), Belgium.

Promotor: Prof. Dr. F. M. Peeters